Numerical Analysis of Tonal Noise Emissions from Open and Shrouded Contra-Rotating Propellers

MSc Thesis Project

Jack Evan Barker

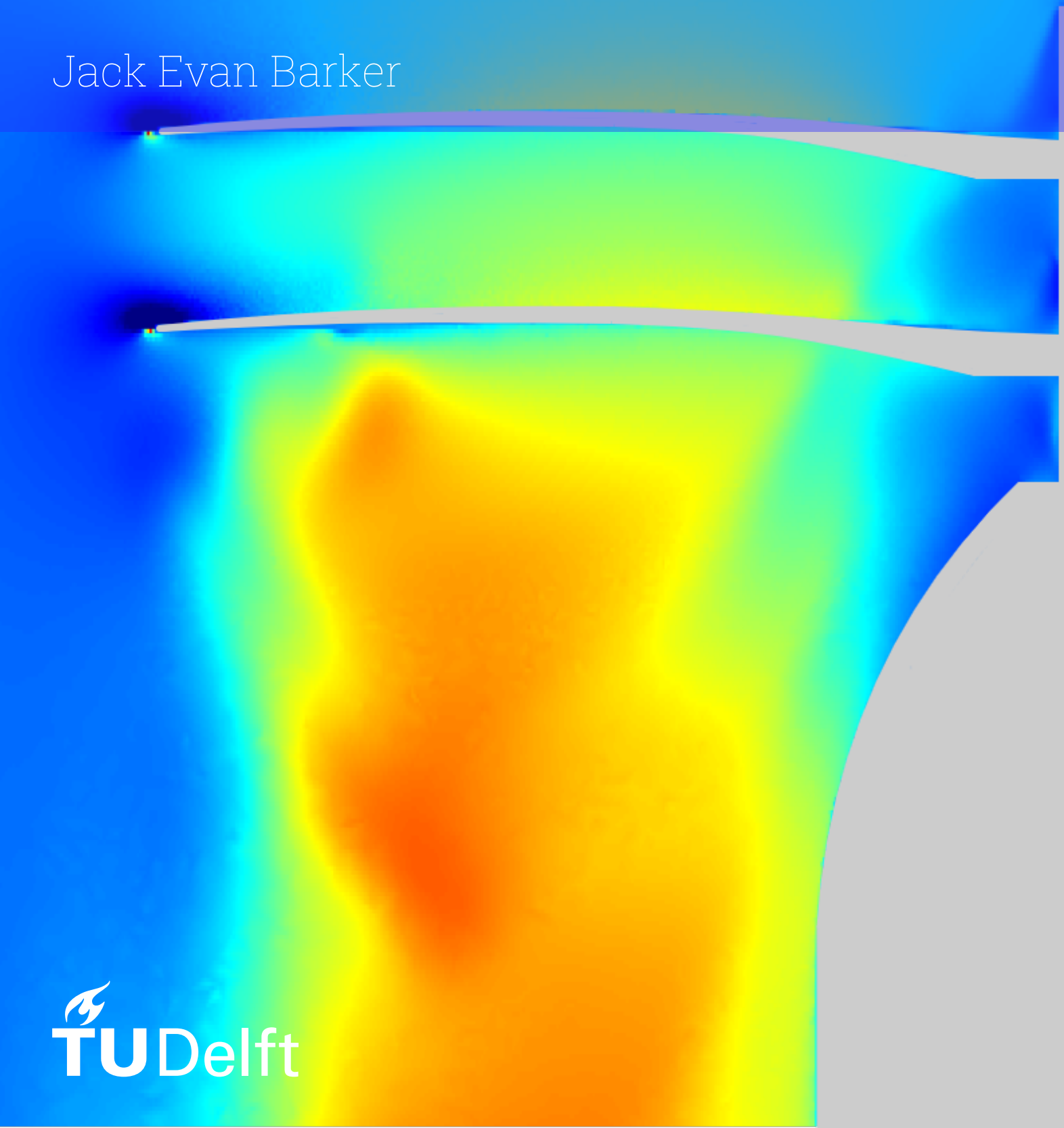

TU Delft

Numerical Analysis of Tonal Noise Emissions from Open and Shrouded Contra-Rotating Propellers

MSc Thesis Project

by

Jack Evan Barker

to obtain the degree of Master of Science
at the Delft University of Technology
to be defended publicly on
November 9^{th}, 2023 at 10:30

Thesis Committee:

Chair:	Dr. Tomas Sinnige	TU Delft - Flight Performance and Propulsion
Responsible Supervisor:	Dr. Daniele Ragni	TU Delft - Wing Energy
External Examiner:	Prof. Francesco Avallone	TU Delft - Wing Energy & Politecnico di Torino
External Supervisor:	Dr. Alessandro Zarri	von Karman Institute for Fluid Dynamics

Project Duration:	February 17^{th} - November 9^{th}, 2023
Assessing Faculty:	Faculty of Aerospace Engineering, TU Delft
Student Track:	Flight Performance and Propulsion
Student Number:	5458218

TU Delft

Preface

I was always going to be an engineer. There was never a doubt in my mother's mind. The way I would take apart my toys instead of playing with them. But, when I was 14 years old my parents gifted me a "Discovery Flight" in a little old Piper Cherokee at a local airport. This seemingly ephemeral gift suddenly sparked my enduring love for aircraft and flying. By 16, I proudly earned my Private Pilot's License and suddenly the sky was the limit.

Embarking on the rigorous journey through aerospace engineering, I pursued my bachelor's at ASU and master's at TU Delft, perpetually propelled by my initial fascination with flight. A coincidence recommendation introduced me to the von Karman Institute for Fluid Dynamics, an organization that shaped the past year and a half of my life.

Beginning with a summer internship and evolving through my thesis project, I have been afforded many incredible opportunities. My integration into the ENODISE project enabled me to dive deep into the European aerodynamics community, forging connections with passionate and insightful people like Sophie Le Bras and Korcan Kucukcoskun from Siemens, and Michel Roger from École Centrale de Lyon. Moreover, opportunities to share my work at several international meetings and contribute to publications, including my own AIAA conference paper [1] and database contributions [2, 3], has been immensely gratifying.

However, none of this would have been possible without the continuous support of my supervisor and mentor Alessandro Zarri. An immense thank you for always being available, day or night, to discuss ideas and all the possible avenues my research could take. Also, for humanizing the world of aeroacoustics, always supporting me, and introducing my work to anyone who would listen.

I would also like to thank the rest of the VKI team. Especially Professor Christophe Schram and Dr. Julien Christophe for their insight and feedback as well as for working with me on my conference paper.

A huge thank you to my parents who didn't know what they started all those years ago. Thank you for being ever supportive and patient with this process. I am sorry for all those trips you needed to make across the pond, I'm sure you hated visiting so much.

And to Alizé, whose pull on my heart has dragged me halfway around the world and considerably confused my job prospects, thank you for your unending support. I hope this is the final stepping stone to our future.

There are a million more people to thank that I cannot list here. From the Room 2.42 group who I am forced to mention because they mentioned me, to long-time friends who I can call up after years of radio silence as if no time had passed, I could not have done this on my own, thank you.

Jack Evan Barker
Delft, October 2023

I am not ashamed to confess that I am ignorant of what I do not know.
- Cicero

Summary

As market growth projections for Urban Air Mobility vehicles (UAMs) skyrocket, their presence in urban environments is likely to become increasingly prevalent, as will their noise. This creates a disturbance to both humans and wildlife, previously unaffected by aircraft noise. Further reinforcing the concern is the new multi-rotor designs, which introduce additional sources of noise.

Research on novel designs provides a limited understanding of the primary noise-generating mechanisms contributing to overall sound production. Among these innovative designs, complex geometries like open Contra-Rotating Propellers (CRP) and Shrouded Contra-Rotating Propellers (S-CRP) emerge. This study focuses on CRPs because they are anticipated to offer increased thrust with the same platform area, crucial for urban UAM operations. Additionally, shrouds are explored for their potential for increased thrust, acoustic shielding, and directivity manipulation, while also offering space for acoustic liners and increasing safety for ground operators.

The objective of this study is to isolate the aerodynamic and acoustic installation effects and identify the noise-generating mechanisms of the CRP and S-CRP configurations.

For this, the aerodynamics and acoustics of six propeller configurations are analyzed, including both the primary CRP and S-CRP geometries and sub-variants thereof. The exploration uses a hybrid numerical methodology, consisting of an aerodynamic flow solver based on the unsteady Reynolds-Averaged Navier-Stokes equations (uRANS) and a Finite Element Method (FEM) acoustic propagation solver. The latter generates acoustic sources from the aerodynamic solution using the source mode formalism.

This not only facilitates an aerodynamic understanding of the acoustic sources but can also detail near-field effects on acoustic propagation. While alternative methodologies achieving similar results necessitate high-fidelity simulations, the uRANS-FEM method can effectively capture aerodynamic and propagation effects within a moderate computational time. However, it also restricts analysis to tonal components of loading noise.

The CRP configuration showcased an improvement in efficiency metrics, marked by a 2.98% increase in FOM and a 57.53% increase in thrust per area, suggesting their higher efficiency and compactness compared to a single rotor. However, this came at the cost of increased noise levels, with amplifications ranging from 10 to 50 dB across various harmonics, attributed to the interaction of the contra-rotating blades. The study further noted a reduction in thrust for both the lead and rear propellers due to the interaction, particularly within the inner 75% radius of the rear propeller. A correlation between the azimuthal angle of the peak thrust and the angle of the highest noise generation was also observed.

When employing a shroud on a CRP, significant modifications in the performance of the shroud were not as anticipated in the literature. The shroud, while contributing to overall thrust, led to a considerable thrust reduction (over 54%) for both propellers due to separated flow. Acoustically, the shroud induced only a minor reduction in noise due to the aerodynamic effects, primarily due to decreased mean thrust. The dominant aerodynamic noise-generating mechanism in the S-CRP configuration is still the blade interaction.

Contrary to expectations, the study found that the shroud in S-CRPs did not effectively mitigate noise radiation in the rotor plane. Instead, there was an increase in noise (5 to 25 dB), largely due to the acoustic interference and the specific position of the propellers within the shroud. This led to a redistribution of sound, particularly affecting the noise emissions of the lead propeller, which was near the shroud's leading edge.

Overall, the study provides valuable insights into the complexity of applying shrouds to CRP systems, highlighting significant variations in thrust and acoustic properties compared to single propeller systems. The findings underscore the need for careful consideration of aerodynamic and acoustic installation effects in the design and application of CRPs and S-CRPs in urban environments.

Contents

List of Figures

Nomenclature

Abbreviations

Abbreviation	Definition
AML	Automatically Matched Layer
BEM	Blade Element Momentum Theory
BLH	Blade Loading Harmonics
BPF	Blade Passage Frequency
BPFH	Blade Passage Frequency Harmonic
BVI	Blade-Vortex Interaction
BWI	Blade-Wake Interaction
CAD	Computer-Aided Design
CFD	Computational Fluid Dynamics
CGNS	CFD General Notation System
CROR	Contra-Rotating Open Rotor
CRP	Contra-Rotating Propeller
FAR	Federal Aviation Regulations
FEM	Finite Element Method
FOM	Figure of Merit
FW-H	Ffwoc-Williams and Hawkings
MRF	Moving Reference Frame
NASA	National Aeronautics and Space Administration
OSPL	Overall Sound Pressure Level
PWL	Sound Power Level
RANS	Reynolds-Averaged Navier–Stokes (steady)
S-CRP	Shrouded Contra-Rotating Propeller
SPL	Sound Pressure Level
UAM	Urban Air Mobility
UAV	Unmanned Aerial Vehicles
uRANS	Unsteady Reynolds-Averaged Navier–Stokes
VKI	von Karman Institute for Fluid Dynamics

Symbols

Symbol	Definition	Unit
c	Speed of Sound	[m/s]
d	Propeller Separation Distance	[m]
d_1	Distance for Lead Propeller	[m]
d_2	Distance for Rear Propeller	[m]
f	Frequency	[Hz]
h	Mesh Ratio	[-]
k	Wavenumber	[Hz]
k	Load Harmonic Order	[-]
l	Characteristic Length of a Body	[m]
m	Sound Harmonic	[-]
n	Rotation Rate	[Hz]
$\hat{n}$	Unit Surface Normal Direction	[-]
p	Pressure	[Pa]
p_{rms}	Root-Mean-Square of Pressure	[Pa]
r	Radial Position	[m]
t	Time (at Source)	[s]
u	Velocity	[m/s]
u_a	Axial Velocity	[m/s]
u_t	Tangential Velocity	[m/s]
A	Amplitude	[Pa]
B_1	Number of Blade, Lead Propeller	[-]
B_2	Number of Blade, Rear Propeller	[-]

Symbol	Definition	Unit
C_P	Power Coefficient	[-]
C_T	Coefficient of Thrust	[-]
D	Blade Diameter	[m]
D_e	Shroud Exit Diameter	[m]
D_t	Shroud Throat Diameter	[m]
He	Helmholtz Number	[-]
I	Acoustic Intensity	[-]
J	Advance Ratio	[-]
J_2	Advance Ratio with Axial Displacement	[-]
$J_n(x)$	Bessel Function of the First Kind	[-]
L	Characteristic Length	[m]
L_c	Shroud Center Section Length	[m]
L_d	Shroud Diffuser Length	[m]
L_i	Shroud Inlet Length	[m]
L_p	Sound Pressure Level (SPL)	[-]
L_W	Sound Power Level (SWL)	[-]
P	Power	[W]
P_a	Acoustic Source Power	[W]
P_in	Input Power	[W]
Q	Torque	[Nm]
R	Blade Radius	[m]
T	Thrust	[N]
T_c	Thrust Coefficient	[-]
T_s	Period	[s]
U_∞	Freestream Velocity	[m/s]
α	Angle of Attack	[°]
δ_{tip}	Tip Gap	[m]
θ	Diffuser Angle	[°]
λ	Wavelength	[m]
ρ	Density	[kg/m^3]
τ	Retarded Time	[s]
ϕ	Blade Twist Angle	[rad/s]
ω	Angular Frequency	[°]
Θ	Azimuthal Blade Angle	[°]
Ω	Rotation Rate	[rev/s]
Ω_1	Rotation Rate, Lead Propeller	[rev/s]
Ω_2	Rotation Rate, Rear Propeller	[rev/s]

1

Introduction

1.1. Context and Motivation

The multi-rotor arrangement has become an increasingly common design choice for electric aircraft propulsion. With ranges of designs that include distributed leading edge propulsion [21], over-the-wing propulsion [22], tip-mounted propulsion [21], contra-rotating propellers[4], shrouded propellers [23], and combinations of these. These configurations are useful in a variety of markets, including Urban Air Mobility vehicles (UAMs). UAMs, which are often referred to by the reductive moniker of *flying taxis*, are vehicles designed to replace cars, buses, trains, and even some short regional jets for intracity and intercity travel. A survey of current designs already includes ranges of 35-300 km [24]. Growth projects are skyrocketing with the expectation that the market for intercity UAM services will be about $32 billion worldwide while the entire market scope can be up to $320 billion by 2035 [25]. There is already an estimated $5.5 billion invested in their development as of 2021.

While UAM technologies offer many implementations and have promising market growth, it is important to also address the issue of noise generation, as these systems are often designed to fly lower and closer to communities that were previously undisturbed by air traffic noise [26, 27]. Such vehicles may be annoying to humans [28] and disturbing to animals and their habitats [29]. This thesis project investigates both the noise and performance of two configurations, contra-rotating propellers (CRP) and shrouded contra-rotating propellers (S-CRP).

The largest benefit of contra-rotating propellers is that they provide reduced planform areas compared to multiple single-rotor propellers while delivering the same thrust [30]. For example, both Ehang 216F (Figure 1.1(a)) and Volocopter VoloCity (Figure 1.1(b)) are designs that include a two-person cabin of approximately the same size and use approximately the same number of propellers, however, the planform area of the Ehang 216F is notably smaller due to the application of contra-rotating propellers. These also provide redundancy in case of rotor failures [30], which is especially important in quadcopter designs such as the Workhorse SureFly shown in Figure 1.2 [6]. They also offer performance increases by eliminating the reaction torque of the propellers [31] and increasing the overall efficiency at all advance ratios [32].

(a) (b)

Figure 1.1: A comparison of two UAM designs, the (a) Ehang 216F [4] and the (b) Volocopter VoloCity [5], which have approximately the same cabin but different planform volumes.

Figure 1.2: Workhorse (Moog) SureFly [6].

New UAM designs contain not only a contra-rotating propeller but also a shroud surrounding the propellers. This shrouded contra-rotating propeller design can be seen in the Airbus CityAirbus and the joint venture PopUp.Next from ItalDesign, Audi, and Airbus [33]. Studies show that a shroud can increase thrust total coefficient between 25% and 60% when designed to be thrusting [15, 34]. It also allows for acoustic shielding and directivity manipulation [35] as well as space for acoustic liners. Additionally, safety benefits include protection for ground personnel and equipment as well as shrapnel containment in emergencies [35]. Because of these advantages, shrouds may be required in future certification processes.

A significant disadvantage of contra-rotating propeller systems is the generally higher levels of noise that they produce in comparison to other multi-rotor designs with equivalent thrust performance. This is attributed to the interaction tones produced by the periodic loading on the propeller blades caused by their interaction with the unsteady periodic flow from the other propeller [36]. The addition of a shroud may also be a help both to reduce noise [37] and increase performance [34].

1.2. Challenges of CRPs and Shrouded Propellers

Contra-rotating propellers (CRPs) are a concept in aeronautical propulsion that dates back to 1907 [38, 39]. Only 70 aircraft have used CRPs in their design, mostly serving as single builds or flying test beds [31]. The concept was initially introduced to improve propulsive efficiency, eliminate reaction torque, and provide benefits at high angles of attack. Nevertheless, despite the potential benefits they offer, the adoption of CRPs has diminished due to various challenges they have encountered, such as mechanical complexity, elevated production expenses, increased weight, issues with vibrations, whirl flutter, and noise-related complications.

In recent years, the benefits of CRPs have once again come to light, with the increasing use of electric propulsion making it possible to overcome weight limitations and interest in Unmanned Aerial Vehicles (UAVs) and UAMs pushing the design space. Noise has now become a major limitation for design and researchers are tasked with translating historical knowledge and improving CRP design to meet current performance and noise requirements [40].

Shrouded propellers are more commonly found in marine propulsion [41] and early wind-energy systems [42], but have also been tested for aviation applications since the late 1950s. In the 1950s and 1960s, NASA conducted tests on forward-flight vehicles [43, 44], leading to the development of two tilt-duct prototypes, the Bell X22 and the Doak VZ4D. Although these prototypes were not successful, the concept of shrouded propellers was later applied to helicopter tail rotors as the Fenestron [45] in order to reduce blade vibration, prevent foreign object damage, and increase safety.

Today, companies in the UAS market (which shares design similarities with UAMs) are also considering designs using shrouded single propellers. Commercially produced UAVs, such as the DJI Avata FPV, include a shroud around the quad-copter design [46]. These are presumably employed for safety, although the exact reason for including the shroud is not published in the open literature. In the field of UAMs, concepts not only include shrouded propellers but shrouded contra-rotating propellers. Because companies are beginning to consider designs using shrouded contra-rotating propellers in the burgeoning UAS market and the literature does not yet clearly describe the physical noise-generating processes of CRPs and much less is known about SCRPs, this research focuses on filling in these gaps.

1.3. Research Objectives

The first goal of this project is to apply a *hybrid computational aeroacoustic methodology* to CRP and S-CRP configuration. With the ability to account for acoustic interactions in the near-field with lower processing times than other methods with the same capabilities this method seems, a priori, an extent method for this investigation. Then, from this, the overarching aim of this research project is concisely summarized as follows:

To identify and distinguish the specific mechanisms responsible for performance and acoustic directivity in CRP configurations, and to investigate the applicability and modification of these mechanisms in S-CRP configurations.

To unravel these interactions and their implications on both performance and noise characteristics, the following specific research questions are proposed:

1. *What is the trade-off in terms of Figure of Merit, thrust per area, and acoustic emissions when a contra-rotating propeller configuration is used in place of a single propeller?*
2. *How much are the aerodynamic performance and the noise-generating mechanisms modified when employing a shroud designed for single propeller systems on a CRP one?*
3. *Can a shroud be used to mitigate noise radiation when used on a contra-rotating configuration?*

1.4. Manuscript Outline

This manuscript is structured to facilitate an in-depth exploration of the research objectives and to include a comprehensive background into the physics and methodologies studied. Then, the validation of the methodology is assessed and the results are presented. The final sections present an analysis using the results and matching theory. It is organized as follows:

- Chapter 2 provides the fundamental background for the acoustic analysis in this study followed by a separate examination of the literature concerning three relevant geometries: a single propeller, a CRP, and shrouded propellers. Each presents details on sound-generating mechanisms and parameter trends.
- Chapter 3 describes the background necessary to understand the theory and operation of simulation. The description of the geometries simulated and the simulation configurations of the final results are also presented.
- Chapter 4 presents the verification and validation of the simulation methodology containing comparisons to experimental solutions.
- Chapter 5 is the focal point of the investigation. Here, an analysis of the results is presented and conclusions an made based on the findings.
- Finally, Chapter 6 is a summary of the relevant results and conclusions. It also includes recommendations for future studies.

2

Background

2.1. Acoustic Fundamentals

2.1.1. Fundamentals of Sound

Sound is a wave characterized by pressure fluctuations that travel through a medium. It is described by its speed of propagation, c, frequency, f, and wavelength, λ. Although the speed at which sound propagates can vary depending on the medium's properties, in these simulations, it's taken as 340 m/s for a medium with a density, ρ, of 1.225 kg/m^3. The impacts of sound propagation within a single medium, termed as *acoustic installation effects*.

Wave Propagation

The first acoustic installation effect is radial spreading which is the sound emitted from a single source that propagates as a spherical wave and expands radially. The pressure fluctuation of the wave, therefore, decreases with the radius. Equation 2.1 is the definition of a spherical harmonic wave in complex notation with the pressure fluctuation, p', shown to be inversely proportional to the propagation radius, r. It is also dependent on the initial amplitude of the fluctuation, A, and the time since emission, t.

The first acoustic installation effect, radial spreading, involves sound emitted from a single source, which propagates as a spherical wave and expands radially. Consequently, the amplitude of pressure fluctuation of the wave decreases with the radius. Equation 2.1 defines a spherical harmonic wave in complex notation, illustrating that the pressure fluctuation amplitude, p', is inversely proportional to the propagation radius, r, and also depends on the initial amplitude of the fluctuation, A, and the time elapsed since emission, t.

$$p'(r,t) = A/re^{i\omega(t-r/c)} \tag{2.1}$$

Acoustic interference arises when multiple waves simultaneously coexist in a domain, thereby influencing each other when they occupy the same space. The emerging composite wave is shaped by the phasing of the interacting waves, culminating in either constructive or destructive interference. Constructive interference amplifies the combined wave, creating a louder sound when waves with identical frequencies synchronize their phases. In contrast, destructive interference entails out-of-phase waves of the same frequency, resulting in cancellation and diminished amplitude. For some complex wave patterns, distinct segments of the waveform can experience amplification or attenuation.

Surface Scattering Due To Solid Boundaries

In many problems, the effects of reflected and scattered sound waves due to solid bodies need to be considered in addition to the free-field propagation solution. To quantify this effect, the compactness of the body must be considered. A compact body has a characteristic length small enough compared to the wavelength that is essentially unseen by the sound wave and does not affect the free-field propagation. Therefore, the compactness of a body changes depending on the frequency considered.

Typically a characteristic length l is the longest dimension in the direction of propagation, which is usually the chord, mean chord, or maximum chord, when referring to airfoil shapes. Then using the

wavelength, λ, and the wavenumber, k, the Helmholtz number is defined in Equation 2.2. If this value is less than one the body is considered compact.

$$He = kl = \frac{2\pi}{\lambda} l \tag{2.2}$$

Compact bodies do not affect the propagation of noise from another source but, may produce their own noise. Non-compact sources can change the propagation of noise from another source, known as shielding or amplifying, as well as scattering and reflecting the sound.

Additionally, compact and non-compact bodies present in the near-field of the sound source are known to affect the far-field results [47]. This is due to the interference while the wave is still developing and this is a central component of this study when the shroud is introduced in close proximity to the propeller sources.

While numerical and analytical scattering techniques exist for simple geometries in literature, such as infinite planes, and based on free-field prediction methods [48, 49], the most common solution is using a numerical approach for finding a solution of the Helmholtz partial differential equation and its boundary conditions [50]. However, when geomtries become more complex numerical solutions are required to solve the interactions. One example is Finite Element Methods (FEM), such as in [51], which is a common method for doing this and is what will be used in this study; further implementation details are in subsection 3.3.1.

The *acoustic installation effects* are an important consideration in this study. All of these effects are neatly summarized in Figure 2.1. While there are additional effects to consider in broader applications, such as changing medium, they aren't relevant to this simulation since the fluid remains steady and uniform throughout the study.

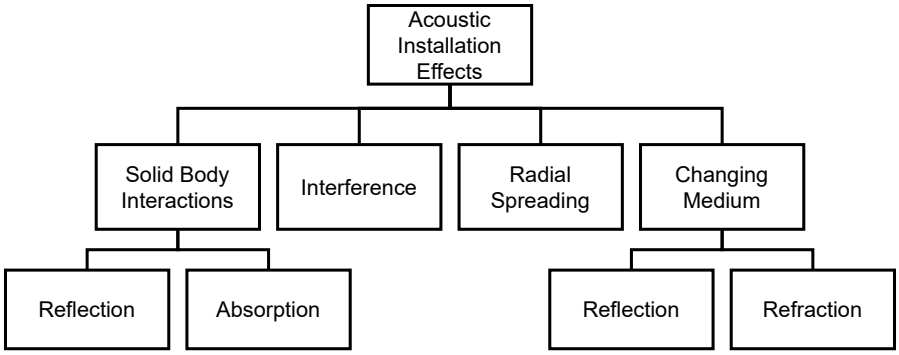

Figure 2.1: Classification of acoustic noise interference based on Ref. [7].

2.1.2. Human Perception and Standard Practices

The range of human hearing that can detect these fluctuations is typically from around $20Hz$ to $20kHz$ but, this depends on many factors including the listener's age and the loudness of the sound [52]. The human auditory system perceives sound levels logarithmically, thereby employing a decibel-scale value called Sound Pressure Level (SPL), which is standard practice.

SPL is determined by Equation 2.4, founded on the root-mean-square of the pressure fluctuations, p_{rms}, recorded at the listener's location over a sample period, T_s, where $p'(t) = p(t) - p_{mean}$ represents the time-dependent pressure fluctuations. A reference pressure value, $p_{ref} = 2 \times 10^{-5}$ Pa, is utilized, thus the hearing threshold of an average individual is at 0 dB and the pain threshold is approximately 130 dB at 1000 Hz. A perceptible difference for most is 2-3 dB, while an increase of 10 dB is commonly perceived as a doubling in loudness [52].

$$L_p = 20 \log_{10} \left(\frac{p_{rms}}{p_{ref}} \right) \tag{2.3}$$

$$p_{rms} = \sqrt{\frac{1}{T_s} \int_0^{T_s} p'^2 dt} \tag{2.4}$$

The frequency-domain analysis of a signal demonstrates how the signal's energy is dispersed across a range of frequencies detailing information not seen in the time domain. To convert from time-history data into the frequency domain a Fourier transformation is applied to the sound signal, as in Equation 2.5. However, it is commonly performed discretely utilizing the general form Equation 2.6, where X signifies the pressure in Fourier space, and x corresponds to the time-dependent pressure signal.

$$X = \int_{\infty}^{\infty} x e^{-i2\pi f t} dt \tag{2.5}$$

$$X_k = \sum_{n=0}^{N-1} x_n e^{-i2\pi k n/N} \tag{2.6}$$

Frequency analysis gives insight into the loudest tones and energy distribution, however, a listener will be affected by all frequencies emitted. The Overall Sound Pressure Level (OSPL) is computed by the summation of all SPL values at all frequencies in dB. This is representative of the total intensity experienced by the listener. The SPL is also typically a function of directivity, θ, from the source.

$$OSPL(f) = 10 \log_{10} \left(\sum_i 10^{SPL(f_i,\theta)/10} \right) \tag{2.7}$$

SPL and OSPL are functions of both directivity and distance from the source and can be affected by many factors in the acoustic field. To investigate changes in the source itself the Sound Power Level (SWL), L_W, is used to determine its strength directly. It is also measured in dB where P_a is the power of the noise source or sources and it is referenced to $P_{a,ref} = 10^{-12} W$.

$$L_W(f) = 10 \log_{10} \left(\frac{P_a}{P_{a,ref}} \right) \tag{2.8}$$

The value for P_a can also be solved from the acoustic emissions if they are known in every direction. This is done by using the acoustic intensity, I, and the p_{rms} value in Equation 2.9, where, A is the area of the listener sphere where p_{rms} is calculated.

$$I = \frac{P_a}{A} = \frac{p_{rms}}{2\rho c} \tag{2.9}$$

2.1.3. Aeroacoustic Analogies

In the 1950s Lighthill introduced an acoustic analogy to investigate jet engine noise [53]. This was extended by Curle to include surface boundaries in the formulation, which allowed the analogy to be solved for stationary surfaces [54]. Then, in 1969, with the formulation by Ffowcs Williams and Hawkings (FW-H) [55], the noise generated by moving surfaces in the flow field could be computed. The FW-H analogy, Equation 2.10, is derived from the Navier-Stokes equations such that it is in the form of a wave equation. This is done by subtracting the divergence of the continuity equation from the time derivative of the momentum equation.

$$\begin{aligned} 4\pi c_0^2 (\rho(\mathbf{x}, t) - \rho_0) H_s = & \frac{\partial^2}{\partial x_i \partial x_j} \int_{V_0} \left[\frac{T_{ij} J}{r \left| 1 - M_r \right|} \right]_\tau d\eta \\ & - \frac{\partial}{\partial x_i} \int_{S_0} \left[\frac{p_{ij} \hat{n}_j A}{r \left| 1 - M_r \right|} \right]_\tau dS(\eta) - \frac{d}{dt} \int_{S_0} \left[\frac{\rho_0 v_n}{r \left| 1 - M_r \right|} \right]_\tau dS(\eta) \end{aligned} \tag{2.10}$$

There are three source terms in this formulation that influence the density fluctuation at the listener ($\rho' = \rho - \rho_0$), where c_0 and ρ_0 are the speed of sound and density, respectively, in the medium around the source. The FW-H equation is solved in *retarded time* where the solution is calculated at the listener's reception time, τ. The emission time is t and listener time is solved as $\tau = t - r(\tau)/c_0$. The coordinate η is the Lagrangian coordinates of a moving reference frame such that the sources are at rest. **x** is the fixed coordinate system listener location and r is the radiation vector between the listener and source.

In the formulation, M_r is the Mach number of the moving source in the radiation direction and $\hat{n}$ is the unit surface normal component.

The first term relies on the Lighthill stress tensor, T_{ij}, and the Jacobian of the source convection velocity, J. It is solved by integrating over the entire volume, V_0, encapsulated by source surface. It is representative of non-linear distortion of the flow and turbulence and is modeled as a quadrupole. A quadrupole is two dipoles placed infinitesimally close to each other and having opposite phases (Figure 2.5). It can be visualized as a deforming sphere without a change in volume or net force. This is a quadrupole and it is the least efficient acoustic source.

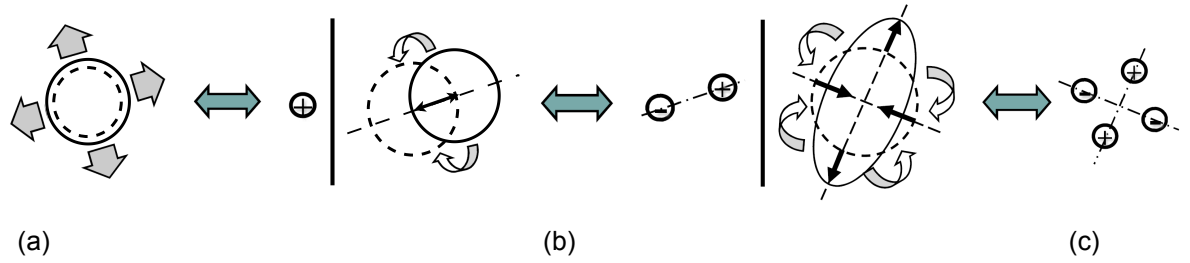

Figure 2.2: Depication of (a) Monopolar, (b) Dipolar, and (c) Quadrupolar sources. [8].

The second term describes the effect of surface forces in terms of the surface pressure distribution, p_{ij}, and the ratio of the area elements in different spaces, A (essentially a two-dimensional Jacobian). Solved by integrating over the surface of the source, S_0, this is described by a dipolar source which is an oscillating sphere that does not change volume and is two monopoles out of phase. This source is more efficient than a quadrupole but less efficient than a monopole.

The last term is the monopolar source, which indicates the volume displacement. The strength of this term is dependent on the density ρ_0 of the fluid and surface velocity relative to the fluid, V_n, which is also the fluid velocity in the η-coordinate field. The monopole is a pulsating sphere with changing volume and is the most efficient source.

Numerical Solutions

If only the surface sources moving at subsonic speeds are considered a common solution of FW-H equation is used known as the Farassat 1A (F1A) formulation [56]. Derived by Farassat and Succi in 1980, this formulation is a time-domain solution that splits the solution into two parts, the thickness noise and the loading noise. Each equation has two terms, one for the near-field and one for the far-field. This derivation indicates that the near-field decays at a rate of $1/r^2$ while the far-field decays with $1/r$ as described in Section 2.1.1.

While this study focuses on the more complex *source mode formalization* with a FEM-based noise propagation (subsection 3.3.1) the F1A method will also be used in the verification and validation section of the study. It gives a good comparison for free-field propagation dipolar (loading) sources. As the source mode solution only considers dipolar (loading) sources, the F1A method can additionally solve for monopolar (thickness) noise giving insight into the contribution of these sources.

The largest limitation of the F1A method is that it can only consider free-field propagation outside the surface. Thus to use it to capture the scattering effect the source surface would have to encapsulate the entire shroud geometry. This in turn requires a direct computation of the acoustic pressure wave propagation up to this surface. Typical CFD second-order schemes, like the one applied in this study, require around 18-25 nodes per wavelength to properly be refined [57]. This is an enormous computation cost for a large source surface.

2.2. Single Propeller

This section explores the fundamental principles that govern propeller aerodynamics. It presents fundamental models for predicting thrust and torque generated by a propeller, offering valuable insights into the underlying physics and considerations related to propeller blades. These simplified models lay the groundwork for the development of more intricate aerodynamic and acoustic models, as further discussed in both this chapter and Chapter 3.

Additionally, this section introduces the key coefficients used to describe propeller performance and operating conditions, ensuring consistency throughout the manuscript. Lastly, it provides an overview of the basics of acoustics in relation to propeller blades, opening the door to an exploration of the current literature on the subject.

2.2.1. Propeller Aerodynamics

A propeller is a device that has radial blades which rotate around a central axis. These blades are twisted and cambered such that when the propeller is rotated by a motor a thrust is generated due to the relative motion of the blades to the surrounding fluid. Therefore, a propeller can be used to convert the torque of an engine into thrust. The propeller imparts an increase in velocity on the entire streamtube of the flow as well as an increase in pressure across the propeller disk.

Basic Propeller Theory

The simplest model of a propeller is the Actuator Disk Theory, which describes the velocity and pressure increases across the propeller by modeling the propeller as a two-dimensional disk where the thrust is distributed uniformly, no rotation is imparted on the flow, and the streamtube entering and leaving the disk has a uniform velocity except in the axial direction [10].

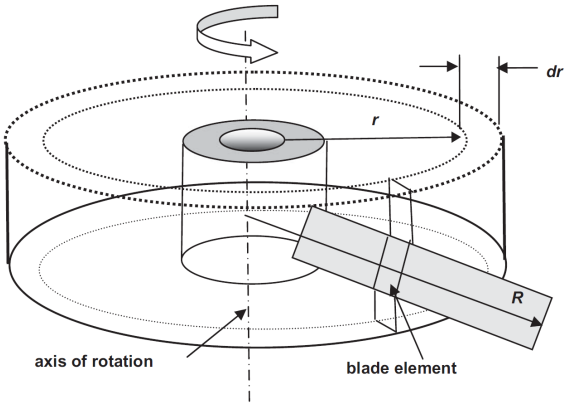

Figure 2.3: Depiction of the discretization of an arbitrary blade element in an annular flow region. [9]

Another model, called Blade Element Theory, discretizes the blades into blade elements as shown in Figure 2.3 where each individual section is described by a two-dimensional airfoil model where the component velocities are used to calculate the lift and drag contributions of each section. The combination of these two models, Blade Element Momentum Theory (BEMT), can be used to solve for the localized forces on the blades as well as the resulting thrust while being able to account for angular momentum.

Each section of the blade distribution in BEMT has a bound circulation described by the Kutta–Joukowsky Theorem [10] thus creating a circulation distribution across each blade. Each bound circulation also has a free circulation and vorticity associated with its strength resulting in a vortex shed from each blade element. The wake is formed by these vortices, and it moves downstream in the shape of a helix as shown in Figure 2.4(a). As with a finite wing, the vortex sheets along the blade roll up into a single vortex stream as they travel downstream as shown in Figure 2.4(b). This now causes the slipstream to include axial and tangential velocity components; the latter commonly referred to as the swirl [10].

Tip Loss

A propeller's efficiency is impacted by the development of a tip vortex at the blade's outer edges. The rolling of the vortex sheets toward the blade tips, as mentioned earlier, results from pressure differentials between the upper (suction side) and lower (pressure side) surfaces of the propeller [10]. These pressure differences arise due to the airfoil section's cambering and angle of attack, which is the basis of lift generation [58].

However, in the absence of any surface obstructing the interaction between these pressure regions, fluid movement occurs from regions of low pressure to those of high pressure over the propeller's finite

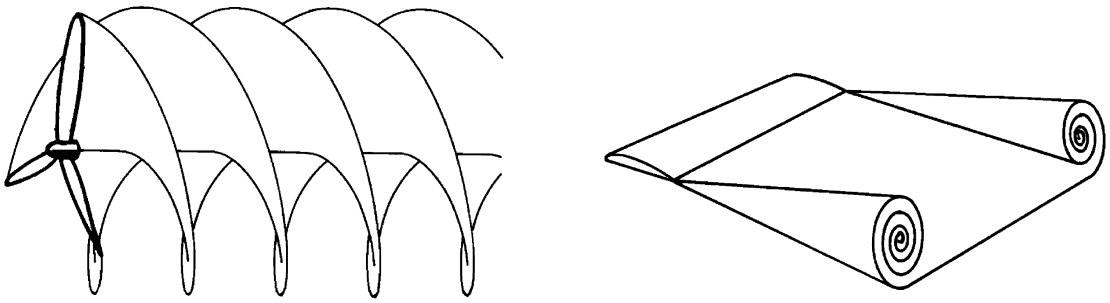

(a) (b)

Figure 2.4: (a) Propeller with trailing helicoidal vortex sheets. [10] (b) Rolling up of the vortex sheet behind a wing. [10]

tip. Consequently, this process diminishes the pressure difference across the blade in areas close to the tip. The outcome is a reduction in the effective thrust generated and the emergence of vortical structures from the tip. [58]

2.2.2. Performance Coefficients

There are usually two approaches to non-dimensionalized thrust. The first is to represent the thrust coefficient in relation to free-stream velocity (Equation 2.11), and the second to the rotational velocity as the coefficient of thrust (Equation 2.12). These are used to analyze the effects of either the flow condition or the propeller parameters, respectively, and are used based on the relevancy of the non-dimensionalization variables to the study.

$$T_c = \frac{T}{\frac{1}{2}\rho_\infty U_\infty^2 \pi R^2} \tag{2.11}$$

$$C_T = \frac{T}{\rho_\infty n^2 D^4} \tag{2.12}$$

In these formulas, T is the thrust, ρ_∞ represents the freestream density, and U_∞ is the freestream velocity. The propeller characteristics are represented by R as the radius, the diameter is $D = 2R$, and n is the rotational speed in Hz. Likewise, the power can be made dimensionless in several ways but the one typically used in literature is given by Equation 2.13. With power being a direct function of the torque, Q, of the system.

$$C_P = \frac{P}{\rho_\infty n^3 D^5} \tag{2.13}$$

$$P = \Omega \cdot \frac{2\pi}{60} Q \tag{2.14}$$

The advance ratio, Equation 2.15, is a non-dimensional number that correlates the forward motion of the propeller, U_∞, with the rotational velocity of the propeller. This number is often used to describe propeller motion and is useful for understanding flight conditions, velocities seen by the propellers, tip vortex paths, and blade loading. For a single propeller, low values close to one show a dominant rotational component, such as in hover and near-hover conditions. High values will have stronger influences from the freestream velocity. For all propellers, the advanced ratio can be used to describe the operating condition of the system but with contra-rotating propellers, it provides much less insight into the performance of the propellers, especially the rear propellers as they are not directly influenced by the freestream velocity.

$$J = \frac{U_\infty}{nD} \tag{2.15}$$

The ratio of effective propulsive power to shaft power is the propeller efficiency. This can also be the coefficient of thrust and advance ratio compared with the coefficient of power.

$$\eta = \frac{TU_\infty}{P_{in}} = \frac{C_T J}{C_P} \tag{2.16}$$

The figure of merit (FOM) is another method used to measure the efficiency of the overall power consumption of the propeller systems. The FOM represents the ratio of the ideal power of the system, P_i, and the actual power used, P. This can be solved using the values of C_T and C_P using the total thrust and total power and in the case of a thrusting shroud, the value also includes any thrust from the shroud.

$$FOM = \frac{P_i}{P} = \frac{C_T^{1.5}}{\sqrt{2}C_P} \tag{2.17}$$

2.2.3. Propeller Acoustics

Propeller noise sources are typically classified into three main categories: broadband noise, harmonic noise, and narrowband random noise [7]. A breakdown of broadband and harmonic noise sources for propellers is given in Figure 2.5.

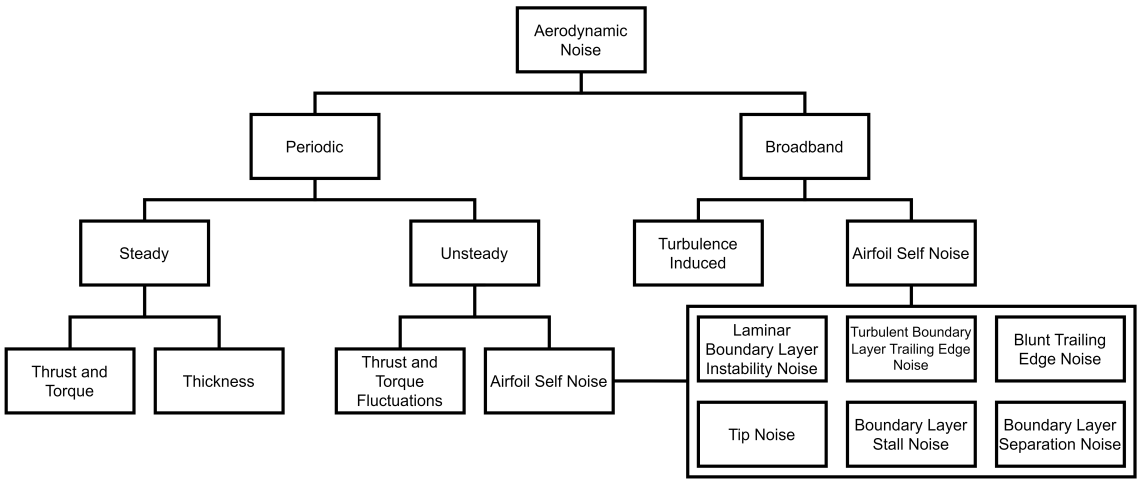

Figure 2.5: Classification of aerodynamic noise sources extended from Ref. [7].

Periodic noise is attributed to sources that repeat consistently in time and therefore arise at a certain frequency due to their pulsing steady pace. These spikes in frequency, as illustrated in Figure 2.6(a), represent a single tone that would be registered by the human ear thus giving the name, tonal noise. This is most commonly seen in propellers at the blade passage frequency (BPF), which is the fundamental rotation frequency, Ω multiplied by the number of blades, B. Also seen in Figure 2.6(a), the energy of this noise is spread to higher harmonics that occur at integer multiples of $B\Omega$. This is referred to as harmonic noise because it occurs at multiples of a certain base frequency.

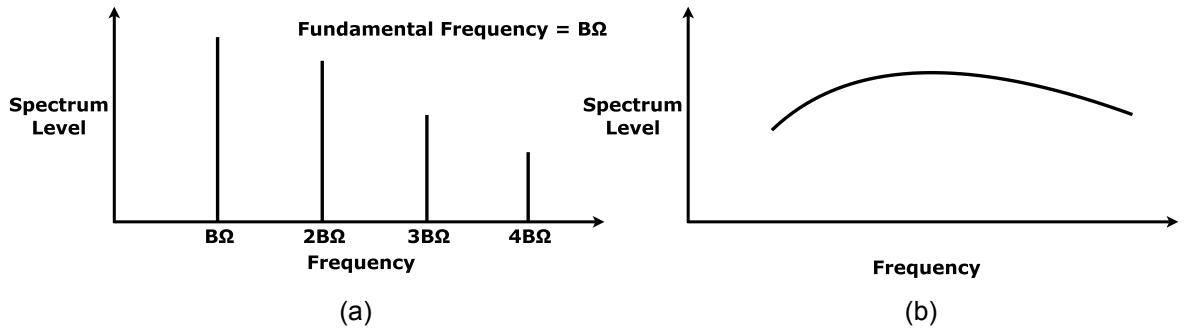

Figure 2.6: (a) Theoretical depiction of harmonic tonal noise [7]. (b) Typical broadband distribution [7].

Broadband noise is made up of random fluctuations that include energy at all frequencies [7]. The frequency spectrum of this noise is continuous but not of equal amplitude at all frequencies. In Figure 2.6(b), a typical shape of a broadband spectrum for propeller noise is depicted. This form of noise is caused by the vorticity created by the blades as well as the turbulence with which the blades interact [59]. Broadband noise typically has a lower sound level than harmonic noise, especially at lower frequencies, but the combination of all pressures at all frequencies can noticeably increase the OSPL.

Psychoacoustic studies indicate that of the different types of noise, tonal noise is perceived as the most annoying by the human ear [60]. As a result, tone noise will be the major focus of this study. The hybrid methodology discussed in Chapter 3 was conceived with this assumption in mind and is limited to tonal noise generated by the surfaces.

Tonal noise is further classified into steady and unsteady sources as shown in Figure 2.5. Each of these has unique characteristics and will have different impacts on the results of this study.

Steady Noise

Steady sources pertain to elements that appear unchanging over time in the rotating reference frame of the propeller blades and are divided into three categories: thickness, loading, and nonlinear [7]. These correspond to the Ffwocs-Williams and Hawking model presented in Section 2.1.3 as monopolar, dipolar, and quadrupolar, respectively. Because these sound-generating mechanisms are steady with regard to the rotating surface of a propeller, they will appear periodic for a stationary listener position.

The volumetric displacement of air by the passing blades causes thickness noise, which has an amplitude proportional to the blade volume and velocity and is represented by a monopole source distribution. Thickness noise becomes more becomes important at high speeds and thicker blades [7].

The force components (thrust and torque) on each blade generate loading noise. This results from the pressure field that surrounds each blade and is modeled with a dipole went when the flow is linear. This is the dominant noise-generating mechanism for propellers at low to moderate speeds with thin blades and will be one of the focuses of this study [7].

Unsteady Noise

Unsteady sources of noise are time dependent as experienced by an individual rotor in the rotating reference frame and the noise can be harmonic or random. The same three noise-generating mechanisms are still thickness, loading, and non-linear noise and they are still modeled using the same analogous source however, they now vary in time in the moving reference frame.

This is caused when the blade sees a change in inflow condition depending on the blade position. A typical example of this would be an angle of attack imposed on the propeller where the individual blade would encounter a varied orientation of freestream velocity depending on the azimuthal angle [7].

Another case that is of interest for new research is when a wing or drone arm to which the propeller is mounted causes a non-uniform inflow angle experienced by the blade. In the case of contra-rotating propellers, the unsteady loading noise becomes a very important noise source and a dominant factor in tonal noise [51].

Airfoil Self Noise

Airfoil self-noise is an important source of noise for both tonal and broadband noise. ”Airfoil self-noise is due to the interaction between an airfoil blade and the turbulence produced in its own boundary layer and near wake” and is the noise produced when non-turbulent flow is encountered [61].

In a study from Brooks, 1989 [61] six characteristic self-noise mechanisms were presented, some of which will be relevant in the coming project, they are laminar boundary layer instability noise, turbulent boundary layer trailing edge noise, blunt trailing edge noise, tip vortex formation noise, boundary layer separation noise, and boundary layer stall noise. These are all depicted in Figure 2.7. While this study only presents periodic changes to the pressure on the blade surface, some or all of these effects may be present in the experimental simulations to which the results are compared.

Of these six the only periodic noise source on the surface is the laminar boundary layer instability noise. Turbulent boundary layer trailing edge noise and tip vortex formation noise are broadband-generating mechanisms. The blunt trailing trailing edge noise occurs off the surface and thus is not captured in this study. Finally, the boundary layer separation noise and stall noise create quasi-tonal noise which will not be captured unless it occurs at the blade passage frequency (or its harmonics) and is give very tonal characterisitcs.

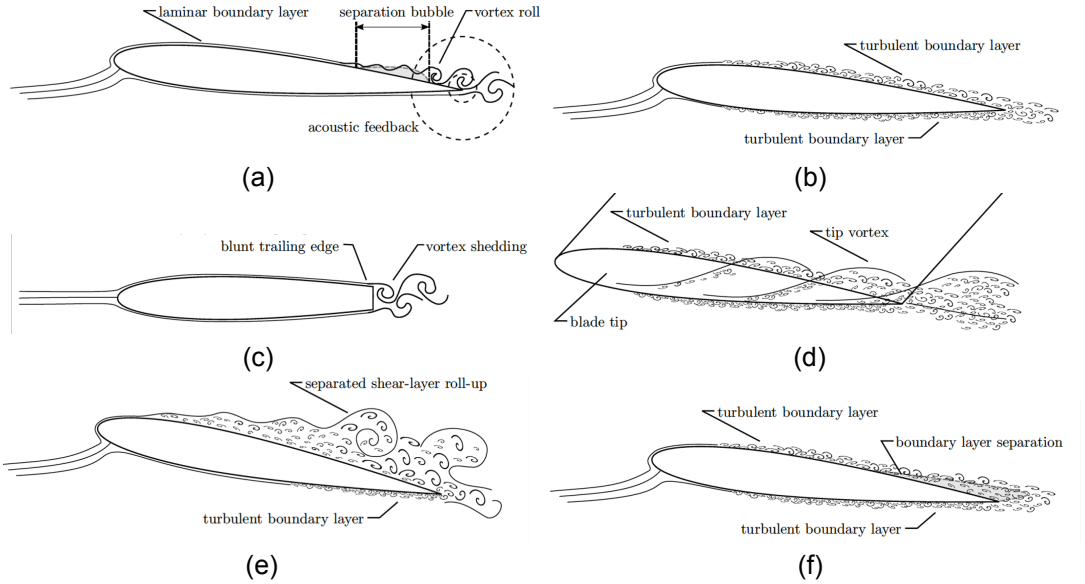

Figure 2.7: (a) Laminar Boundary Layer Instability Noise. (b) Turbulent Boundary Layer Trailing Edge Noise. (c) Blunt Trailing Edge Noise. (d) Tip Vortex Formation Noise. (e) Boundary Layer Stall Noise. (f) Boundary Layer Separation Noise. [11]

Laminar boundary layer instability noise is a form of trailing edge noise that creates tonal noise. It is characteristic of low Reynolds number flows (50,000<Re<500,000) in which conditions small perturbations in a laminar boundary layer are coherently amplified over a laminar separation bubble or separated shear layer. These amplified instability waves pass the trailing edge and scatter sound. On top of this, this scattering propagates upstream and initiates new instability waves, creating a self-perpetuating feedback loop.

In a contra-rotating system, the effects of the rotor-rotor interactions are expected to predominately change the loading noise [14]. This is a period variation and as such, this study has been aimed to study tonal noise. Modeling the broadband noise is possible with methods such as Ref. [62] but generally breaks down with low Reynolds shown in Ref. [63], this study only models periodic noise due to the expected tonal distinctions between configurations.

2.3. Contra-Rotating Propellers

Building upon the fundamental case of a single propeller, introducing a coaxial contra-rotating propeller brings about propeller interactions. This section delves into the literature to illustrate potential shifts in the loading noise induced by the CRP. The literature also highlights specific geometric considerations, which are presented here for contextual comparison. Concluding this section, a preliminary analytical model for the CRP setup in forward flight offers a deeper understanding of the underlying mechanisms.

2.3.1. Additional Noise-Generating Mechanisms

Introducing an additional propeller in an aircraft system impacts its acoustic profile through two fundamental aspects: *aerodynamic installation effects* and *acoustic installation effects*. The former involves noise variations due to alterations in flow characteristics [64], while the latter encompasses changes in sound propagation, such as scattering and acoustic interference [65].

In contra-rotating propeller configurations, despite not introducing new sources, the interplay between the two rotors amplifies unsteady-loading noise, primarily driven by interference between the two rotors [7]. This amplification stems from two underlying factors: The first pertains to the downstream convection of the wake generated by the leading propeller, which subsequently interacts with the rear propeller. These are the viscous wake effects and they only affect the rear propeller. The second phenomenon involves a propeller distorting the potential field around it, the proximity to the other propeller affects the inflow of the second propeller. Both processes are unsteady, stemming from their reliance on the rotational position of the initiating propeller and perpetually encountered by the blades of the opposing propeller in the propeller's rotating reference frame, leading to periodic noise.

The resultant noise not only presents typical BPF harmonic tones but also gives prominence to interaction tones, generated through the sum of the BPFs of the upper and lower propeller. When the blade number and rotation rate of the propellers are identical, these tones emerge on the even multiples of the BPF harmonics. Conversely, if these parameters differ, interaction tones surface in the frequency spectrum at the sum of the individual BPF of each propeller, formulated as $\omega_{mn} = mB_1\Omega_1 + nB_2\Omega_2$ [13, 14]. Refer to Figure 2.8 for a conceptual diagram illustrating these principles.

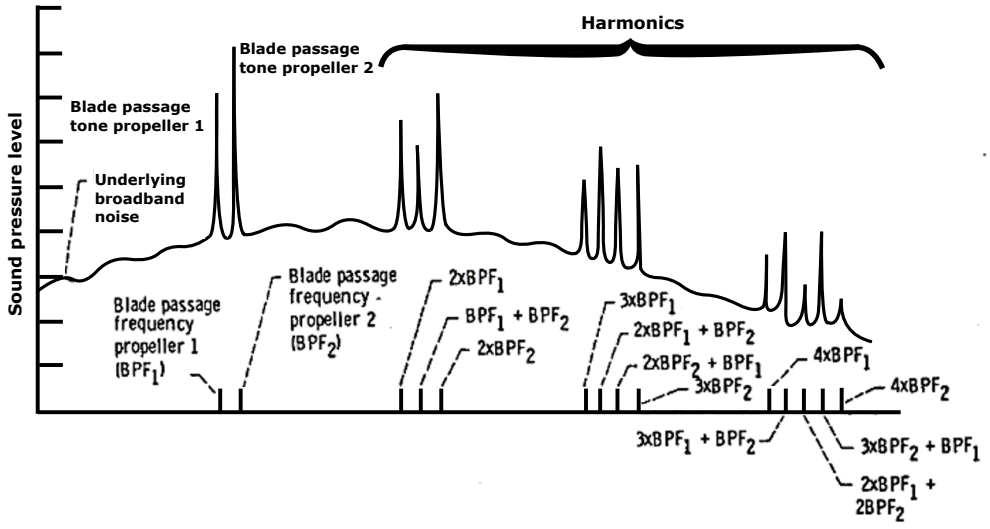

Figure 2.8: Example frequency spectra for contra-rotating propellers at different RPM values showing interaction tones. [12]

Chaitanya et al. [13] further categorize the noise sources into three primary categories: propeller self-noise, propeller installation noise, and propeller-propeller interaction noise. In that study of contra-rotating propellers, the dominant noise source has been identified as the propeller-propeller interaction noise on the downstream propeller, induced by various factors such as blade lift downwash, velocity deficits drag, and tip vortices [7]. Furthermore, interactions can amplify propeller self-noise due to blade-vortex interaction (BVI) and blade-wake interaction (BWI). BVI occurs when a vortex created by the blade tip impinges on the succeeding propeller, whereas BWI is when a wake generated by a leading propeller interacts with a subsequent blade.

2.3.2. Parameters Effects

In the literature, there are several design choices that impact the interaction of sound production. In 1985 Dittmar split these into two categories: reducing the strength of the wakes and vortices from the upstream propeller and reducing the response of the downstream blades to the wakes and vortices [12].

In the first method, the following parameters were introduced: spacing, drag reduction, sweep, lean, and avoidance. A model for the velocity deficit equation for an open single propeller's wake is written as,

$$v/U_\infty = \frac{2.41\sqrt{C_D}}{(z/c + 0.3)}, \tag{2.18}$$

and indicates that the spacing, z/c, influences the velocity deficit of the propeller as the wake convects downstream. This shows the change in velocity experienced by the rear propeller diminishes downstream or with a smaller propeller chord. Also, using an airfoil section design to reduce the propeller's drag will impact the second propeller's noise, even if it is a frequent design decision for other reasons.

To reduce the strength of vortex impingement downstream one method is to prevent the vortices from coming into contact with the propellers. To do this, the radius of the aft propeller can be shortened, or a nacelle can be used to push the flow out axially, however, the proximity of the vortices can still change the loading, making this a complex interaction. The effects of spacing on BVI are complicated due to the reduction of strength during convection but also the radial contraction of the vortex structure.

Finally, an overall reduction of circulation on the propeller may include using fences on the blade if size allows or pitch and twist angle changes.

The study by Chaitanya et. al. [13] gives insight into both optimal blade row (propeller) spacing and contributions of different noise sources for contra-rotating propellers and is one of few concerning near hover conditions. Because this analysis considers a zero net torque reaction, the separate propellers have different thrust values but rotate at roughly the same speed.

When the same propellers are utilized, an ideal propeller spacing of $z/D = 0.25$ is effectively independent of total thrust. Near this optimum, the sound power level varies with thrust, but it becomes independent of thrust away from the optimum because of the large increase in interaction noise. The ideal propeller spacing remains at a constant z/D ratio as the propeller diameter increases, while the overall sound power level decreases when thrust is maintained.

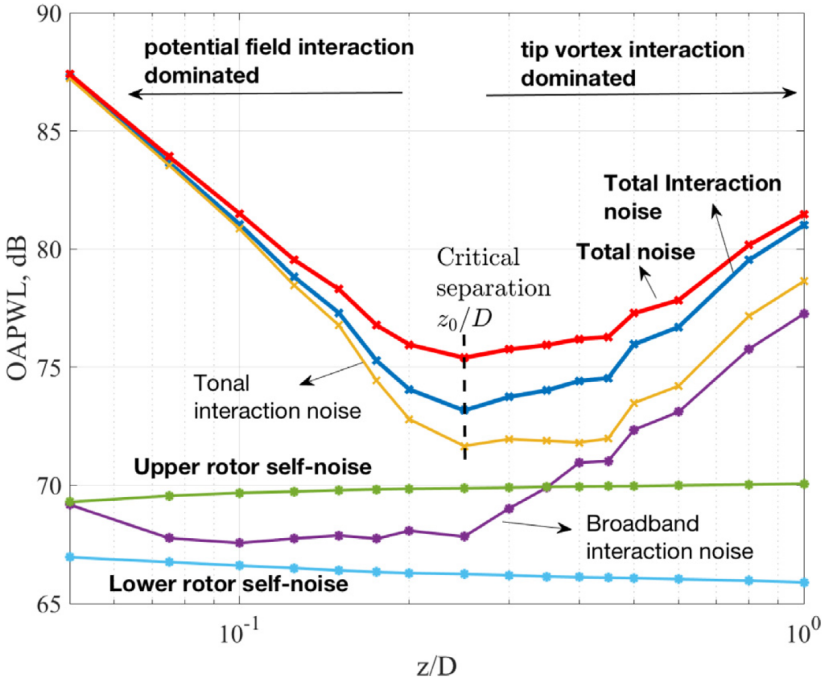

Figure 2.9: Breakdown of noise source components at different blade row spacings for a fixed combined thrust of $16N$. [13]

The breakdown of noise source contribution is best detailed in Figure 2.9 but, overall, from this study, it was found that the interaction noise is always dominant. Broadband noise interaction increases as separation distances exceed the optimum due to vortex impingement increasing turbulence on the downstream rotor.

Another configuration investigated by Chaitanya et al. [13] concerns propellers of mismatching diameters. In the study, the combined thrust value is maintained by changing the rotation speed of the aft propeller leading to an analytical derivation such that the overall sound level is proportional to $N^{5.5}D^7$ which was experimentally validated.

The optimum separation distance is found to decrease as the RPM of the smaller downstream rotor is raised. This is due to a decrease in the potential field interaction as well as an increase in the noise due to tip vortex interaction. The spacing effects in Figure 2.9 are generally upheld in this study.

Additionally, the tonal increase only occurs at harmonics of the downstream rotor which shows the increased strength of the tip-vortex impingement. From this, the cropping of the rear rotor was found not to unilaterally decrease the noise of the system as would have been predicted rather, it was found that the position of the tip vortex interaction with the downstream rotor and the operating conditions significantly influenced the sound.

Potential Field Interaction Effects

At separation distances $z/D < 0.25$ tonal noise contributions are dominant due to the interaction of the rotor potential field with the subsequent rotor according to Figure 2.9. The figure does show a

difference between upper and lower rotor self-noise but this is due to the difference in the thrust that the individual propellers are generating rather than wake-rotor interactions.

Chaitanya et al. [13] identify the dominance of potential field interaction through two key observations. First, at close separations, the amplitudes of even-harmonic frequency tones exceed those of odd harmonics. This phenomenon occurs because all tonal frequencies resulting from interaction must manifest at even harmonics, given that $B_1 = B_2$ and $\Omega_1 = \Omega_2$.

Secondly, the even harmonic multiples of blade passage frequency (BPF) diminish exponentially as propeller spacing increases, while the even multiples remain largely unaffected by this difference. This leads to the conclusion that the even BPF multiples are primarily influenced by the potential interaction of the propellers, whereas the odd multiples are solely attributed to rotor-generated sources. Consequently, the tonal amplitudes at odd harmonic frequencies must originate solely from the rotor itself.

Additional Parameter Comentary

The existing literature reveals a gap in comprehensive studies focusing on various factors that play a critical role in shaping wake dynamics and blade responses of contra-rotating propellers during hover or near-hover conditions, such as the effects of Reynolds Number, chord length, and more [13]. Specifically, these parameters determine the shape, angle, and velocity deficit of the wake created by the first propeller and, therefore, the response that occurs from the second propeller. This leads to the understanding that adjustments to components, such as the sweep angle and tip shape, can significantly impact wake and vortex behaviors. Thus, while the noise-generating mechanisms identified in this thesis are consistently present, they may manifest differently based on the exact geometry.

2.3.3. Analytical CRP Model

An extension of the theory for a single propeller (Equation 2.10) to contra-rotating propellers is presented by Hanson in 1985 [14]. This formulation accounts for both aerodynamic interference between the rotors and the reinforcement and cancellation of the acoustic fields of the two rotors. The paper also uses a theoretical model for the potential wake which can be substituted with experimental or numerical data.

Ref. [14] produces a general formula that works for both open contra-rotating propellers and turbofans. A specific case where $B_1 = B_2 = B$ and $\Omega_1 = \Omega_2 = \Omega$ is also presented. This is the same condition as this study and is given in Equation 2.19.

$$
\begin{aligned}
p = & \frac{-i\rho_0 c_0^2 B \sin\theta}{8\pi\left(r_1/D\right)\left(1 - M_x \cos\theta\right)} \sum_{m=-\infty}^{\infty} \sum_{k=-\infty}^{\infty} \exp\left\{ i\left[(m-2k)B\left(\phi - \phi^{(2)} - \frac{\pi}{2}\right) + mB\left(\frac{\Omega r}{c_0} - \Omega t\right)\right]\right\} \\
& \times \int_{\text{root}}^{\text{tip}} M_r^2 e^{i(\phi_0 + \phi_S)} J_{(m-2k)B}\left(\frac{mBz_0 M_T \sin\theta}{1 - M_x \cos\theta}\right)\left[k_x \frac{C_{Dk}}{2}\Psi_{Dk}\left(k_x\right) + k_y \frac{C_{Lk}}{2}\Psi_{Lk}\left(k_x\right)\right] \mathrm{d}z_0
\end{aligned}
\tag{2.19}
$$

In this formulation Ψ_{Dk} and Ψ_{Lk} are "nondimensional transforms of chordwise distributions of drag and lift such that the product $C_{Lk}\Psi_{Lk}$ is equivalent to a lift response function times the quasi-steady lift coefficient" [14]. Thus, representing these values in both the lift and drag direction describes the sources on the propellers and includes the influences of the potential field and wake on both propellers.

The summation over the modes where k is the order of the load harmonic and m is the sound harmonic. The combination of these two indices dictates how much a source at a specific frequency influences the listener at a specific frequency. This is modulated by the Bessel Function (first kind), $J_n(x)$.

The remaining variable simply describes the propellers and their operating condition where M_T is the blade tip rotational Mach number, M_r is the blade section relative Mach number, M_x is the flight Mach number, B_D is the chord-to-diameter ratio, ϕ is the azimuthal observer angle, and θ is the observer angle from the axis. $\phi^{(2)}$ represents the blade angle at time $t = 0$ while ϕ_0 and ϕ_s are phase angles associated with offset and sweep. Also included in the formula are k_x and k_x which are further expressions based on M_T, M_r, M_x, m, B, B_D, k, and θ.

The model presented here was compared with experimental results from a test flight, as documented in Ref. [14]. Figure 2.10 illustrates the remarkable agreement between the model's predictions and the

experimental data, which were obtained in the plane of the rear rotor while the aircraft was flying at cruise speed.

The study's conclusion emphasized the need for refining the "aerodynamic interference model." It's essential to recognize that the measurements taken in this study pertained to a very different flight regime and propeller design compared to what will be investigated in the current thesis project. Therefore, only relevant conclusions are presented here.

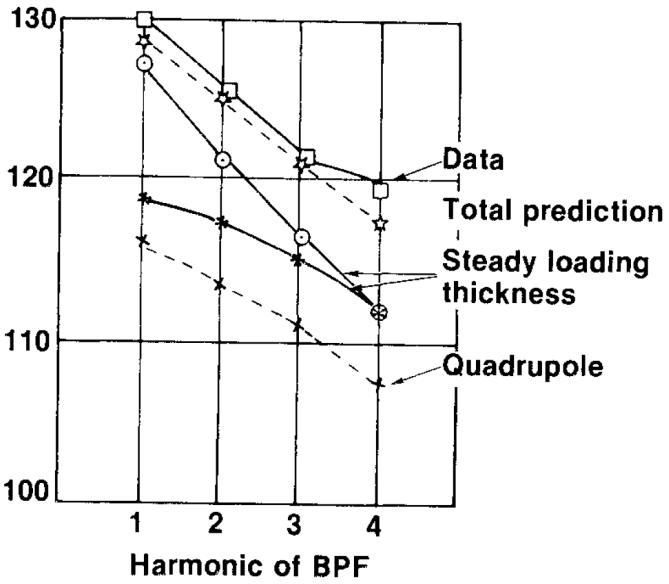

Figure 2.10: Comparison of noise components predicted by the methodology presented in this section with experimental data gathered from a test flight of a Fairey Gannet [14].

2.4. Shroud Effects and Design

This section covers two primary topics. The first addresses the design of the shroud, detailing the function of its components and explaining the underlying flow theory. From there, literature findings provide insights into an optimized shroud design that informs this study. The second topic introduces noise-generating mechanisms and performance characteristics of both single and contra-rotating shrouded propellers that are known in the literature.

2.4.1. Shroud Design

In this study, the shroud employed is of medium length relative to ducts explored in other research. When comparing the thrust, T, and power loading, denoted as T/P, of a ducted and un-ducted propeller, ducts of length $0.28D$–$0.53D$ show a larger increase compared to ducts shorter than the 0.15 propeller diameter [15]. However, this increase is less pronounced than that noted in prior studies for ducts exceeding 0.8 times the propeller diameter. For UAM applications the long duct design is not ideal given its excessive weight and space requirements.

The referenced study categorizes the shroud into three distinct parts: the inlet, the center, and the outlet, depicted in Figure 2.11. Each part uniquely influences both the thrust and propeller performance. These effects are analyzed in this section.

Shroud Effect on Propeller Perfomance

The influence of the shroud on the inflow profile is dependent on the design of the inlet as well as the remainder of the duct. The load distribution of the propeller blade can change due to the addition of a shroud and the largest factor in this change is the increase in axial velocity [66]. As the axial velocity increases, the angle of attack for the whole propeller decreases, as seen in Figure 2.12. Because propeller blades are normally designed at a given angle of attack, α, the addition of a shroud to a propeller system requires either the airfoil shape or the incidence angle, ϕ to be adjusted.

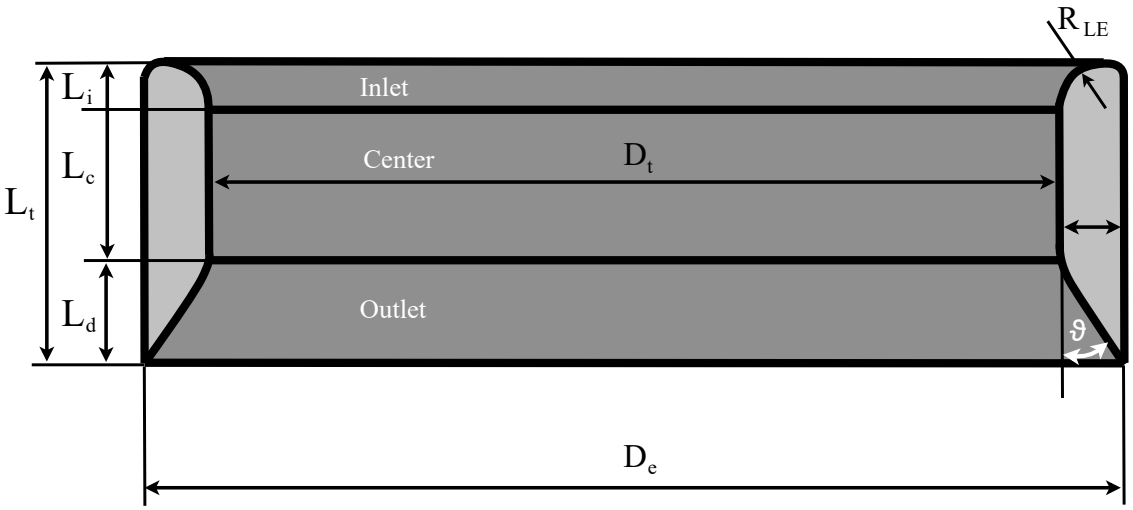

Figure 2.11: Shroud section definitions as used in Ref. [15].

A decreased angle of attack also increases the component of lift in the rotational direction (increase in β), this in turn increases the torque and reduces the lift of the propeller. If the blade angle is altered to maintain the angle of attack, this is amplified. Increased freestream velocity magnifies this issue, thus limiting shrouded operation to low advance ratios.

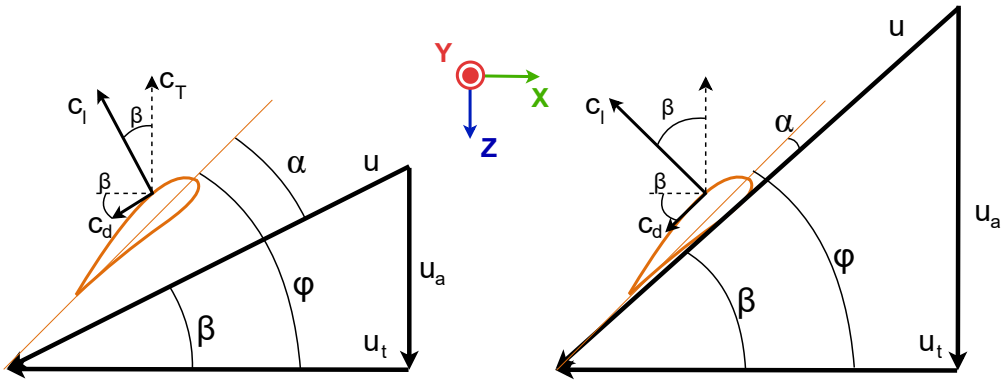

Figure 2.12: A velocity diagram comparing the effects of increased axial velocity on an arbitrary blade section at the same incidence angle [16].

Shroud Center Effect

The integration of a shroud introduces a barrier near the blade tip that limits the capacity of pressure differentials between the pressure and suction sides of the blade to generate vortices. This mitigates losses related to lift near the tip, yet it also exposes the tip to the influence of the shroud. The extent of interference by the shroud and its effectiveness in minimizing vortex generation is dependent on the distance between the wall and the blade tip, referred to as the ”tip gap,” denoted as δ_{tip} [18].

Shroud Inlet Design

The design of the should inlet is a fine balance as an inlet that is too sharp will cause separation due to the formation of a *vena contracta* while a large radius will suffer from skin friction drag [17]. However, the additional thrust of the shroud is due to a region of low-pressure suction forces acting on the inlet of the shroud.

The *vena contracta* is a phenomenon that occurs because the streamline of a flow cannot change shape and direction instantaneously. Thus, as shown in Figure 2.13, the momentum of the flow over a lip causes the flow to separate from the wall. This would create a non-ideal flow condition for the propeller inside the duct.

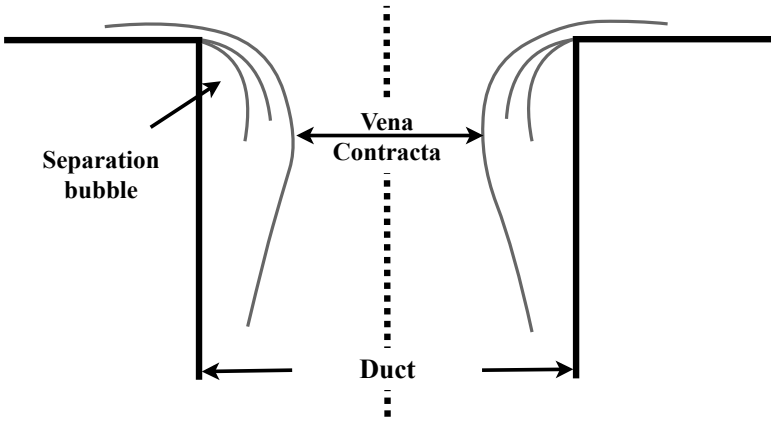

Figure 2.13: Depiction of vena contracta [17].

The most significant advantage of a shrouded design is the additional thrust it generates. In some instances, this extra thrust can constitute up to 40% of the system's total thrust. Airfoil-shaped shrouds create suction at the leading edge, producing thrust - predominantly from the inner half of the inlet's lip due to the flow's high velocity (up to 80% of the shroud thrust). This thrust is typically about four times the losses caused by a diverging outlet [18].

Consequently, the shroud's leading edge aims to facilitate flow entry into the duct with minimal separation, necessitating a smooth, rounded inlet that is neither too wide nor too abrupt. A gradual inlet radius of curvature generally minimizes losses from separation. Moreover, during hover, the shroud's external shape matters less since the leading edge generates all the thrust, and even the outer lip contributes minimally.

Shroud Outlet Design

The purpose of a diffuser is to reduce the exit velocity, which yields improved thrust efficiency of the propellers at a slight reduction of shroud thrust for a given propeller configuration.

Because of the pressure increase across the propeller, the portion of the shroud following the rotor plane (outlet) should diffuse the flow such that a full pressure recovery is made. In the case of an open propeller the stream tube contracts (the velocity increases), as seen in Figure 2.14(a), to account for the increase in pressure. This contraction is accompanied by a loss of power and can be partially recovered using a divergent section such as in Figure 2.14(b). The diffuser ratio, σ_d is defined in Equation 2.20 and is used to describe the expansion of the flow in the shroud.

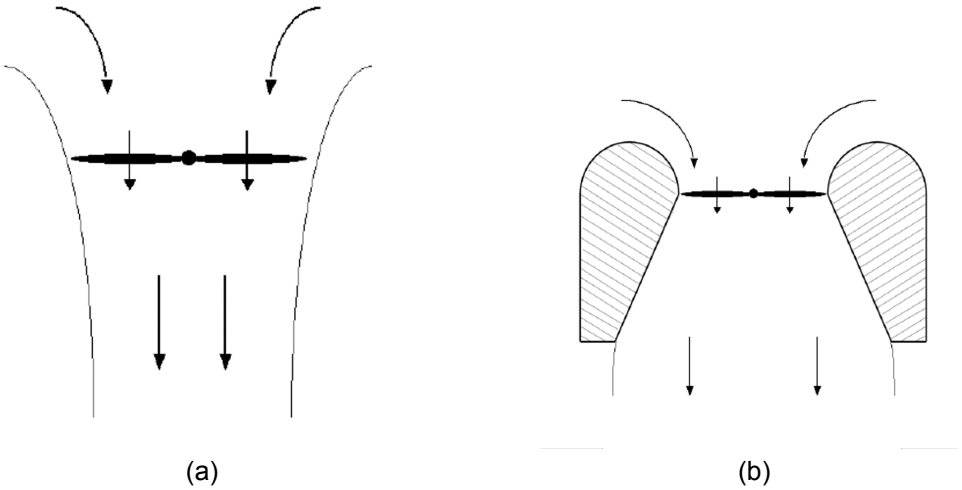

(a) (b)

Figure 2.14: A comparison of the streamtube from (a) an open rotor system and (b) a shrouded rotor system [18].

Using the BEMT formulation Equation 2.21 describes the relationship between the ideal power of a shrouded propeller system ($P_{i,SR}$) and the ideal power of an open propeller system ($P_{i,OR}$). In the case of the propellers having the same disk area ($A_{SR} = A_{OR}$) and the total thrust of both are the same such that $T_{SR} = T_{OR}$ (T_{SR} includes both the thrust of the propeller and shroud), then Equation 2.22 is reached [18]. From this formula the concept is clear, a larger expansion ratio significantly improves power requirements.

$$\sigma_d = \frac{A_{exit}}{A_{rotordisk}} \tag{2.20}$$

$$\frac{P_{i,SR}}{P_{i,OR}} = \frac{1}{\sqrt{2\sigma_d}} \left(\frac{T_{SR}}{T_{OR}}\right)^{3/2} \left(\frac{A_{OR}}{A_{SR}}\right)^{1/2} \tag{2.21}$$

$$\frac{P_{i,SR}}{P_{i,OR}} = \frac{1}{\sqrt{2\sigma_d}} \tag{2.22}$$

Theoretically, for a cylindrical, straight-sided shroud ($\sigma_d = 1.0$), the power requirement would already be 29% less for the same thrust (or it could produce 26% more thrust at the same power). It follows that a wider expansion is always more effective. However, because the derivation assumed inviscid flow, the formula does not account for the diffuser having an adverse pressure gradient. Now, the exact angle between the rotor disk and the exit becomes important, not just the expansion ratio.

According to Black et al. [67], increasing the diffuser angle from 8° to 14° can result in a 15% increase in static thrust, however, wider diffuser angles reduce the performance of ducted single propellers because they create flow separation brought on by skin friction drag and backpressure.

Optimal Design

In the experimental study presented by Pereira [18] an optimized solution is determined by testing a large range of values of the shrouded-rotor parameters. The optimal value was determined for a specific rotation rate quantified by maximizing the ratio of the FOM of the shrouded configuration to the FOM of the open propeller, $FOM_{max,SR}/FOM_{max,SR}$. The same result held for a range of rotational rates from $\Omega = 500$ RPM to 5000 RPM.

The optimum configuration within the investigated range of shrouded-rotor parameters from this study had a tip gap of $\delta_{tip} = 0.1\%D_t$, a shroud leading edge radius of $R_{LE} = 13\%D_t$, a diffuser angle of $\theta = 10°$, and a diffuser length of $L_d = 50\%D_t$ to $72\%D_t$ where D_t is the shroud throat diameter. Performance was degraded by altering the blade tip clearance, the inlet lip radius, the diffuser length, and the diffuser angle from these optimum values. The momentum theory (Equation 2.22) predicted that performance would improve with increasing expansion ratio (σ_d), and this was observed to be true up to an expansion ratio of about 1.2. Performance suffered when σ_d was increased over this point, regardless of whether the diffuser's length or angle was increased.

The effects of changing δ_{tip}, R_{LE}, θ, or H would compound with one another. Since the degree of each parameter's influence relies on the values of the others, it is impossible to definitely say that one parameter has a bigger impact on performance than another. The lip radius appears to be the exception to this rule, as changes in this parameter had essentially the same effects regardless of the values of the other parameters.

As a result, it would appear that deviating the value of any shroud parameter from the optimal to increase performance results in a reduction in the performance's sensitivity to changes in any other parameters. Likewise, increasing the rotor's efficiency would appear to reduce the performance benefit from the presence of a shroud.

2.4.2. Single Shrouded Propellers

An experimental acoustic analysis of a shrouded single propeller revealed that the OSPL, directivity, broadband noise, and tonal noise are altered by the presence of a shroud [19]. The study investigates the impact of ducts on noise characteristics and directionality in two scenarios: an omni-directional source without incoming airflow and a propeller operating at 85% of maximum power without incoming airflow. Key outcomes include changes in power spectral density (PSD), noise directionality, and the identification of noise sources through beamforming analysis.

In the case of the omni-directional source without incoming airflow, the presence of a duct induced periodic changes in the PSD, consistent with sound propagation behavior in ducts. This included the emergence of resonance and anti-resonance frequencies. Noise directionality was moderately affected, with localized reductions of approximately 2 to 3 dB at specific positions. Notably, a slight reduction of around 1 dB was observed at the center of the duct, primarily due to sound diffraction at the duct's edges. Additionally, constructive interference led to noise reinforcement of about 2 dB at the top and bottom of the microphone array.

When the propeller operated without incoming airflow, the introduction of a duct resulted in increased noise levels across most frequencies, except for the first harmonic. Harmonics present in the isolated propeller were no longer visible above 2 kHz with the duct. Noise directionality exhibited significant alterations, with noise levels increasing by up to 12 dB at the top and bottom of the microphone array (Figure 2.15). Interestingly, the center of the array experienced the lowest increase in noise levels. These changes in the power spectral density and directionality were attributed to the creation of additional broadband noise sources, such as trailing edge noise, due to interactions between the propeller and the duct.

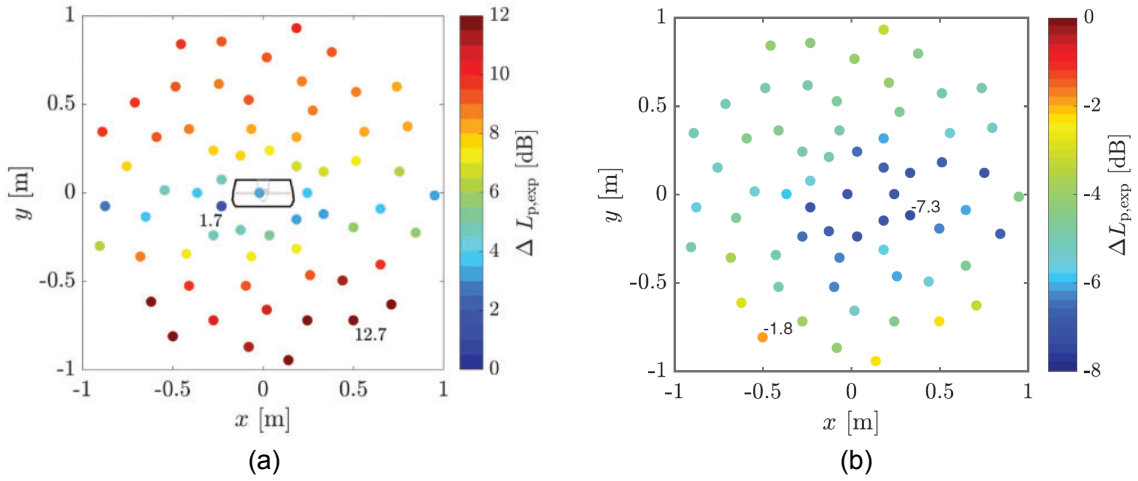

Figure 2.15: (a) Change in overall sound pressure level of a propeller at 7500 RPM due to shroud in quiescent conditions. [19] (b) Change in sound pressure level of a propeller at 7500 RPM due to shroud with an inflow velocity of 10 m/s [19].

In a scenario with an inflow velocity of 10m/s with the duct, a slight increase in broadband noise and a significant reduction in harmonic noise levels across all microphones are observed. As in the case without inflow velocity, lower noise levels remained centered in the microphone array as shown in Figure 2.15(b). Unlike scenarios without airflow, the duct introduced an additional noise source, possibly stemming from the interaction between propeller tip vortices and the duct walls. This source persisted due to the absence of upstream airflow, as evidenced by its similarity to the gray line representing typical duct propagation. Notably, this new source was absent in scenarios with airflow, reshaping the overall noise profile of the isolated propeller.

This additional source was determined from a beamforming analysis to identify noise sources and patterns for both the omni-directional source and the propeller scenarios. Additionally, for the omni-directional source, noise reduction primarily occurred at the leading edge, whereas noise amplification revealed sources of equal magnitude on both the leading and trailing edges of the duct, reflecting frequency-dependent variations in duct propagation. For the propeller, noise sources without the duct did not precisely align with the propeller plane, especially for certain tones. However, the introduction of the duct increased the strength of noise sources, and a new source was identified at the leading edge, confirming the impact of resonance and turbulent flow interaction with the duct on noise levels. Figure 2.16 helps to depict the sources mentioned above.

Similar effects were shown as early as 1949 by Hubbard (Ref. [68]) where applying a shroud always has lower sound pressure levels near the rotor plane. A correlation with the separated flow was discovered from this investigation as well. It was discovered that the addition of the shroud (for a constant rotational speed) resulted in overall sound pressure levels that were up to twice as high as the isolated propeller in cases where the flow separated inside the shroud, but with the unseparated flow the sound

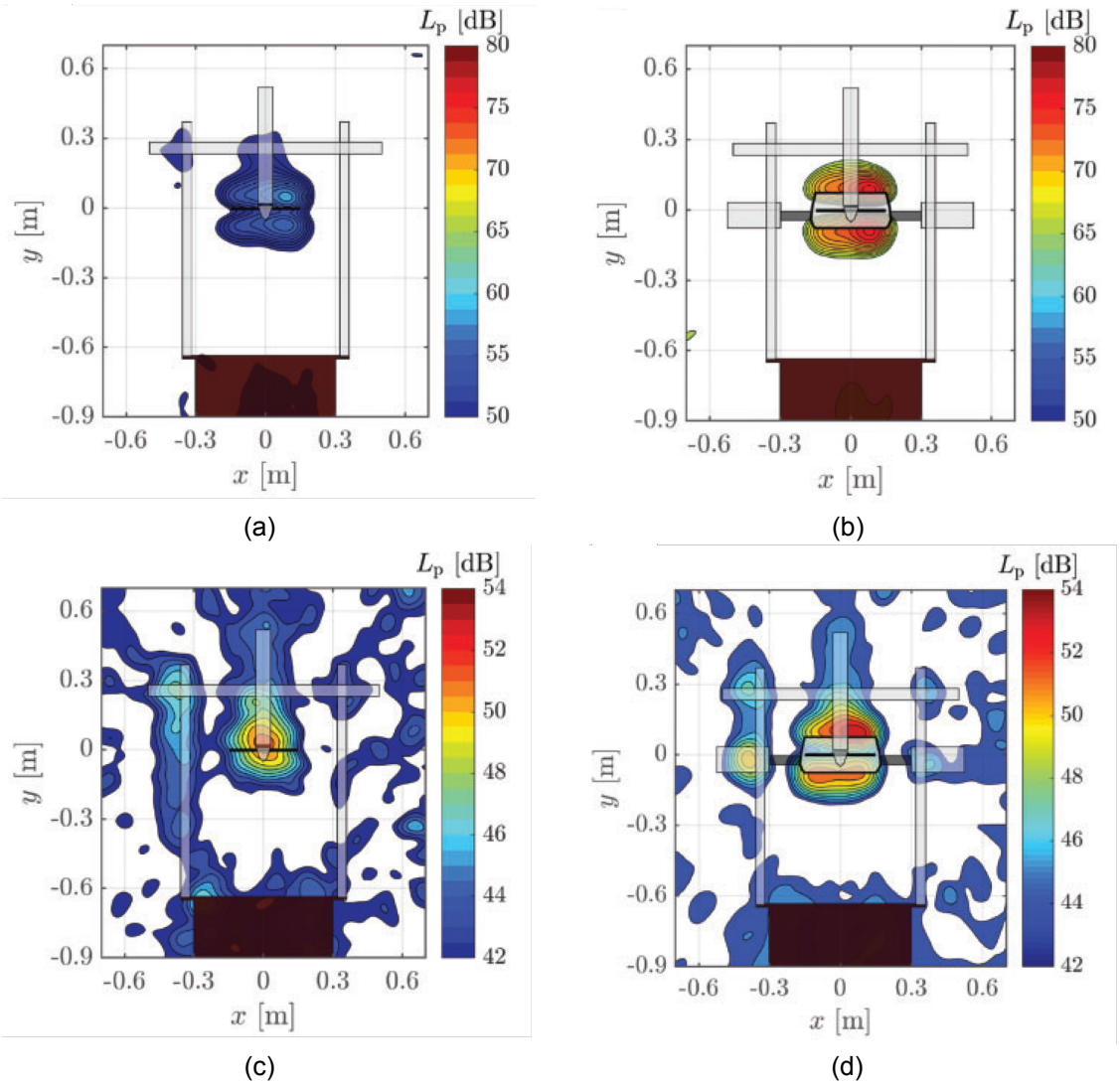

Figure 2.16: Beamforming results for (a) an isolated propeller, with no incoming airflow, (b) a ducted propeller, with no incoming airflow, (c) an isolated propeller, with a constant incoming airflow, and (d) a ducted propeller, with a constant incoming airflow. [19]

levels could be as low as half of the isolated propeller. With separated flow, all frequencies related to rotational sound are reinforced and unsteady noise is increased whereas the converse is true in unseparated flow. The study also found that for the same tip speed and power coefficient increasing the number of blades of the propeller reduces the total sound emission. In the experimental results increasing the blade number from 2 to 5 reduced the sound pressure by a factor of 1.5 to 3 depending on the directivity.

A numerical approach to the analysis of shrouded propellers including optimization published by Zhang and Barakos [35] in 2021 gives further insight into how the shroud changed the inflow conditions and altered the performance. Although this optimization is not targeted for hover conditions, the higher advance ratios are still very low (≈ 0.2) and are relevant in a study near hover. The study used airfoil-like cross-sections for the shroud and saw that the propeller loading is reduced and up to 50% of the thrust comes from the shroud depending on the configuration. At hover and low speeds, the shrouded propeller was typically more efficient than the open propeller but, at higher advance ratios this is not the case.

The study included a performance optimization that changed both the duct shape and the blade twist and improved the performance at higher advance ratios but slightly penalized lower advanced ratios and cross-wind performance. The optimizer decreased the expansion ratio of the duct and inverted the

camber of the inlet. This design caused the shroud to induce less change for the inlet velocities and mass flow through the disk, improving the overall thrust. The global blade pitch was also increased to accommodate higher inflow velocities although it was changed less when both variables were coupled.

The acoustics analysis took into account the final optimized designs as the shrouded and unshrouded based-line geometries. The difference between the shrouded and unshrouded shows a reduction of 5-10 dB in the far field. This reduction is also attributed to shielding from the shroud. In the optimized cases it is shown that when only the blade twist is optimized in the presence of the shroud, there is a negligible effect on the sound level and directivity. Conversely, changing the shape of the shroud and the coupling of the two parameters leads to a change in the directivity but, the mean OSPL level does not change.

When these investigations, both experimental and numerical, compare the performance of shrouded propellers to open propellers they typically use the same design of propeller to determine the effects of the shroud. Therefore, the propeller utilized is no longer designed to have the optimal performance for its application because of the variable inflow to the propeller caused by the shroud. This study from Zhang and Barakos [35] shows that performance can be improved by changing the twist thus, it is likely that other changes, such as chord distribution, sweep, and lean can also change the performance by optimizing the circulation distribution.

The performance of the propeller itself does not vary considerably when the tip gap is changed, the effects on the duct account for the majority of the performance fluctuation [16, 18, 69]. This is not always the case, as demonstrated by Akturk and Camci [70] where they employed a large number of blades and found that the tight spacing between the blades allowed for interaction between one blade and the leakage from the blade before it. For noise, a smaller tip gap is shown to produce more noise at the same rotation speed, however, at the same level of thrust decreasing the tip gap reduced the noise in almost all directions due to increased broadband noise [16].

2.4.3. Shrouded Contra-Rotating Propeller

Research indicates an increase in the overall thrust when a shroud is integrated with a contra-rotating propeller. One study highlights a surge of up to 25% in the thrust coefficient [15], while another reports a 61.2% in total thrust [34]. These same studies also report an increase in power loading by up to 50% and 60%, respectively. However, the performance of both the open CRP and S-CRP drops off sharply after the maxima. The design parameters studied in these two reports were focused on shroud design.

The study from Huo and Liu [34] reports that a large inlet and a divergent nozzle greatly improve the system performance compared to a cylindrical or convergent nozzle, but this is limited by flow separation. Additionally, they found no performance sensitivity to propeller location within the shroud and only a small improvement in power level when comparing the S-CRP to the CRP.

In that study, the addition of the shroud allowed the rear rotor to play a more significant role in thrust generation because the shroud contained propeller interactions and wake developments. The propeller speeds also influence the performance as it ”[behaved] better when the upstream rotor rotates more slowly than the downstream rotor” [34].

Another study from Zhao and Shkarayev [15] further determined that the thrust of the system decreased with an increased advance ratio (Figure 2.17), showing that the test geometry is significantly better performing in hover and hover-like conditions attributing the reduced performance to an increase in drag on the outer surface of the shroud.

Experimental aeroacoustic results are presented in the study by Koenig et al. [37], however, this only takes into account the shroud’s effect on propeller performance because the tested shroud does not produce any thrust on its own. It also uses small shrouds compared to the studies shown previously, which are tested in many configurations including encasing and not encasing the propellers. Thus, the paper focuses on how shrouds can vary the performance and sound level mostly by altering the flow.

The best design presented for a non-thrusting shroud maintains the streamtube shape characteristic of an open propeller, as increased performance is achieved through effective airflow expansion. The design that demonstrated the highest performance enhancement, quantified in terms of FOM, was one where the shroud encompassed only the downstream propeller. This particular configuration also led to a minor reduction in OSPL.

This reduction can be attributed primarily to the diminished presence of the first harmonic, which is consistent across both propellers, with the remainder of the acoustic domain either matching or exceeding the levels identified in the open rotor setup. The specific factors contributing to this subtle

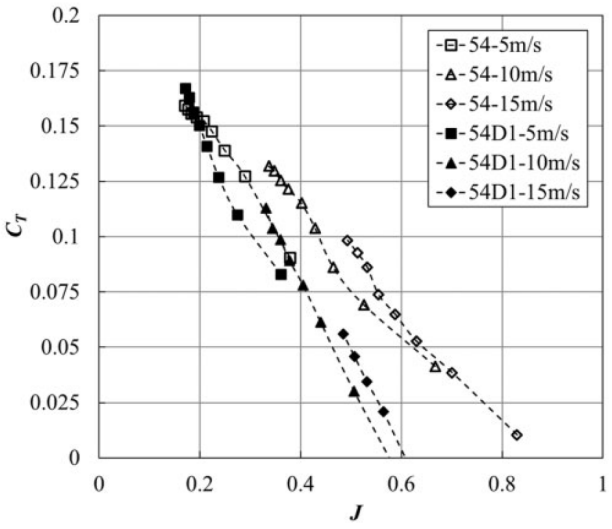

Figure 2.17: Experimental results showing how quickly performance decreases with increases advance ratio for an S-CRP configuration. [15]

change were not elaborated upon, likely due to their minimal impact.

In contrast, another configuration using a rounded shape similar to the streamtube-inspired design, registered the most substantial decline in OSPL, accompanied by a marginal rise in FOM. The study did not extend to an exploration of the underlying causes of these observations.

Besides the two best designs, the study by Koenig et. al. [37] gave a few additional trends to consider when designing non-thrusting shrouds for a contra-rotating system. The design results are similar between a single propeller and a coaxial propeller system suggesting significant transferability of concepts between the two systems. Reducing the tip gap gave similar results as Ref. [18] and Ref. [69] where reduced spacing increased OSPL but, this study shows that efficiency increased with a lower gap.

Expectations for S-CRP

The following influences are predicted based on these observations and extrapolation from shrouded single propellers (found to be feasible in ref. [37] which showed very similar results between the two) and contra-rotating propellers:

- Shroud should fully expand the flow without having flow separation to produce the best performance and noise emissions.
- A shroud will cause a lower noise near the rotor plane compared to the rest of the field
- Noise production is positively correlated with and performance is negatively correlated with advance ratio.
- Blade pitch will impact the performance of any rotor system and rotor interaction noise but, not propeller self-noise or the sound generated by the shroud.
- Interaction noise will remain the dominant noise source for the propellers in the presence of a shroud.

When extrapolating information from the other configurations certain trends can not be predicted for the full shrouded contra-rotating propeller configuration. For example, for shrouded single propellers it was found that the tip gap varies inversely with noise and impacts shroud performance, however, increasing the tip gap increases the vortex strength which, in a CRP configuration typically increases the interaction noise.

Similarly, the influence of spacing between the blade rows in CRP is well understood but interaction phenomena are expected to significantly change with the introduction of the shroud. Likewise, the results of adding more blades to either blade row are unknown.

In a CRP system, it is anticipated that this would decrease the response from the rear rotor, as more blades lead to less velocity fluctuation magnitude. However, more blades are also shown to interact

with the leakage from the radially preceding blades due to reduced radial spacing between blades. Other parameters, such as chord length and circulation distribution are also not wholly predicted by the literature.

3

Methodology

The approach employed in this study is a split methodology solving combining the flow field solution, using the unsteady Reynolds-Averaged Navier-Stokes (uRANS) equations, with a Finite Element Method (FEM) application of the *Source Mode* formalization based on Ffowcs-Williams and Hawkings (FWH) analogy. This methodology has been previously investigated for propeller-wing interactions and a quadcopter drone configuration in Ref. [1] and Ref. [51], respectively.

Complementing this numerical study, an experimental campaign is currently ongoing at the von Karman Institute for Fluid Dynamics (VKI), with results for open single and contra-rotating propellers available in Ref. [71]. The campaign yielded the geometrical definition as well as aerodynamic and acoustic data. Because this reference will be used in multiple publications it is logical that it is used as a baseline here, ideally designed or not.

3.1. Geometry description

This study examines six configurations, with a primary focus on open contra-rotating propellers and shrouded contra-rotating propellers (see Figures 3.1(e) and 3.1(f)). To evaluate the impact of different components, simulations of two open single rotors and two shrouded single rotors are also performed (Figures 3.1(a-d)).

Figure 3.2 illustrates the variables as referenced in simulations and results, defining parameters related to propeller position, propeller characteristics, and shroud features. For the propeller position the diameter of the propellers, D, the distance between the propellers, d, the distance downstream from the base of the lead propeller, d_1, and the distance downstream of the base of the rear propeller, d_2. The lead propeller is shown where φ_i is the section twist of the blade, Θ is the azimuthal angle of rotation (defined as positive in the direction of rotation for the respective propeller), and Λ is the sweep angle. For the shroud, the leading edge radius is defined as R_{LE} and the diffuser angle is ϑ. Lastly, the tip gap is denoted δ_{tip}.

The VKI experimental campaign utilized a coaxial shaft, fitted with two *Mejzlik* 13×4.2 propellers, designed to rotate in opposite directions, available in both 2-bladed and 3-bladed versions. The propeller spacing can vary from 20 mm to 30 mm ($0.06 < z/D < 0.12$). The shroud is a custom design by VKI with an airfoil cross-section design to generate thrust and the same propellers will be used in both the open and shrouded contra-rotating case.

Both experimental and simulation baseline cases utilized the two-bladed propellers, each rotating at 6000 RPM and estimated to exert about 10.6 N of force per propeller under isolated static conditions [72]. The counter-rotating configurations are set to the maximum propeller spacing of 3 cm, with the upstream (lead) and downstream (rear) propellers rotating clockwise and counter-clockwise, respectively, as viewed from upstream.

The shroud's design employed in both this study and the subsequent experimental campaign adheres to the optimal parameters identified in Ref. [18] and elaborated upon in Subsection 2.4.1. This design specifies a shroud leading edge radius (R_{LE}) constituting 13% of the shroud throat diameter (D_t), alongside a diffuser angle (θ) set 10°. It also establishes a tip gap (δ_{tip}) at 0.1% of D_t. Although the chosen diffuser length (L_d) of $25\%D_t$ falls below the optimal range, the study still indicates that this

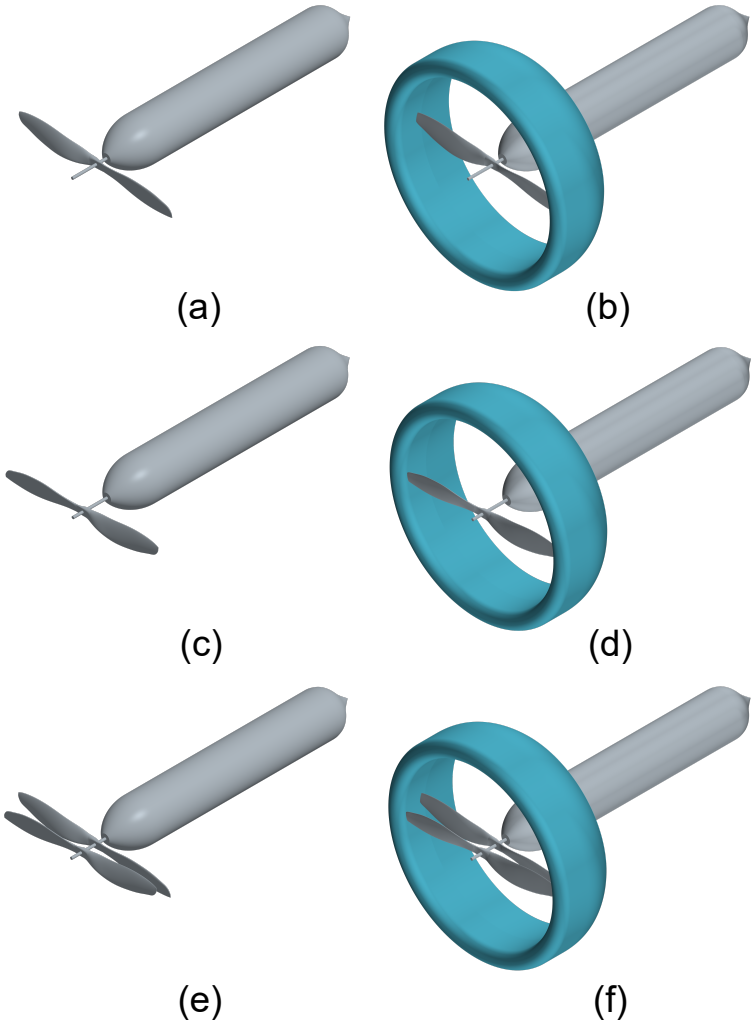

Figure 3.1: (a) Open single propeller in the rear position (b) Shrouded single propeller in the rear position (c) Open single propeller in the lead position (d) Shrouded single propeller in the lead position (e) Open contra-rotating propeller (f) Shrouded contra-rotating propeller

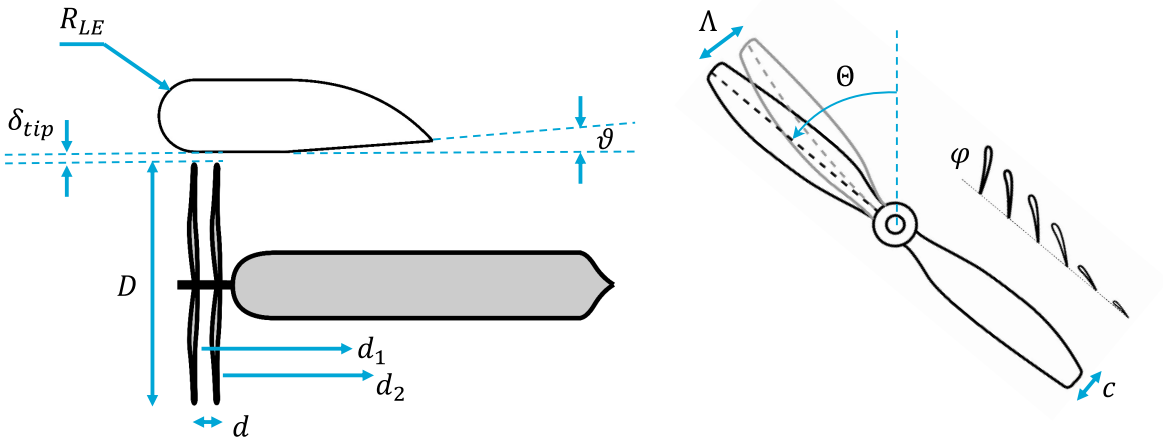

Figure 3.2: Geometrical definitions of numerical and experimental setup including both the shroud, propellers, and possible sweep variables (not to scale).

length still increases the system's thrust relative to that generated by open propellers. The objective of this design strategy is to maximize the thrust derived from the shroud, to slightly increase the efficiency of the propellers by facilitating flow expansion, and to achieve these performance enhancements within a compact shroud structure, thereby contributing to weight minimization.

To achieve a uniform tip gap between the propeller and shroud, the original propellers utilized in the open rotor cases were slightly altered, with approximately 3.7% of the propeller radius trimmed, maintaining the original twist distribution. This difference in blade shape must be considered when analyzing the difference between the configurations.

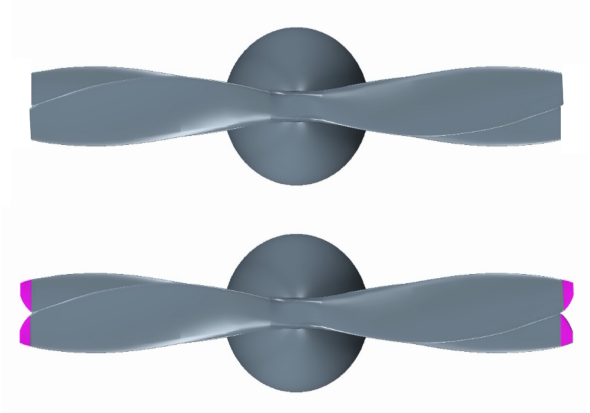

Figure 3.3: Visual representation of the trimmed portion of the propeller.

For the full-length, open-rotor propeller, the longest chord is roughly 2 cm, and the maximal thickness is approximately 1 mm, giving a tip tangential velocity of ≈ 103.74 m/s and a peak Reynold's number of $250,000$. From this, the expected maximum boundary layer thickness is expected to be 0.37 mm.

3.2. Computational Fluid Dynamics Solver

This section introduces the initial phase of the hybrid uRANS-FEM methodology, focusing on the aerodynamic solution. Although the foundational principles discussed here would be integrated with Chapter 2, they are presented in this context to ensure a coherent understanding. This approach aids the subsequent subsection, which delves into the application of the commercial solver.

3.2.1. Fundamentals for Reynolds-Averaged Navier-Stokes

Unsteady Reynolds-Averaged Navier-Stokes (uRANS) simulations will be utilized in the thesis project to solve flow field variables and calculate aerodynamic forces on surfaces, as well as surface pressure fluctuations that radiate noise.

The Reynolds-Averaged Navier-Stokes (RANS) equations are a set of mathematical equations that describe the steady-state or time-averaged behavior of fluid flows. These equations are solved using numerical methods such as finite volume or finite element where the flow domain is discretized into small computational cells and the equations are solved for each cell. The resulting system of equations is then solved iteratively to obtain the flow characteristics. This can also be solved in a series of time steps to capture unsteady behavior (uRANS).

To describe non-linearity (turbulence) in the formulation, the Reynolds Stress Transport equations can be derived with terms that describe the advection, production, diffusion, dissipation, and pressure strain correlation of the Reynolds stress. Each of these also has non-linear terms creating the closure problem of turbulence, requiring modeling. The two most popular models are the $k-\varepsilon$ *model* [73] and the $k-\omega$ *model* [74].

The $k-\varepsilon$ *model* is a two-equation model with a derived transport equation for the turbulent kinetic energy, k, and a postulated transport equation for dissipation, ε. This solution assumes that a linear relation between Reynolds stress and the strain rate tensor can be found for isotropic turbulence; this does not hold in most real flows and boundary layers but gives good results quickly in external flows far from walls. The $k-\omega$ *model* is also a two-equation model with a transport equation for the turbulent kinetic energy, k, and a specific dissipation rate, ω.

The $k-\varepsilon$ *model* is a two-equation model with a derived transport equation for the turbulent kinetic energy, k, and a postulated transport equation for dissipation, ε. This solution assumes that a linear relation between Reynolds stress and the strain rate tensor can be found for isotropic turbulence; this does not hold in most real flows and boundary layers but gives good results quickly in external flows far from walls. The $k-\omega$ *model* is also a two-equation model with a transport equation for the turbulent kinetic energy, k, and a specific dissipation rate, ω. This gives good results for boundary layer flows, flows with pressure gradients, and even separation [75].

The propeller was tested experimentally in an environment where the level of inlet turbulence was not precisely controlled and other sources of unsteadiness were also possible, such as recirculation, in the acoustic chamber. Due to this, it was uncertain if the propeller would have turbulent flow or laminar flow over the blades. Testing both, simulations with a turbulence model gave results closest to those produced in the experiment. This is noted in Figure 4.1. The turbulence model used in this study is Menter's Shear Stress Transport (SST) turbulence model [76] which uses the $k-\omega$ *model* near the wall and blends it to the $k-\varepsilon$ *model* in the free-field. Thus, taking the strengths of both methods and only relying on a blending function between the two.

The goal of employing uRANS simulations in this study is to predict the aerodynamic sources of noise for the CRP and S-CRP configurations. This method is considered low-order because, due to its modeling of turbulence, the solution will take less time to solve than high-fidelity solvers such as LES, DES, and DNS while still capturing the flow physics. However, because uRANS lacks the fidelity in the far field to capture the small pressure fluctuations that constitute sound, an acoustic methodology must be utilized to calculate far-field noise based on surface pressure fluctuations.

The commercial program used in the thesis project, Simcenter STAR-CCM+ [77], includes a methodology to export surface pressure data as CFD General Notation System (CGNS) files and import it into the acoustic solver, Simcenter 3D[78]. Additionally, because of the use of turbulence modeling, the small fluctuations associated with turbulence are stochastically determined. This means that periodic influences on the flow are not captured at this level and limits the usability of higher harmonic results in cases with low periodic influences.

3.2.2. Application of uRANS

The definition of the CFD mesh will begin with the requirements of the wall. The wall model used in this study, the *All y$^+$ Treatment*, requires the value of the y$^+$ at the wall be either less than 1 or between 30 and 50 [77]. The $y+$ value is a dimensionless parameter that represents the distance from the first mesh cell to the surface wall shown in Equation 3.1 where u_τ is the friction velocity, y is the absolute distance from the wall of the first mesh cell, and ν is the kinematic viscosity. In this case, all surfaces have a $y+<1$ such that only the viscous sublayer needs to be modeled stochastically and the buffer layer before the log-law region will be directly calculated.

$$y^+ = \frac{yu_\tau}{\nu} \tag{3.1}$$

Because the friction velocity, u_τ, will vary across different regions of the surfaces, the propeller and shroud geometries are split into patches in the CAD model. This allows for more refinement on the surface of the propeller near the tips, leading edge, and trailing edge where the velocity is higher.

Immediately surrounding each propeller is a specified region to dictate the rotation of the propellers. In the geometries containing shrouds, this region extends radially to the midpoint of the tip and shroud wall, shown in blue in Figure 3.4. In cases without a shroud, this region extends to 1.25 times the radius of the propeller. The distance from the tips ensures mesh growth from the propeller surface does not cross the boundary of this region so when it is used as a sliding mesh there is no refinement discontinuity outside at the interface.

Within the domain, there are two regions large regions of refinement. One around the propellers and shroud and one around the motor body. Because the characteristics of the flow downstream of the shroud and propellers are not of interest, the region around the motor body is only refined enough to properly propagate the flow away from the interested region and does not solve for fine details of the flow. This maintains a lower overall cell count.

The STAR-CCM+ user manual suggests, for simulations of this nature, to use a 'bullet shaped' domain (Figure 3.5) with a length of 20 characteristic lengths downstream and a radius of 10 characteristic lengths beside and ahead of the configuration [77]. In this study, the characteristic length is taken to

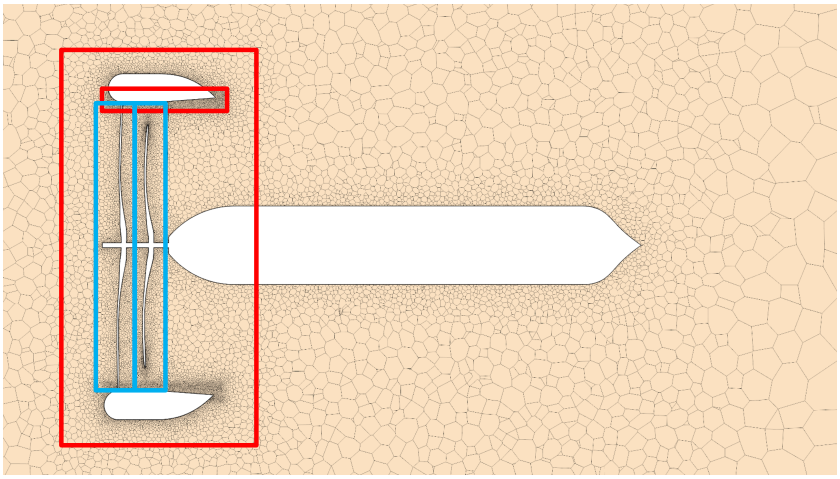

Figure 3.4: Depiction of low cell count mesh. Red indicates regions of refinement (not all shown) and blue indicates sliding mesh regions.

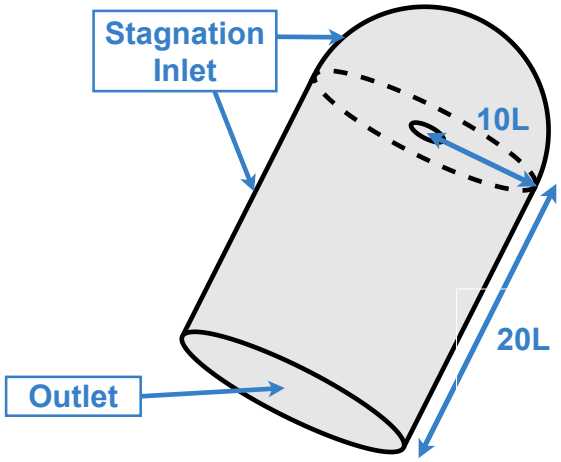

Figure 3.5: Domain size definition where the characteristic length, $L = 1.25D$

be 1.25 times the diameter of the propellers. This definition is used to negate the effect of boundary on the near-field aerodynamics while using as few cells as possible.

As denoted in Figure 3.5 the boundaries in front and around the propeller are defined as a *stagnation inlet* condition with a boundary-normal definition of flow direction. This condition is chosen such that the total pressure can be defined as zero at boundaries, which is far enough from the near-field aerodynamics of the propeller systems that there should be no flow or pressure change.

Ref. [77] indicated that the stagnation inlet should be used in combination with a *pressure outlet* boundary to ensure the static pressure can match that of the inlet environment. This maintains the far-field condition and allows the dynamic pressure created by the rotating surfaces to exit the domain. The combination of these two accounts for mass flow conservation.

All uRANS simulations were initialized with a steady simulation where the region immediately surrounding each propeller is defined in a moving reference frame (MRF). The previously defined region of 1.25 times the radius of the propeller is used for this. The application of a steady MRF simulation serves the purpose of initiating the field and expediting the convergence rate.

In the context of the unsteady scenario, this region becomes a sliding mesh, meaning that the region rotates during each time step. An essential consideration when determining the time step is to prevent the mesh from rotating excessively far from its original position, which could result in a large discontinuity at the interface. In practical terms, this translates to a limitation wherein the region's rotation is restricted to a distance of 1-2 cell lengths at the outermost radius.

The criteria for a simulation being considered converged when the thrust values of all components are within 0.25% at the same spatial point between two revolutions. This typically occurs around the third or fourth revolution thanks to the RANS initialization. This consistency is then validated for an additional revolution before exporting the data, which spans over four revolutions.

Finally, the complete list of models and solver parameters is listed in Table 3.1. This list includes an acoustic solver which is incorporated in STAR-CCM+. This is described alongside the other computational aeroacoustics (CAA) models in Section 3.3.2.

Additionally, transition models were tested for applicability in this simulation study. The two models incorporated into STAR-CCM+ are the *Gamma-ReTheta* model [79] and the simplified version, the *Gamma* model [80]. This endeavor is not included here as the results were inconsistent and had a larger disagreement with the experimental data. However, future work with these methods is important for the future of contra-rotating geometry.

Category	Model/Value
Solver Equations	Reynolds-Averaged Navier Stokes
Space	Three Dimensional
Time	Implicit Unsteady
Flow	Coupled Energy/Flow
Equation of State	Ideal Gas
Viscous Regime	Turbulent
Turbulence Model	SST (Menter) K-Omega
Wall Model	All y+ Wall Treatment
Acoustics	On-the-Fly FW-H
Time Step	2.7778E-5 s (1°)
Temporal Discretization	2nd-Order
Maximum Inner Iterations	10
Minimum Allowable Wall Distance	1E-10
Expert Initialization Method	Grid Sequencing

Table 3.1: List of models, boundaries, and solution conditions for all simulations.

3.3. Computational Aeroacoustics Solver

This section details the approach of the Computational Aeroacoustics (CAA) Solver, emphasizing its novel approach to handling noise prediction challenges in aerodynamic systems through the *Source-Mode Method*. Detailed explanations cover the solver's methodology, its integration with Finite Element Method (FEM) for improved acoustic pressure calculations, and separating aerodynamic and acoustic installation effects.

3.3.1. Source-Mode Method

Employing a mesh fine enough to accurately capture the minuscule pressure fluctuations across the entire domain, extending up to the listener locations, is too costly when using approaches like unsteady uRANS. Conventional CFD second-order schemes necessitate approximately 18-25 nodes per wavelength to refine the propagation of acoustic pressure effectively [57].

The acoustic analogies of the surface of the propellers are constructed from the pressure fluctuations calculated by the CFD simulations. The dipole source strengths are obtained by integrating the transient pressure field over acoustically compact segments of the propeller. The three components of the force per segment are calculated and in the frequency domain reconstructed from the rotating source to stationary components.

The propagation of the noise from the analogous source to the listen location would be solved using a Fourier transform for a complex Green's function for every point in the discretized space as the propellers rotate [81]. This proves to be computationally intensive.

A more suitable solution is to associate each spinning radiation mode inside the integration of Equation 2.10 with a *source mode*, which is induced by a continuous circular array of phase-shifted stationary point dipoles over the rotor plane (as seen in Ref. [82]). Thus, fixed dipole sources are calculated in an analogous reconstruction of rotating dipolar sources allowing a frequency domain solution.

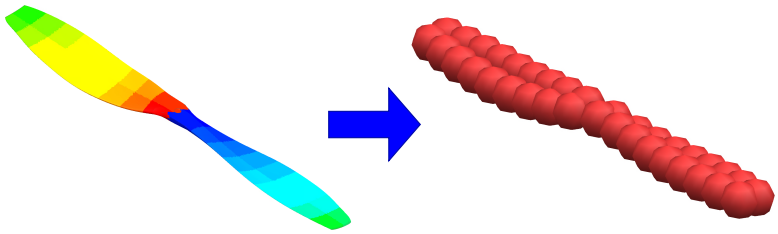

Figure 3.6: Visualization of compact segments and their equivalent dipole location (not scaled by Fourier coefficients)

Because the dipoles are at discrete locations some error is introduced into the solution, however, with this method, the sound field propagated in space is uniformly valid. As a result, each point on the field may be solved independently using a linear superposition, and equivalent sources for bodies in the field can be constructed.

This method is sufficient on its own to detail the free propagation of the rotating sources, however, it does not allow an investigation into the impact bodies in the flow (such as a shroud) have on the propagation. A Finite Element Method (FEM) solver can be introduced to resolve the geometric features of the model to calculate the source strength of reflections and to discretize the field to calculate the propagation rate. The FEM solves the propagation of the acoustic pressure, p, given the acoustic source pressure vector projected from the source modes, P_f, using the following differential equation:

$$[M_f]\{\ddot{p}\} + [B_f]\{\dot{p}\} + [K_f]\{p\} + [A_f]\{\ddot{p}\} = \{P_f\} \tag{3.2}$$

where $[M_f]$ is a compressiblilty matrix, $[B_f]$ is the impedence matrix, $[K_f]$ is the mobility (inverse mass) matrix, and $[A_f]$ is the area matrix.

The shroud surfaces serve as reflective boundaries entirely encompassed within the FEM domain. When exclusively considering the installation effects of the shroud, which involves assessing its influence on the propagation of sound waves rather than the pressure fluctuations on its own surface, the FEM approach quantifies the impact of the shroud's presence on the acoustic pressure.

In other cases, the noise stemming from the flow over the shroud is simulated with conventional surface dipoles. These dipoles are categorized as compressible, indicating that they incorporate the acoustic pressure fluctuations originating from other sources. This implies that the CFD simulation, from which the data is extracted, comes from a compressible solution and is refined enough to facilitate the propagation of acoustic pressure between the surfaces. While this approach elevates the refinement prerequisites of the CFD simulations, the areas with high levels of refinement remain localized.

The exterior boundary condition of the FEM domain's surface is a non-reflective surface, incorporating an Automatically Matched Layer (AML) in conjunction with a Kirchhoff radiation surface [83]. This setup facilitates the extension of the acoustic solution toward listener positions outside the computational domain.

The volume between these two boundary conditions is meshed using tetrahedral elements, selected with the consideration that they generally follow the rule-of-thumb of approximately 6 elements per wavelength corresponding to the frequency of interest [51]. Nonetheless, the employment of an Adaptive Order FEM solver within the software mitigates the strictness of this criterion by allowing mesh refinement tailored to each frequency analysis [78].

3.3.2. Application of CAA

At each time step during the exported rotations of the CFD simulation, a data file in the CGNS format is created. These files describe the pressure over the surfaces in the simulation and are then used as inputs for the acoustic solver. For each of the six simulations, one set of CGNS files was exported for all surfaces but, in the CAA program, the surfaces can be separated as necessary.

The tonal noise emissions for this study are calculated using a commercial CAA program, Simcenter 3D with the NASTRAN FEM solver and source-mode method built in [78]. Two meshes were built with the outer surface of both formed by projecting the surface of the shroud outward 12.5 cm. The first mesh was filled in completely with an irregular tetrahedral mesh. For the second mesh, the shroud was

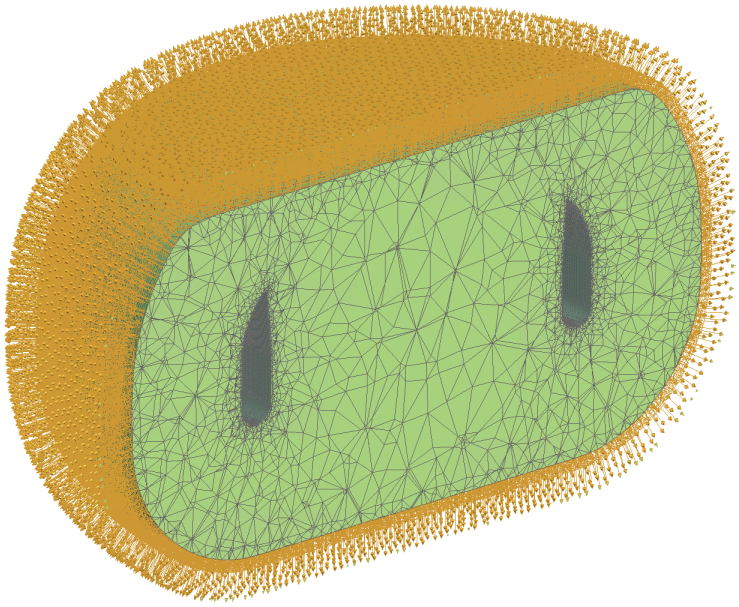

Figure 3.7: Cut away of the acoustic mesh showing the hollow region of the shroud surface and AML layer vectors

discretized linear triangular elements of 3 mm in order to describe the geometry. The second mesh was then also filled with tetrahedral shapes between the two surfaces as seen in the cut-away Figure 3.7.

The first mesh is not specifically necessary given that a method such as the Farassat 1A solution would likely be faster for free propagation. The mesh was used for solving free-field propagation to maintain the same methodology for all results.

Listener Locations

For the analysis using the experimental data Figure 3.8 describes the arrangement of the microphones as reported in ref. [71]. The ring in the left figure is orthogonal to the two on the right and Mic 0 and Mic 2 align with the axis where the centerline of the propeller will overlap (axis of overlap). The microphones are also in the rotor plane of the rear propeller.

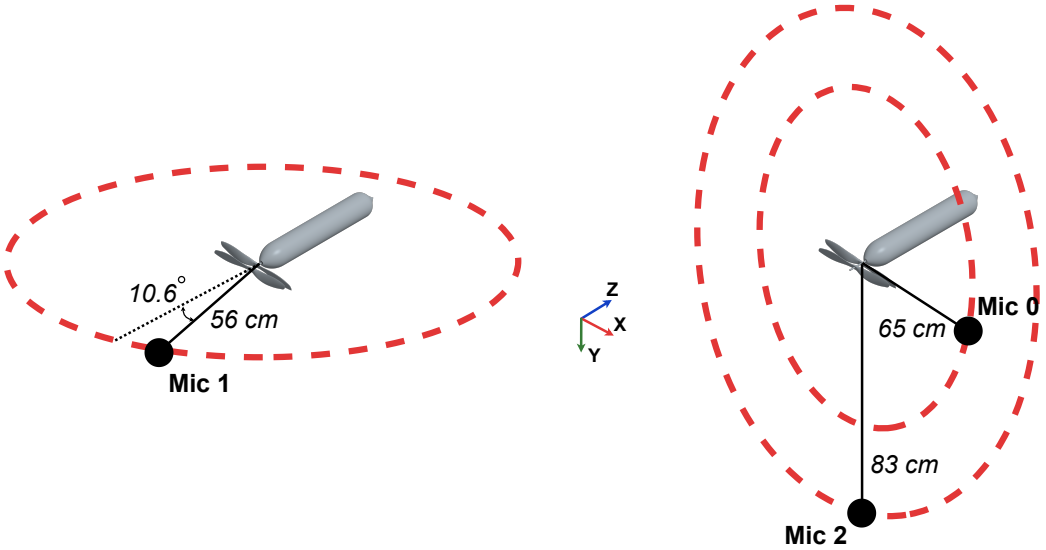

Figure 3.8: Microphone location diagram (not to scale).

Figure 3.9 describes the angles used to describe the results produced in the numerical simulations. The assumption that they are not to scale and orthogonal still holds. However, the rotor plane directivities are now in mean difference between the two propeller's rotor plane.

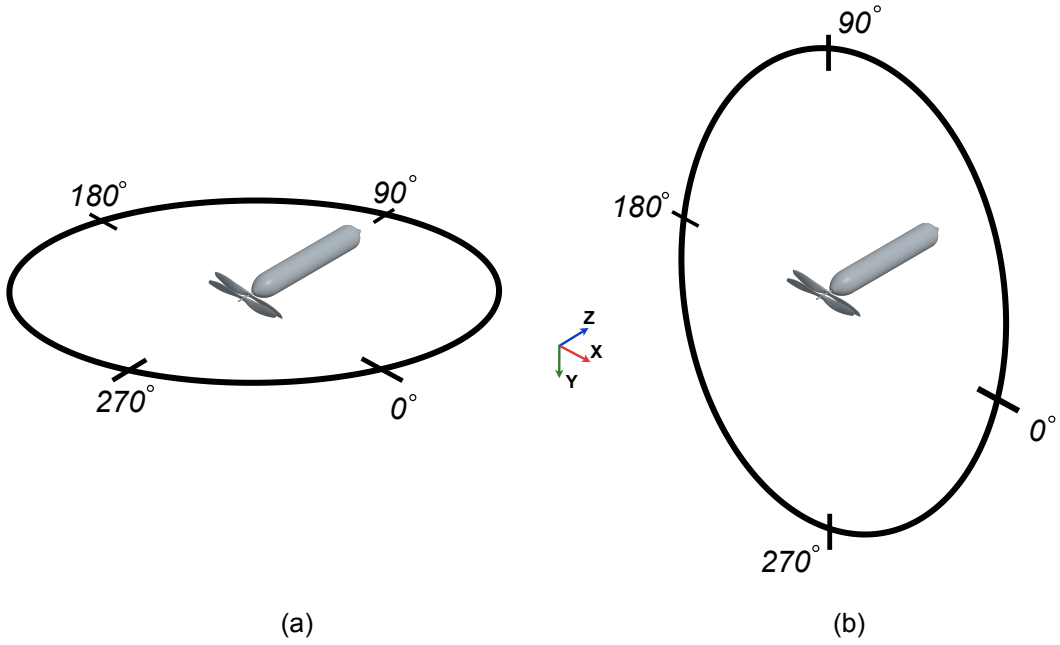

Figure 3.9: Sampling listener location definition for directivities in (a) the mid-plane and (b) the rotor plane (not to scale).

Addition Considerations

While the numerical simulation is designed to replicate the experimental conditions found in Ref. [71], some differences have to be pointed out. The numerical simulation represents an idealized scenario, primarily subject to expected errors related to numerical diffusion within the unstructured mesh and numerical truncation.

Nevertheless, it is worth noting that certain macro-elements may introduce additional variability. For instance, ambient conditions such as pressure and temperature were standardized to typical sea-level conditions in the numerical simulations due to the unavailability of experimental data at an earlier stage.

4

Verification and Validation

Before delving into the analysis of differences in the aerodynamic and acoustic performance of various configurations, it is essential to verify and validate the methodology. Therefore, this section will compare the uRANS-FEM method with experimental data as well as other CAA methodologies.

In parallel with this research, an experimental campaign was conducted at VKI, utilizing identical geometry and conditions. As the study is still ongoing, in this section, only the results published in Ref. [71] are utilized as a basis for comparison.

4.1. Aerodynamic Results

The first part of the uRANS-FEM methodology is the aerodynamic simulation of the flow condition due to the multiple geometries. To ensure that any changes analyzed between multiple configurations are truly due to the geometry the methodology must produce consistent and converged results.

Starting with an analysis of the effect of the mesh on the macro-performance characteristics, Figure 4.1 shows that for the CRP configuration all simulations using the conditions from Table 3.1 (in blue) are within 5% of the experimental results. With a higher refinement, the resulting total thrust value appears to approach the experiment.

Additionally, a Richardson extrapolation is included. This is solved using the simplified formula for a three-mesh study given by Equation 4.1. This method solves for the extrapolated exact value of any simulation variable, φ_{exact}, given the same variable in three different simulations. These simulations must have a mesh whose density increases at the same ratio, h.

$$\varphi_{exact} = \varphi_{fine} = \frac{\varphi_{medium} - \varphi_{fine}}{h^{(O)} - 1} \tag{4.1}$$

where the order of convergence, (O), is given by:

$$(O) = \frac{\ln\left(\frac{\varphi_{coarse} - \varphi_{medium}}{\varphi_{medium} - \varphi_{fine}}\right)}{\ln(h)} \tag{4.2}$$

The Richardson extrapolation indicates that at an infinitesimally small cell size (infinite cell count) there is a small difference between the experimental and numerical results. This difference in results at the extrapolated value as well as the difference at individual mesh size cases are all within 5%. This percentage is used as a reference since the uncertainty of the experimental campaign has not yet been published.

The accuracy of 15.4 million cell mesh is within sufficient accuracy, at least at a high level, and the finest mesh has excessively long computational time and very heavy storage requirements, therefore, the former is chosen as the baseline mesh. The following comparisons of different meshes also used this as the finest mesh when solving Richardson extrapolated values.

Figure 4.1 also includes the results of two additional simulations. The first is decreased time step results. This point represents the results of a simulation that was performed using the exact same conditions listed in Table 3.1 except the time step is 10% of the baseline case (now 0.1° per step). This

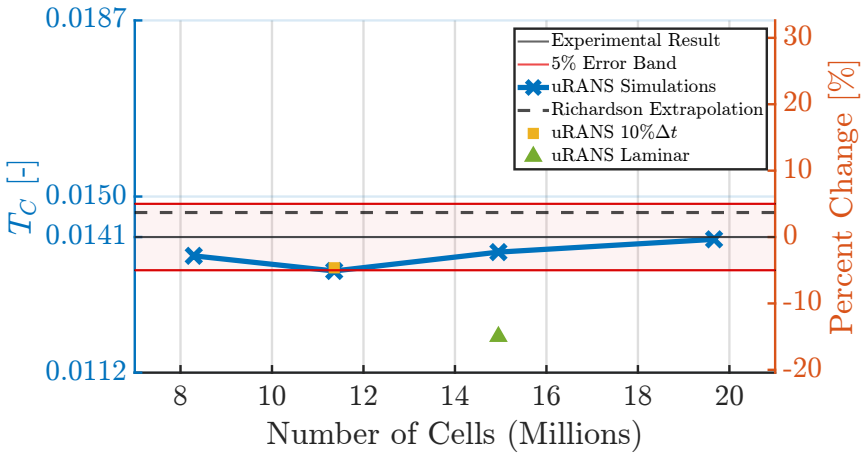

Figure 4.1: Total thrust value plotted against the mesh density of the entire domain for four simulations of the CRP (Richardson extrapolation is of the largest three mesh sizes).

was performed at a medium cell density mesh due to the large increase in data output. The result shows that the mean thrust solution of the system is negligibly different between the two time steps. This implies that, at least at a high level, the simulation setup is mostly converged in time.

The second additional point included in the plot is the laminar simulation. In this case, all conditions and solver models are the same as the baseline case except that the flow is laminar; thus, no turbulence model is applied. Given the low Reynolds number of the configuration, it may be expected that in a perfect environment, the flow over the propellers may be laminar. However, the results show that this is not the case. In fact, the thrust generated under laminar conditions differs significantly from the experimental findings, whereas the fully turbulent solution aligns more closely with the experimental data.

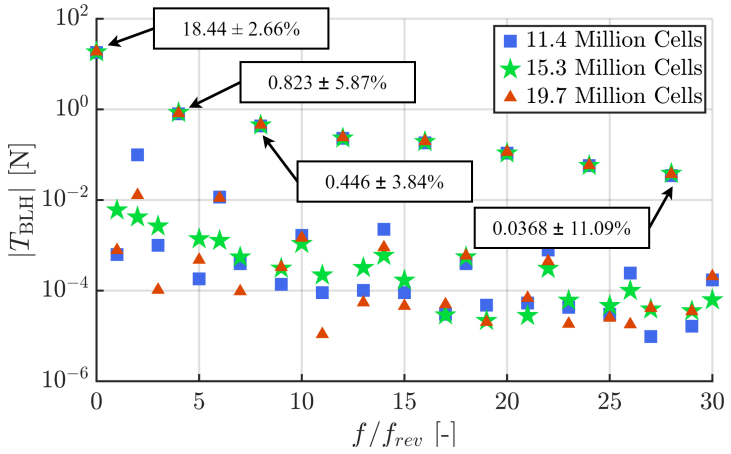

Figure 4.2: Blade loading harmonics of the rear propeller (both blades) from the open CRP configuration comparing the effects of changing the mesh size.

A more detailed examination of the thrust generated by the propellers provides valuable insights into the accuracy of the simulations. The Fourier transform of the time history of the total thrust from the lead propeller in the CRP configuration, as presented in Figure 4.2, offers a clearer understanding of how thrust is distributed across the system's harmonics.

This analysis reveals that the frequencies corresponding to interaction tones (multiples of four of the shaft frequency) dominate the unsteady loading on the blade. It is important to note that these interaction tones are consistently predicted between different mesh sizes, indicating that mesh refinement is capable of reliably capturing these interaction effects, especially at low frequencies. However, the mesh refinement does not consistently predict the other tones at the non-interaction frequencies. This inconsistency suggests that these harmonics may either be stochastically determined by the turbulence

model or heavily influenced by numerical errors within the simulations.

This observation highlights the critical role of interaction tones in shaping the unsteady loading on the blades and the methodology's ability to capture these interactions. It also implies that other harmonics could be less significant or be restricted in terms of computing and turbulence modeling power.

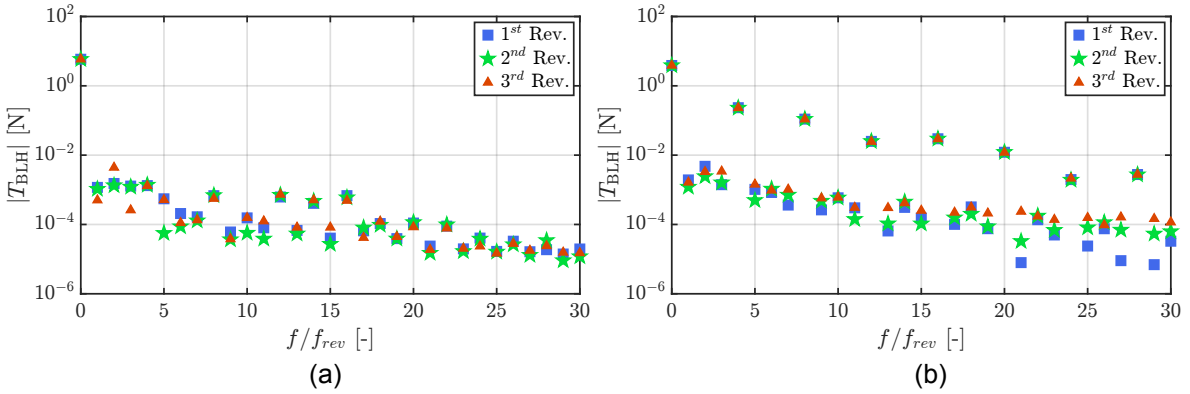

Figure 4.3: Blade loading harmonics at the baseline mesh size of a single blade of the rear propeller when it is (a) open and isolated and (b) in the CRP configuration.

Figure 4.3, which examines a single mesh size between revolutions, shows that consistency depends on the nature of the unsteady loading of the harmonics.

In Figure 4.3(a), where there is a lack of periodic influence on the isolated propeller, inconsistency between revolutions is evident. This is expected, as there are no anticipated sources of unsteady lift in the flow, apart from random fluctuations due to turbulence and numerical noise. In a single propeller configuration, the dominant sources of tonal noise are steady loading noise and thickness noise due to the propeller's rotation. The steady loading noise is evident in the plot, as at $f/f_{rev} = 0$, there is negligible variance between revolutions, indicating the consistency of the steady load.

The partial agreement observed in some of the higher harmonics is not due to a periodic noise but due to two functions of the numerical process. The strongest contributor the stochastic turbulence model introduces underlying fluctuations in similar patterns. As it is based on a periodic flow the model will introduce similar, yet still random, patterns with each revolution. Additionally, during the project, some research indicated that an imbalance in the mesh may exhibit quasi-periodic patterns, however, this is still ongoing as the effect is small.

In Figure 4.3(b), where unsteady loading occurs due to the presence of the other coaxial rotor, there is a significant increase in both tonal noise and agreement at the higher harmonics. The propeller blades pass each other at a frequency of four times f_{rev}, generating a consistent fluctuation of thrust and, consequently, a harmonic at these frequencies. This also increases the thrust at multiples of the BPF ($2f_{rev}$). This accounts for the increased agreement between each revolution. Moreover, it explains the less pronounced but still present agreement at other multiples of the shaft frequency. The influence from the other harmonics imparts a periodic nature to these frequencies, but this influence is at such a low level that random sources introduce inconsistency between revolutions.

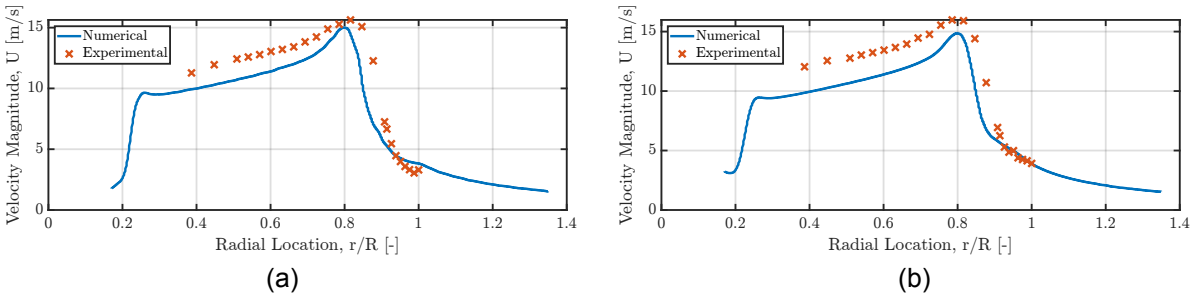

Figure 4.4: Wake velocity magnitude 10 cm ($z/D = 0.3$) downstream of the single open propeller in the (a) lead position and (b) rear position

Analysing the shape of the wake downstream of the propellers is an important part of this analysis as indicated by subsection 2.4.3. So, to confirm that the simulations give realistic results for the downstream velocity profile plane probes from the numerical simulations are compared to experimental hotwire analysis in Figure 4.4. Here it is shown that the trend and order of the velocity magnitude at the same location downstream is consistent between both methodologies.

It is not a perfect fit but this indicates that the outputs of the numerical simulation are relatively physical and not too far from the experimental case. Some of the small differences in the simulation conditions compared to an aerodynamic test in an anechoic chamber mentioned earlier can cause some of these differences.

4.2. Acoustic Results

In this section, the hybrid uRANS-FEM methodology, which is used to report results for the analysis in chapter 5, is analyzed for accuracy and limitations from the perspective of the acoustic results. An array of factors impact the accuracy of tonal noise predictions in propeller systems when compared with experimental data. These factors encompass mesh-related convergence, additional experimental spectral sources, the significance of thickness noise, and near-field versus far-field effects. Additionally, a comparative analysis of different acoustic methodologies is employed to identify uncertainties due to limited experimental data.

Mesh-related Convergence

The experimental study described in Ref. [71] encompassed measurements at three distinct microphone locations: two positioned on the rotational plane and one situated upstream of the propellers, as depicted in Figure 3.8. Importantly, while these microphones effectively capture all noise sources in the simulation, which will be discussed shortly, the numerical simulation exclusively captures the tonal peaks occurring at harmonics of the BPF.

To evaluate the precision of capturing these tonal peaks and to gauge the adequacy of describing the acoustic sources, a comparison is conducted in Figure 4.5 between different CFD mesh sizes similar to the one done for thrust. This comparison indicates the required mesh resolution to accurately represent the acoustic sources.

Microphone	1^{st} BPF [dB]	2^{nd} BPF [dB]	3^{rd} BPF [dB]	4^{th} BPF [dB]	5^{th} BPF [dB]
Mic0	2.111	**-6.622**	2.592	-5.290	6.121
Mic0 (Extrapolated)	2.044	0.339	2.520	0.988	**4.152**
Mic1	-5.385	3.820	**-8.641**	6.308	-2.723
Mic1 (Extrapolated)	-5.149	2.310	**-8.599**	5.488	-2.692
Mic2	3.326	**-4.951**	0.819	-2.586	2.778
Mic2 (Extrapolated)	3.274	**-4.831**	0.838	-2.702	2.308

Table 4.1: The maximum $|\Delta SPL|$ difference at the experimental microphone locations per frequency between the experimental data and the numerical simulation (at 15.3 million cells) and the Richardson extrapolation of the different mesh sizes for numerical simulation results in bold.

While Figure 4.5 extends only up to the 6th BPF harmonic, these initial BPFs offer indicative patterns that persist throughout the entire spectrum and are the loudest. This plot clearly demonstrates that as the mesh resolution increases, the agreement with the tonal peaks becomes more accurate. The computational constraints that impose limitations on achieving high mesh densities require the cell count to be kept as low as possible. Therefore, it is essential to explore whether further improvements are attainable with a higher cell count. In pursuit of this, a Richardson extrapolation is performed for each harmonic generated by the numerical simulations, and the results, along with the finest mesh size used for acoustic calculations, are presented in Table 4.1.

The similarity between the extrapolated difference and the baseline difference suggests that additional mesh refinement likely will not improve the uRANS-FEM methodology's capacity to capture potential outcomes. The observed disparities in tonal results across varying mesh sizes indicate a threshold for consistent predictions. Collectively, the results from the CFD simulation indicate that the pressure fluctuation patterns on the blade's surface are adequately captured. Minimal differences between the results of the larger cell count meshes suggest that the mesh has been refined adequately

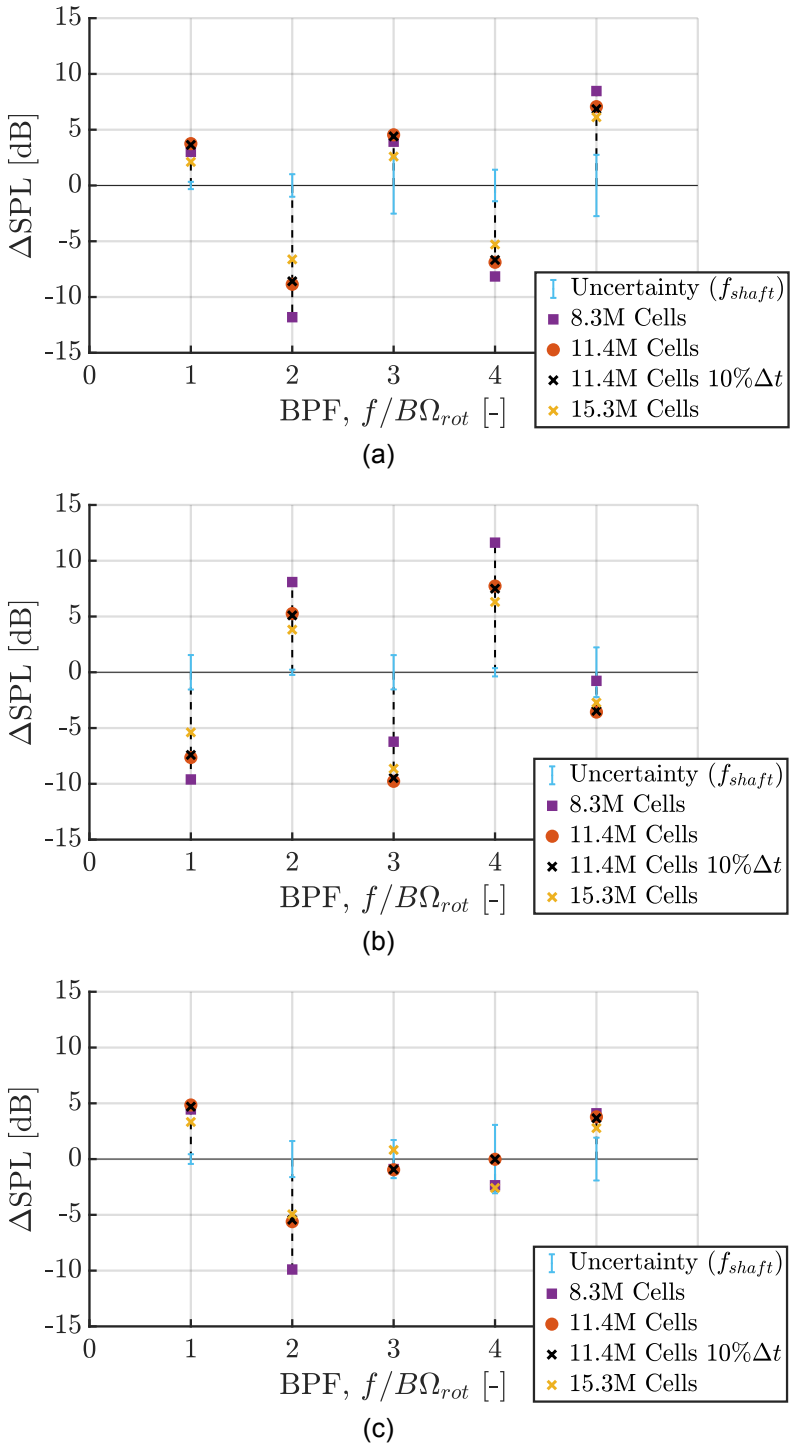

Figure 4.5: Difference between the experimental data and the different numerical simulations for the CRP configuration (including uncertainty due to the tone present at the shaft frequency) at (a) Mic 0, (b) Mic 1, and (c) Mic 2.

on the propeller blade's surface to fully capture the pressure fluctuations, and consequently, lift and drag associated with tonal noise. Thus, the 15.3 Million Cell mesh is considered sufficiently refined and serves as the baseline for the subsequent analysis, with any discrepancies between experimental and numerical results discussed below.

Contribution of Thickness Noise

The microphones employed in the experimental study capture all noise sources generated, which, when compared to the results from the numerical study, can help assess whether tonal noise is primarily dominated by loading noise, as assumed in this study. This can also explain why specific differences emerge between the experimental and numerical results.

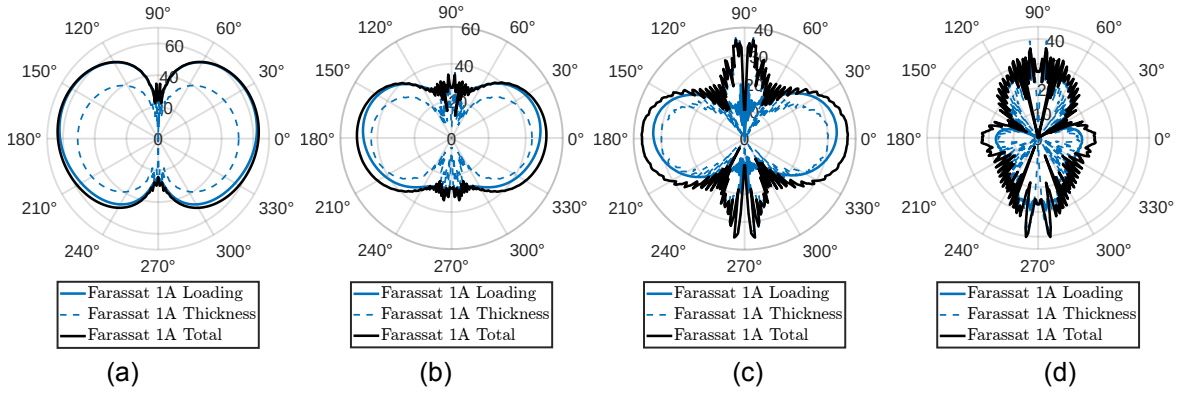

Figure 4.6: Sound level at the mid-plane at $20D$ of the free propagation a single open propeller using the uRANS-F1A methodology for the (a) 1^{st} BPF (200 Hz), (b) 2^{nd} BPF (400 Hz), (c) 3^{rd} BPF (600 Hz), and (d) 4^{th} BPF (800 Hz).

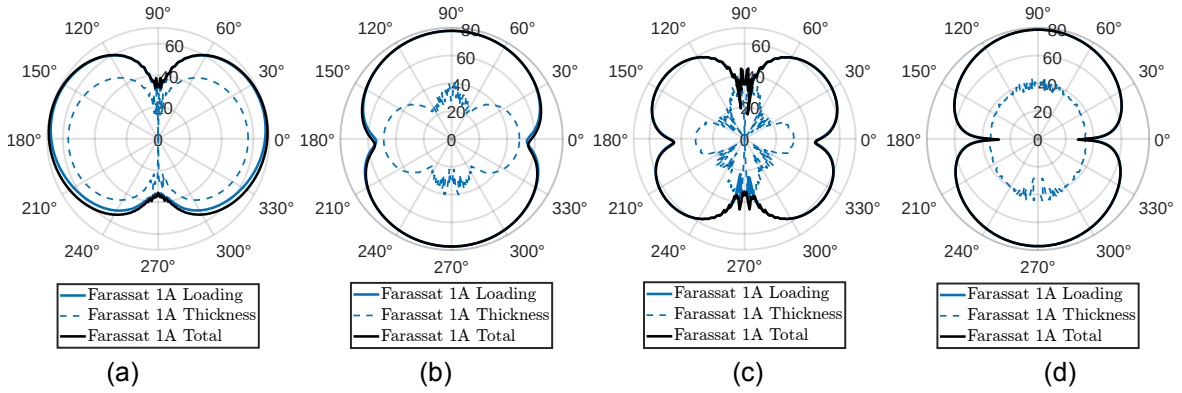

Figure 4.7: Sound level at the mid-plane at $20D$ of the free propagation of the lead propeller in an open contra-rotating configuration using the uRANS-F1A methodology for the (a) 1^{st} BPF (200 Hz), (b) 2^{nd} BPF (400 Hz), (c) 3^{rd} BPF (600 Hz), and (d) 4^{th} BPF (800 Hz).

The first possible cause for the differences is the thickness noise. As depicted in Figure 4.6 and 4.7, the thickness noise contributes to the overall noise at the peak frequencies. Thickness noise is inherently associated with the first BPF because both blades on a propeller displace the air at the rate of rotation. Consequently, the shape of the thickness noise remains identical for both the single propeller and the contra-rotating propellers.

However, a crucial distinction arises in the level of unsteady loading. In the case of the single propeller, unsteady loading is minimal, and thus, the predominant source of loading noise stems from the modulation of steady loading into higher harmonics at the listener's position. This modulation effect is the same phenomenon responsible for generating thickness noise. Consequently, at higher harmonics thickness noise begins to play a more pronounced role in the overall noise spectrum.

This is also why the average change in noise level is relatively small at higher frequencies for the contra-rotating setup as the thickness noise is only harmonics of the original tone but the CRP introduces unsteady loading inducing more noise at higher harmonics. At the first BPF, the change at each directivity between the total noise and the loading noise remains quite low on average.

While the maximum change attributed to thickness noise does exhibit relatively large values (Table 4.2), its significance should be considered in context. The angles at which the maximum change occurs are aligned with the axis, where noise levels are very low, making it challenging to precisely capture the true value. The reasons for the low noise levels along these axes are further explored in

subsection 5.3.1 but because the microphone locations tend to be on or near these axes account for some of the discrepancies noticed in Figure 4.5.

BPF	Average	Maximum	Angle of Maximum
1^{st}	1.56 dB	6.00 dB	88°
2^{nd}	0.44 dB	2.76 dB	1°
3^{rd}	0.86 dB	23.66 dB	83°
4^{th}	0.18 dB	8.80 dB	181°
5^{th}	0.65 dB	23.12 dB	274°

Table 4.2: The maximum ΔSPL due to the inclusion of thickness noise in the CRP configuration.

The remainder of this study does not cover into thickness noise, primarily because it falls outside the scope of the uRANS-FEM methodology's capabilities. Thickness noise becomes relatively insignificant at higher harmonics when unsteady loading due to propeller interactions comes into play. However, it remains a significant factor at the Blade Passage Frequency (BPF) and for single rotors.

In this context, it is important to clarify that thickness noise is primarily determined by factors such as velocity, freestream conditions, and the rotor's thickness, as derived in Equation 2.10. In the current study, the largest change is in blade loading, which supports our decision to exclude thickness noise from the analysis. It is worth noting, however, that while thickness noise is not directly affected by variations in lift from propeller interactions, the introduction of additional propellers alters the velocity, impacting the magnitude of thickness noise.

The remainder of this study does not cover thickness noise as it is a limitation of uRANS-FEM methodology. The thickness noise is negligible at higher harmonics when unsteady loading due to propeller interactions is introduced but not necessarily so at the BPF and for single rotors. It is, however, shown here to not be affected by the propeller interactions and should only be a function of the velocity, freestream quantities, and thickness of the rotor. These parameters are not modified in the current study, which is the reason thickness noise is omitted from the analysis.

Additional Sources of Experimental Spectra

The experimental data exhibits additional peaks at multiples of the shaft frequency (in this case, at half the BPF frequency, as $B = 2$). These additional peaks are absent in the numerical simulations, where results remain below 20 dB at the same frequencies. The noise observed in the numerical simulation only arises from the influence of adjacent BLH tones and the modulating effect of the Bessel function.

In contrast, the prominent tones in the experimental results suggest a potential asymmetry in the experimental setup, such as blade imbalance, minor variations in propeller manufacturing, or rotor-induced vibrations. As these tones coincide with shaft frequencies, they also manifest at the BPF frequencies. In Figure 4.5, an uncertainty band is included to account for the potential influence of the shaft frequency, with the extremes representing perfect constructive and destructive interference. This is calculated using a simple logarithmic sum of the average of the tone on either side and the peak itself. This is meant to roughly and visually indicate how much these tones may be affecting the peaks but, it is not a rigorous calculation of uncertainty.

In addition to the thickness noise and possible influence of the shaft frequency tone, another impact on the difference may be the broadband noise. Obviously, the microphones will capture this but the uRANS-FEM methodology will not. The presence of broadband noise and background noise in the experiment may slightly change the levels of the peak. This is expect to be a very minor contribution as the broaddband noise picked up by the microphone in Figure 4.5 appears to only be between 30 and 40 dB.

Near-field vs. Far-field Effects

The last possible explanation that is investigated in this chapter for the difference between the experimental and numerical results is the methodology itself. The most substantial differences occur at the 2^{nd} and 4^{th} BPFs for the microphones on the rotor plane (Mic 0 and Mic 2). Figure 4.8 provides insight into this observation. This plot illustrates the SPL levels as the listener location moves further from the source, corrected to a listener location of 1 meter. This correction eliminates the effects of radial spreading which is the only acoustic interaction effect present in the far field. When the SPL value stabilizes, the listener location can be considered in the far field.

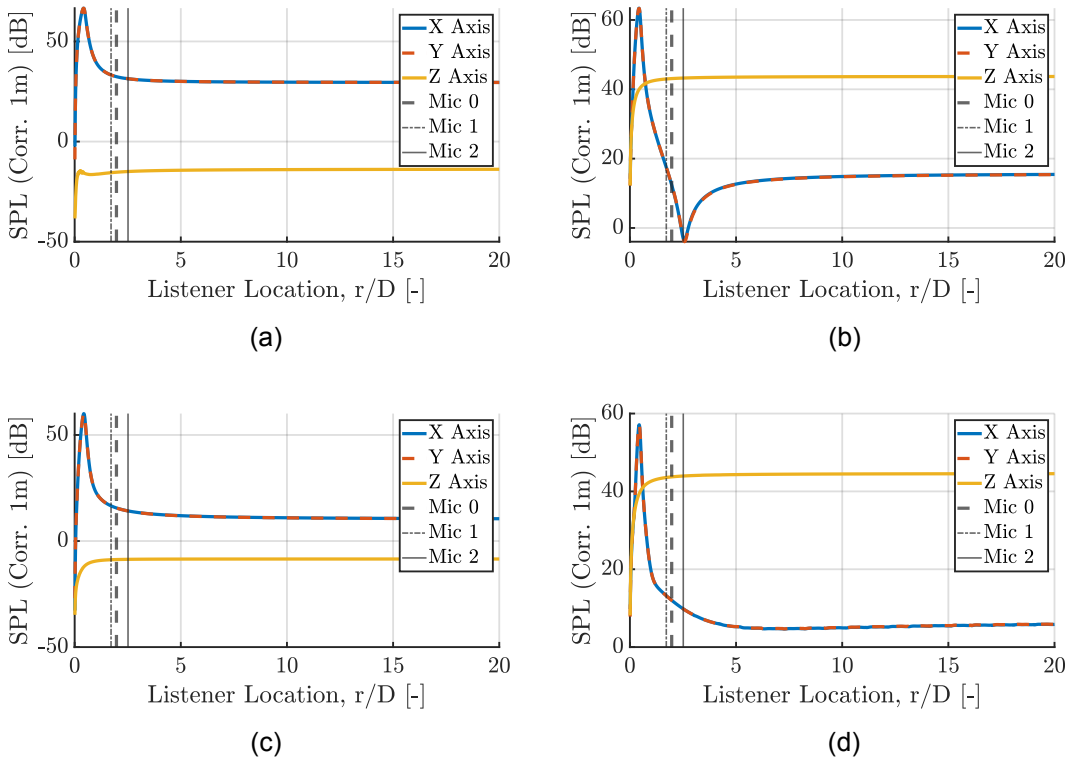

Figure 4.8: Sound level against radial distance corrected to 1 m to remove radial spreading effects for the CRP configuration at the (a) 1^{st} BPF (200 Hz), (b) 2^{nd} BPF (400 Hz), (c) 3^{rd} BPF (600 Hz), and (d) 4^{th} BPF (800 Hz).

In Figure 4.8, the results from three listener arrays extending along each of the axes radially from the sources are presented. Both the X and Y axes yield identical results. This similarity arises because both axes lie within the rotor plane, as depicted in Figure 3.8, and align with the axis of overlap of the rotor centerlines.

This plot offers insights into the near-field behavior of the propeller source, highlighting how, at specific directivities, near-field effects attenuate more rapidly. Additionally, it reveals the positions of the microphones do not necessarily reside in the far field, particularly at the 2^{nd} and 4^{th} BPFs. This observation suggests a degree of uncertainty in the methodology employed for calculating near-field results could lead to the disparity with the experimental results.

As a consequence, this study opts to exclusively conduct the analysis in the far field, with listener locations situated at a radius of 20 times the propeller diameter ($20D$). This choice seeks to mitigate potential uncertainties associated with near-field measurements.

Farassat vs. FEM Methodologies

To gain further insights into the disparities between the experimental and uRANS-FEM results, an additional acoustic approach is applied using the F1A method (subsection 2.1.3), resulting in the uRANS-F1A method. Both methodologies are then compared to the experimental results for both the open rotor and the CRP configuration, as depicted in Figure 4.9, focusing on the baseline mesh size. It's important to note that as there are no scattering bodies present in either simulation, this comparison purely evaluates the two methods: one operating in the time domain (F1A) and the other in the frequency domain (FEM).

In plots featuring co-axial propellers (Figure 4.9(b),(d), and (e)), the two methods yield an average difference between each other of 4.35 dB at all BPF peaks in the propeller plane (Mic 0 and Mic 2). Notably, the differences at the 2^{nd} and 4^{th} BPFs are $2-5$ dB higher than those at other tones, consistent with the trends observed in Figure 4.8. In front of the propeller, the two methods result in an average difference of 4.23 dB between all the peaks. This implies that there exists some divergence in the propagation method, introducing uncertainty that isn't attributed to the sources themselves. However,

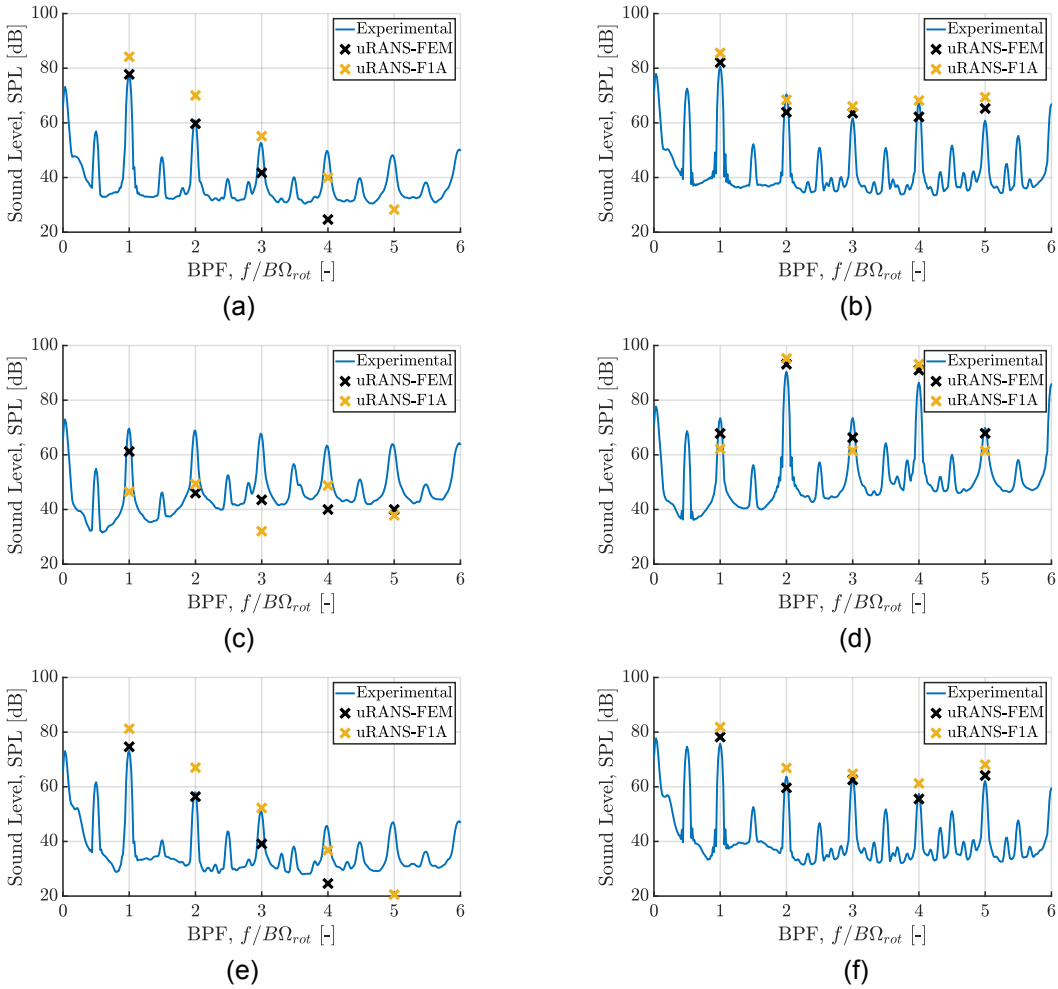

Figure 4.9: Comparison of the uRANS-FEM and uRANS-F1A methods with experimental results at Mic 0 for the (a) the open single propeller and (b) the open contra-rotating propeller; at Mic 1 for the (c) the open single propeller (d) the open contra-rotating propeller; and at Mic 2 for the (e) the open single propeller (f) the open contra-rotating propeller.

at almost every peak, the FEM method tends to provide predictions that are closer to the experimental results.

Additionally, Figure 4.9 includes a similar comparison for the open single propeller configuration. In this case, a large difference emerges between the two methods, with an average difference in tone prediction of 10.82 dB in the radial plane (Figure 4.9(a) and (e)) and 8.10 dB in front of the propeller (Figure 4.9(c)) between all the harmonics.

In the end, this was discovered to be due to the fact that the F1A application in STAR-CCM+ actually does not include a near-field term in its formulation [77]. This brings forth two conclusions. Firstly, the microphones are likely situated well within the near field given the more agreeable performance of the uRANS-FEM method. There is still a tonal noise source in the experimental values for the single propeller not captured by this method.

While the data at the microphone locations can be directly compared using the uRANS-FEM method to the experimental data, it is imperative that the methodology accurately predicts results throughout the rest of the field. Comparing the two acoustic propagation methodologies can give insight into how propagation is predicted in the far-field even if there is no experimental data at these locations due to size limitations in the anechoic chamber.

For higher frequencies, as depicted in Figure 4.10, the results indicate that both methods match exceptionally well for the free-field propagation of the propeller sources in the CRP configuration. Minor differences are observed near the axis, but the primary lobes closely align. However, at the first BPF, the agreement is less precise, particularly around 240° and 300°.

These differences between the two methods, apart from the first BPF, exhibit significantly less variation than at the microphone locations. They show deviations of less than 2 dB at most points, except on the axes. This finding, coupled with the conclusions drawn from Figure 4.8, suggests that the primary distinction between the methods lies in how they compute the near-field results.

In the near-field region, underdeveloped wavefronts may interact in complex ways. While these interactions decay with distance at a rate of $1/r^2$, as mentioned in subsection 2.1.3, it appears that the FEM-based methodology is better at predicting these changes. The ability to theoretically separate the effects of the near and far fields is substantiated by the matching directivities of the higher harmonics in Figure 4.10. The absence of an agreement for the first BPF suggests that it is still influenced by near-field effects, further implied by the fact that within a radius of $20D$, the first BPF (200Hz) only has 3.88 wavelengths to fully develop.

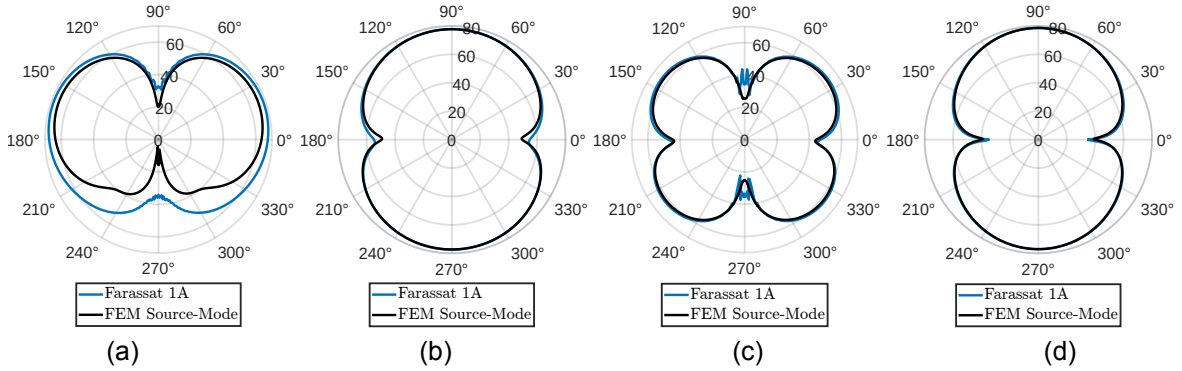

Figure 4.10: Mid-plane directive at $20D$ of the free propagation of both propeller sources for the CRP configuration using the uRANS-FEM and uRANS-F1A methodology for the (a) 1^{st} BPF (200 Hz), (b) 2^{nd} BPF (400 Hz), (c) 3^{rd} BPF (600 Hz), and (d) 4^{th} BPF (800 Hz).

4.3. Summary of Limitations

The uRANS-FEM methodology, as outlined in chapter 3, appears to provide a sufficient framework for evaluating both aerodynamic and acoustic trends, which are instrumental for the analysis conducted in this study. The underlying assumptions made, specifically that the aerodynamic flow is at standard sea-level conditions and is fully turbulent, are deemed acceptable. This acceptability is reinforced by the consistency of the results when compared to the experimental campaign.

The performance characteristics exhibit a high degree of agreement, and the wake profile generally represents the physical wake behavior. Using the aerodynamic results as sources for the acoustic simulation yields decent agreement, particularly in the context of tonal noise for multi-rotor systems. Considering that the numerical methodology exclusively captures tonal loading noise, the alignment observed at the peak frequencies in the CRP simulations is strong. This indicates a mix of effective methodology and a high influence of tonal loading noise. Similarly, the uRANS-FEM methodology offers a good prediction for the first two BPF harmonics in the case of the single rotor. However, progressing to higher harmonics, the dominance of loading noise diminishes, rendering the peak frequencies less representative of the experimental data and only reflective of the tonal component.

With the subsequent analyses, it's important to acknowledge certain limitations. Firstly, this study exclusively focuses on analyzing the tonal component of the loading noise, without addressing other sources such as thickness or broadband noise. While tonal loading noise is recognized as a critical source, this study refrains from making any comments on the total noise experienced in cases not verified against experimental data.

Additionally, the noise evaluations will continue to be conducted at a distance of 20 times the propeller diameter ($20D$) for consistency, despite the fact that results at the first BPF may exhibit higher uncertainty. Finally, the higher accuracy shown by the FEM-based method led to it being the main choice for the analysis in addition to its ability to capture acoustic installation effects.

5

Results and Analysis

The initial section focuses on the alteration of the propeller span from the single open propeller and CRP configurations required for the implementation in shrouded geometries. The analysis is centered around understanding the influence of these modifications on the thrust and efficiency.

The subsequent evaluation is conducted on the impact of geometry on aerodynamics across three primary configurations: the single open propeller, the contra-rotating propeller, and the shrouded contra-rotating propeller. This includes a section dedicated to how the addition of a coaxial propeller alters the performance and flow field, followed by a similar analysis conducted for the introduction of the shroud. Both of these analyses provide insights into the individual contributions of each component within the system.

The final section analyzes the sound level and directivities of the noise emissions for all three configurations. This section analyzes each propeller due to the effects of adding the additional propeller and then the shroud. The aerodynamic and acoustic interference effects of the shroud are separated. Lastly, these effects combine to produce the final results observed in the study.

5.1. Impacts of Propeller Modifications

The modification of the propeller, as detailed in Section 3.1 (see Figure 3.3), is required to make a uniform tip gap inside the shroud. This section analyzes the performance of the *shroud-modified propeller*, which is the version of the propellers inside the shroud and is referred to as the 'trimmed' propeller. This is compared to the original propeller design in the open CRP configuration, the 'untrimmed' counterpart.

Component	Untrimmed [N]	Trimmed [N]	Percent Change
Both Propellers	18.42	17.37	5.70%
Max Variation	2.61	2.61	0.00%
Lead Propeller	10.65	9.84	7.61%
Max Variation	2.09	2.12	1.44%
Rear Propeller	7.77	7.53	3.09%
Max Variation	1.29	1.34	3.88%

Table 5.1: Thrust for the open CRP configuration for both trimmed and untrimmed configurations.

The data presented in Table 5.1 reveals a reduction in overall thrust upon removing the tip section (trimming) of the propeller. However, the fluctuations in the thrust of the individual blades and the total configuration remain minimally altered. This initial observation implies that the interaction effects may not be dependent on the exact blade length or the specific shape of the tip.

Both propellers undergo a thrust reduction due to the reduction of the tip section, despite their unique thrust distributions. This is evident when examining the thrust as a function of the radius for both the lead and rear propellers in the open CRP configuration, as illustrated in Figure 5.1, which compares the trimmed and untrimmed versions. The unique thrust distribution for each propeller, contingent on its position, is a result of the interaction of the blades.

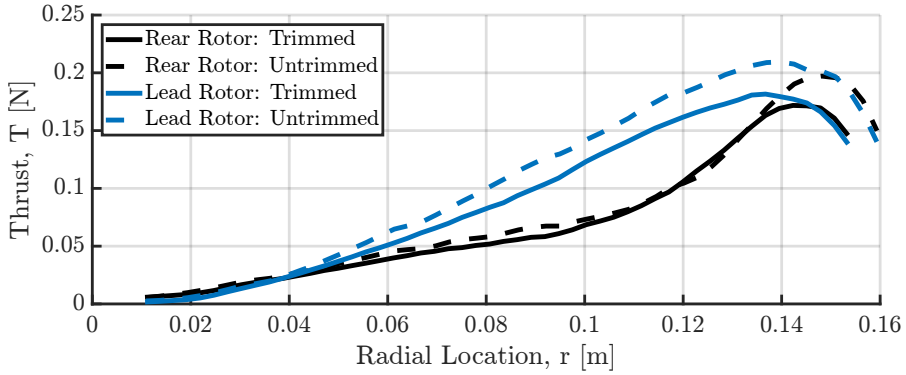

Figure 5.1: Sectional thrust distribution across both propellers in the CRP configuration for both propeller lengths and shapes.

The absence of the tip section detrimentally impacts the overall performance of the lead propeller, not only eliminating the last section which generates its own lift but also significantly diminishing the region of maximum thrust, an effect that permeates from the tip to the hub due to an overall reduction of flow acceleration from the propeller. This impact is evident upon examination of Figure 5.1, which indicates the reduction in propeller performance due to these modifications.

Conversely, the rear propeller experiences a subtler alteration, with the trimming effect predominantly impacting the final 10% of the propeller's performance. This is attributed to the wake generated by the lead propeller, which mitigates the loss propagated from the tip along the propeller span.

Therefore, the trimming of the propeller, while reducing overall thrust, exhibits an impact based on position and other interactions for the lead and rear propellers, with the rear being less affected due to the wake from the lead propeller. These insights necessitate that any comparative analysis between the trimmed and untrimmed propeller versions, thus, between shrouded and unshrouded geometries, should factor in these results to accurately interpret the observed changes.

5.2. Aerodynamic Performance Results

This section explores the alterations in the aerodynamics of the propeller system attributable to CRP and S-CRP configurations. Beginning with an overview that encompasses thrust, power, and efficiency across various configurations, the respective benefits and drawbacks of each are presented.

Subsequently, a focused breakdown of components is presented. Initially, alterations in aerodynamics as a consequence of introducing the coaxial contra-rotating propeller, are examined, followed by those due to the inclusion of the shroud. These elements not only explain the observed performance but also set a foundation for understanding the variations in acoustic emissions, which will be discussed in the following section.

5.2.1. Overview of Total Performance Metrics

Open and shrouded contra-rotating propellers exhibit certain advantages, such as increased thrust per area, but also present trade-offs in terms of efficiency. The substantial contribution of the shroud to total thrust and the impact of different configurations on individual propeller performance are critical considerations for design and the rest of this research.

Configuration	C_T	C_T/A [m^{-2}]	C_P	C_P/A [m^{-2}]	FOM
Open Single Rotor	0.0803	0.9377	0.0282	0.3293	0.571
Isolated Double Rotor	0.1606	0.9377	0.0564	0.3293	0.807
Open Contra-Rotating	0.1265	1.4772	0.0541	0.6318	0.588
Shrouded Contra-Rotating	0.1140	1.331	0.0476	0.5558	0.572

Table 5.2: Performance coefficients for the entire system of each configuration. Given $n_1 = n_2 = n$ and $\Omega_1 = \Omega_2 = \Omega$, all results of the same type are non-dimensionalized by the same values.

To understand this in-depth, the effectiveness of shrouded contra-rotating propellers is assessed through their impact on thrust performance, power consumption, and efficiency. Mean coefficients for

thrust, power, and the FOM (Equations 2.12, 2.13, and 2.17, respectively) have been calculated and are presented in Table 5.2. The non-dimensionalized results are presented using the diameter and rotation rate of a single propeller to ensure consistency across different propeller configurations.

Table 5.2 incorporates the performance metrics for the isolated double rotor. Although this is not a simulated geometry, it represents double the nominal thrust of the open single rotor, non-dimensionalized by the dimensions of a single rotor. The inclusion of this result illustrates the theoretical upper limit that a two-rotor system could achieve without any interaction effects.

From the data, coaxial propeller configurations show an increase in thrust and power consumption compared to a single rotor, as expected due to the incorporation of two rotors. There's also an increase in FOM, suggesting an enhancement in power utilization efficiency, potentially due to swirl recovery by the rear propeller.

Comparatively, the coaxial propeller displays lower overall thrust and power consumption than two isolated propellers but, has a reduced FOM. When considering thrust per unit area, it surpasses both the single propeller and double isolated propeller. This aligns with the anticipated benefits of the CRP system discussed in Chapter 1, which emphasizes achieving higher thrust in a restricted area.

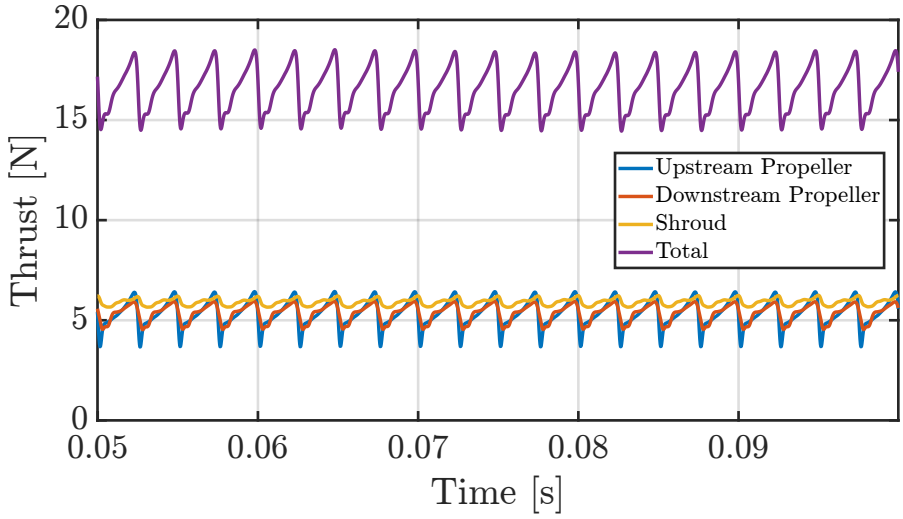

Figure 5.2: Components of the total thrust of the S-CRP configuration as a time history for four revolutions ($\Omega_1 = \Omega_2 = 100$Hz).

Conversely, the S-CRP demonstrates a decline in performance across all measures compared to an open CRP, reducing thrust, increasing power consumption, and lowering the FOM. Yet, it still yields more thrust than a single rotor and uses less power than two open rotors. It also has an improved thrust per area compared to two single rotors and an improved FOM compared to a single rotor.

Figure 5.2 reveals that even though the shroud might not be the optimal choice for pure performance in hover scenarios, it contributes approximately 35.66% to the total thrust. The lead and rear propellers contribute 32.11% and 32.23%, respectively. This significant contribution from the shroud, even in hover conditions, emphasizes its importance in performance evaluation.

While the performance of the S-CRP configuration does not entirely align with expectations set out in Section 2.4.1, the thrust production falls within the anticipated range. The subsequent sections aim to clarify the discrepancies between the shroud's performance and the predictions from the literature, while also providing recommendations for future experimental endeavors.

The observed periodicity in the thrust for each component in Figure 5.2, including the shroud, indicates unsteady loading and, therefore, the presence of unsteady-noise-generating mechanisms. Fluctuations over the shroud are relatively small, suggesting a diminished noise source strength in this region. All fluctuations maintain consistent phase alignment and occur at the same periodicity. The primary peaks that appear four times per revolution match a frequency of 400 Hz, which is in line with the 2^{nd} BPF, corresponding to the rate at which the blade centerlines pass, identifying this as the first interaction frequency, $\omega_{1,1} = \omega_{2,0}$.

The BLHs given in Figure 4.3(b) provide a deeper insight into the periodic sources present in the simulation. With only the interaction tone peaks being consistent, this indicates that the time history

peaks are purely a function of the blade overlap frequency and its harmonics. This might differ if the flow was less perfect, such as in experimental results.

Configuration	C_T	C_P	FOM
Open Single Rotor	0.0803	0.0282	0.571
Open Contra-Rotating (Lead Propeller)	0.0731	0.0280	0.499
Open Contra-Rotating (Rear Propeller)	0.0534	0.0261	0.334
Shrouded Contra-Rotating (Lead Propeller)	0.0366	0.0215	0.230
Shrouded Contra-Rotating (Rear Propeller)	0.0367	0.0227	0.220

Table 5.3: Performance coefficients of each propeller in each configuration. Given $n_1 = n_2 = n$ and $\Omega_1 = \Omega_2 = \Omega$, all results of the same type are non-dimensionalized by the same values.

As observed in Table 5.3, introducing a coaxial contra-rotating propeller leads to a decrease in mean thrust and power consumption for each blade, still resulting in efficiency reduction. Adding the shroud further diminishes the thrust generated by each blade.

In the CRP scenario, the performance of the rear propeller drops more than the lead's, while in the S-CRP setup, both propellers perform similarly. This data is important for design engineers evaluating motor choices for configurations like CRP and S-CRP, emphasizing the trade-offs in terms of thrust, power consumption, and efficiency among different propeller designs.

In conclusion, while contra-rotating propellers, both open and shrouded, offer the advantage of enhanced thrust per area, the shrouded case provides lower overall performance than the CRP configuration. Still, the shroud generated thrust as expected but, did not improve the efficiency of the propellers. These findings underscore the necessity for an understanding of each component's impact on the system's overall performance. The following sections will delve deeper into the individual contributions, first examining the effects of the coaxial propeller arrangement and subsequently exploring the influence of the shroud on the propellers and the surrounding airflow dynamics.

5.2.2. Implications of Contra-Rotating Configurations

The installation of a contra-rotating propeller to a single open rotor introduces intricate aerodynamic interactions between the coaxial rotors, impacting system performance and noise generation. These interactions are predominantly governed by potential field effects and manifest as consistent patterns in thrust variation across both propellers, suggesting a strong influence on the resultant unsteady noise in the axial direction. This confirms what was anticipated by the literature in Section 2.4.3, however, fully discerning the separate contributions of potential field and wake interactions remains challenging due to the complex nature of the flow field.

To explore these phenomena in detail, this subsection investigates the aerodynamic interaction effects attributable to the presence of two coaxial rotors, focusing on the difference between the potential and viscous interactions. The former involves the alteration of the surrounding flow field due to rotor blade motion, while the latter concerns the wake and tip vortices generated downstream of the propeller due to viscous forces. The rear propeller can only affect on lead propeller through a potential influence, whereas the lead propeller can impose both potential and viscous effects on the rear one.

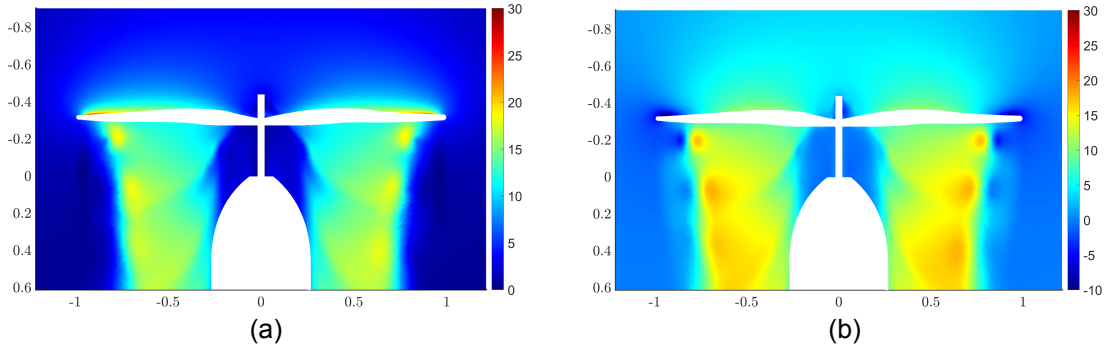

Figure 5.3: Instantaneous velocity (m/s) in the mid-plane of the open single propeller shown as (a) total magnitude and the (b) axial component.

For a single propeller, the impact of the shaft induces a separation of flow along the hub region. Additionally, this effect and the hub section of the blade not being designed to generate lift contribute to a large area of low velocity along the rotational axis. The flow behind the single propeller exhibits a noticeable contraction, with the streamtube boundaries intersecting at a location corresponding to the position of the rear propeller at a radius not exceeding $r/R = 0.75$. This contraction implies a narrowing of the flow streamlines. Both flow behaviors are identified in the flow velocity in Figure 5.3(a).

The open propeller also has a strong recirculating flow near the blade tips, complicating the definition of a distinct inlet area and introducing a region of reversed flow adjacent to the high-velocity patches just outside the boundary of the high-velocity streamtube. This is best identified in Figure 5.3(b) with the negative flow above the tips.

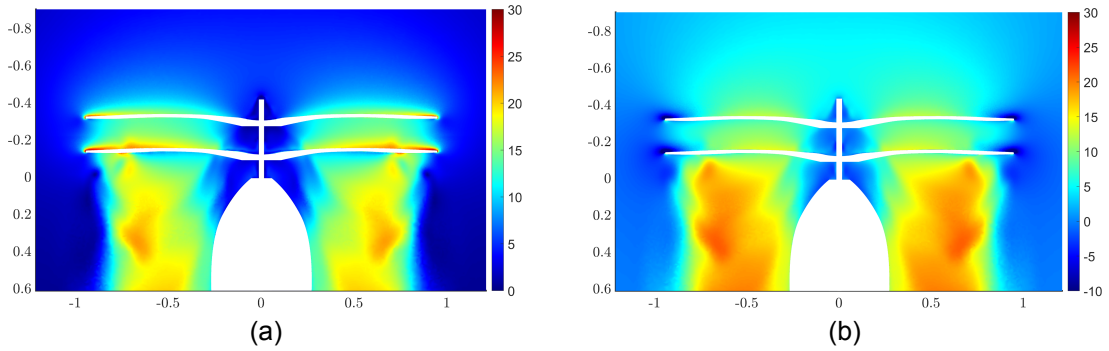

Figure 5.4: Instantaneous velocity (m/s) in the mid-plane of the open CRP shown as (a) total magnitude and the (b) axial component.

The contra-rotating propeller experiences this same tip effect. Figure 5.4 shows very similar shapes to the single propeller in terms of the streamtube shape and in the tip region. The differences do appear in the region between the two propellers, and with a higher velocity in the inlet and wake. This changes the velocity seen by both propellers.

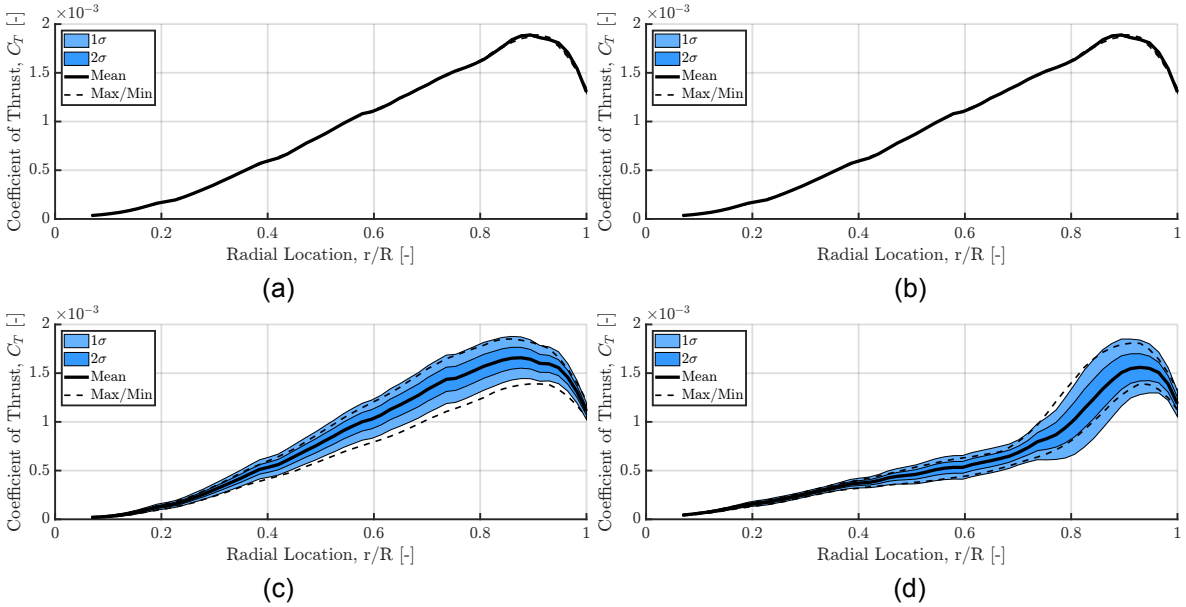

Figure 5.5: Radial thrust distribution along the (a) open single propeller in the lead position, (b) open single propeller in the rear position, (c) lead propeller from the CRP configuration, and (d) rear propeller from the CRP configuration.

The radial distribution of thrust provides the first insight into how this configuration affects the performance and noise emission of the propellers. In Figure 5.5, plots (a) and (b) are very similar since the only difference in the open rotor configuration would be the influence due to the proximity of the motor body.

However, the contrast between plots (a) and (c) reveals the change in the performance of the lead propeller caused by the presence of the rear. The mean of the thrust distribution experiences a slight decrease, particularly near the blade tip, amounting to a 9.16% reduction in the total mean thrust of the propeller. What is more remarkable is the amplified variation in thrust, which results solely from the potential influence of the rear propeller on the incoming flow. This variation remains roughly proportional to the total sectional thrust, between $20 - 25\%$, at any radial position. The only place this differs is near the tip where there are smaller fluctuations decreasing down to about 10% of the total sectional thrust.

This is not the case for the rear propeller comparing plots (b) and (c). Here, not only does the mean thrust decrease by an overall magnitude of 33.54%, but it also undergoes a large shift in distribution shape. The reduction in sectional thrust near the tip of the propeller is almost identical to that of the lead propeller. However, a significant difference emerges when examining radial positions less than approximately $r/R = 0.75$. This corresponds to the region where the wake of the lead propeller impacts the rear propeller, as evident in Figure 5.3(a). It does not impact along the full blade due to the contraction of the wake streamtube downstream of the rear propeller.

Further analysis indicates that the fluctuations in the region $0.75 < r/R < 1.0$ exist on the rear propeller blade and are of the same magnitude as observed in the same region of the lead propeller. Because this region is not influenced by the wake's impact on either propeller and exhibits similar fluctuation magnitudes, it provides the initial indication that the potential field has an important influence on the unsteady lift of both propellers. This observation aligns with the findings in the literature presented in Section 2.3.2, where the configuration's z/D value, approximately 0.091, falls well below the $z/D = 0.25$ threshold distinguishing between potential and viscous effects, as demonstrated in Figure 2.9 (Ref. [13]).

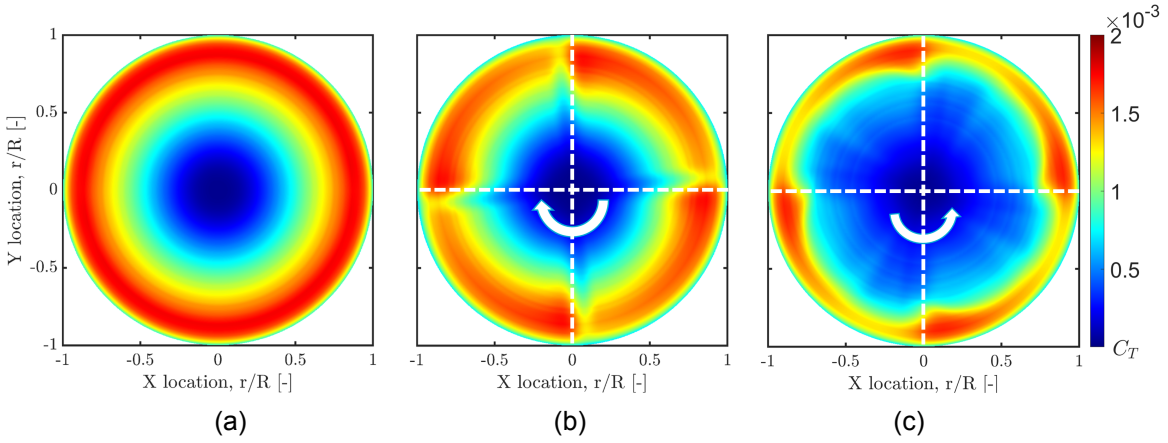

Figure 5.6: Radial distribution of the phase-locked average of the thrust over 3 rotations when looking from the upstream side of the (a) single open propeller, (b) lead propeller in the CRP configuration, and (c) the rear propeller in the CRP configuration (with arrows indicating propeller rotation direction and dashed lines indicating the axis of overlap).

The consistent patterns of thrust variation across both propellers, as shown in Figure 5.6, suggest the strong influence of potential field effects in aerodynamic interactions and the resultant unsteady noise in the axial direction. This conclusion is drawn from the observation that the most substantial increase in propeller thrust for both propellers occurs at the same point in the rotation, specifically in the region immediately following the centerline passage. Conversely, the most significant decrease in thrust happens just before this crossing.

The uniformity in the location and magnitude of these variations across both propellers indicates that they likely stem from a shared effect. This influence is presumed to be the potential effect, as it is the singular effect acting on both propellers. Furthermore, the convection speed of the wake would cause an asymmetry in the azimuthal location of the peaks. Finally, if viscous forces dominate, the peak changes would be where the wake is known to interact with the rear propeller ($r/R < 0.75$), not in the tip region as seen in Figure 5.6.

This analysis shows through an examination of flow behavior and thrust distribution the aerodynamic interactions at work between coaxial rotors and their effects on the performance metrics of the system. Understanding the fundamental interaction mechanisms is especially important for considering their implications in noise generation.

5.2.3. Insights on Shroud Installation Effects

The installation of a shroud fundamentally alters the aerodynamic behavior and performance of propellers. In this case, the shroud design did not perform as anticipated by the literature in Section 2.4.1. Marked by a flow separation along the inner wall of the shroud the tip regions are affected and streamtube contraction occurs. The effect on the propeller depends on its position within the shroud.

The shroud does prevent complete recirculation observed in open configurations but, the alteration of the blade's aerodynamics decreases the overall performance of the propellers. When a coaxial propeller is introduced in a shrouded propeller setup, there is a notable decrease in mean thrust for both propellers, accompanied by an increase in thrust fluctuations. These changes show that the shroud only changes the mean thrust value of the propeller but has a limited effect on the CRP interactions described in the previous section.

This section delves into the specific aerodynamic changes induced by the shroud, beginning with the distinct alteration in the inflow conditions that the propellers encounter in hover conditions. The propellers face different flow conditions near the shroud walls compared to open rotors, primarily due to the adverse pressure gradient along the shroud wall causing flow separation close to the leading edge.

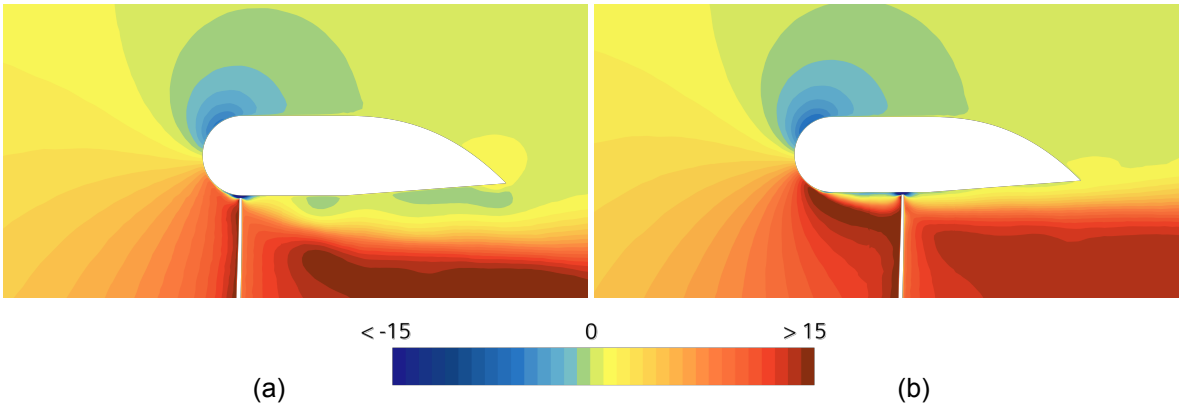

Figure 5.7: Instantaneous axial velocity (m/s) cut through the mean cord for a single shrouded propeller in the (a) lead and (b) rear position.

Figure 5.7 demonstrates the interaction of a single propeller with the shroud in different positions. It reveals a clear flow separation along the shroud wall due to the flow acceleration over the leading edge and has the same thickness regardless of the position of the propeller pulling in the flow. Thus, the amount of stagnant or recirculated flow seen by the propeller at its tip is dependent on its location within the separated flow. This same effect occurs when both rotors are present.

Because of the separation along the wall of the shroud, the streamtube continues contracting downstream, similar to what occurs in an open rotor configuration. The shroud does have the benefit of decreasing the recirculation at the propeller tips. There is still tip leakage around the tips, as shown in Figure 5.7 but this reversed flow is limited to the region of the tip gap and does not flow on top of the propeller, unlike the open propeller.

Regardless of both the propeller's axial and azimuthal position, the shape of the velocity contour remains relatively consistent for the outer surface. This suggests a low level of fluctuation in forces acting on the shroud itself, as further confirmed by the time history of thrust displayed in Figure 5.2. Additionally, the change in velocity over the outer shroud surface is less than 2.6 m/s between the midpoint and the trailing edge, indicating that the outer surface shape of the shroud has a minimal impact on thrust performance during hover conditions.

The lead propeller has a 21.37% overall reduction in thrust for both blades due to the presence of the shroud. This is due to a general reduction in thrust across the entire blade, with a pronounced decrease between $0.8 < r/R < 1.0$ as shown in Figure 5.8(a). However, due to the reduction of recirculation at the tip, the sectional thrust is slightly higher in the shrouded case at $r/R = 1.0$ and the region $0.92 < r/R < 1.0$ is more linear.

The rear propeller shows a decrease in thrust performance of 35.90%. The thrust distribution adopts a different shape in the presence of the shroud. Unlike the open configuration, there is no decrease

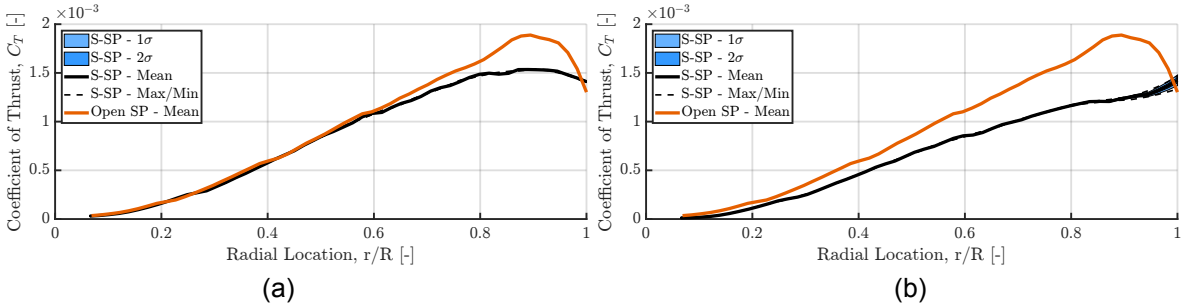

Figure 5.8: Radial thrust distribution along the span of the (a) shrouded single propeller in the lead position, (b) shrouded single propeller in the rear position.

in thrust at the tip due to the pressure differential across the tip being unable to fully circulate over the blade tip due to the presence of the shroud wall, eliminating the strong tip effects seen in the open configuration. Additionally, the stagnant or recirculating flow along the separated wall increases the thrust near the tip relative to the rest of the propeller due to the incoming velocity change at the propeller.

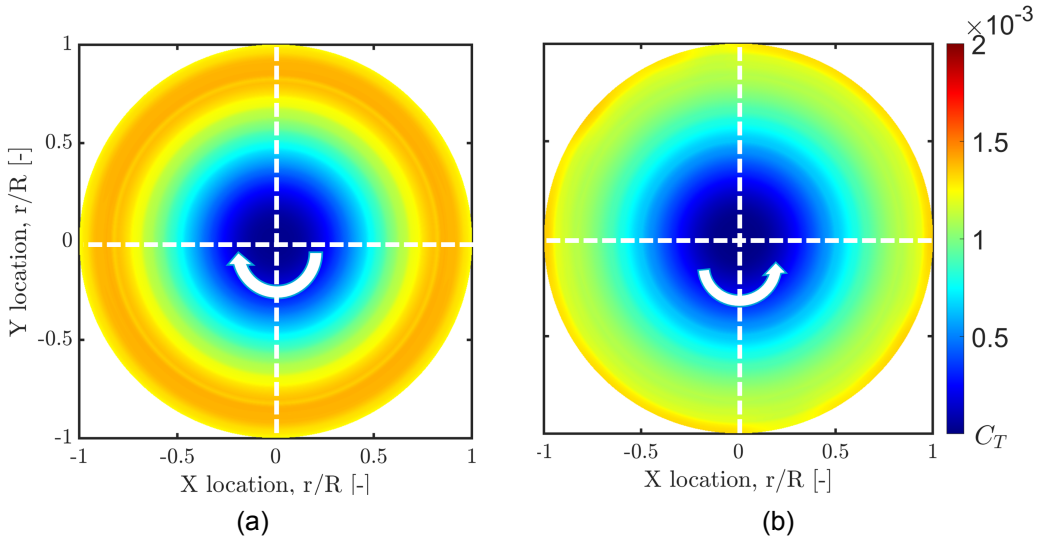

Figure 5.9: Radial distribution of the phase-locked average of the thrust over 3 rotations when looking from the upstream side of the (a) shrouded single lead propeller and (b) shrouded single rear propeller (with arrows indicating propeller rotation direction).

Generally, the average thrust across various azimuthal angles in the rotor plane remains stable for single shroud propellers, as shown in Figure 5.9. However, within the tip region of the shrouded single propeller in the rear position, there are noticeable fluctuations that don't align consistently with the BPF. These are visible in Figure 5.9(b) (as well as Figure 5.10(b)) near the tips, manifesting as subtle inconsistencies in color at the same radial position. Since the thrust represents a phase-locked average over multiple revolutions, these variations appear at a diminished intensity. This indicates that the fluctuations are not periodic in relation to the shaft frequency but does not rule out their potential presence at higher harmonics.

The addition of the coaxial propeller to complete the shrouded contra-rotating configuration leads to a further decrease in thrust for both propellers. Specifically, the mean thrust of the lead propeller drops by an additional 72.95% and the rear by 40.14%. This also creates an increase in thrust fluctuations across the blade span, as shown in Figure 5.10.

While the mean thrust reduces significantly due to the presence of the shroud, the magnitude of fluctuations in thrust for the lead propeller only slightly decreases compared to the open CRP configurations. Consequently, the fluctuations now range between 25% and 35% of the section thrust value at almost all sections along the span, in contrast to the open configuration where they were within the $20 - 25\%$ range.

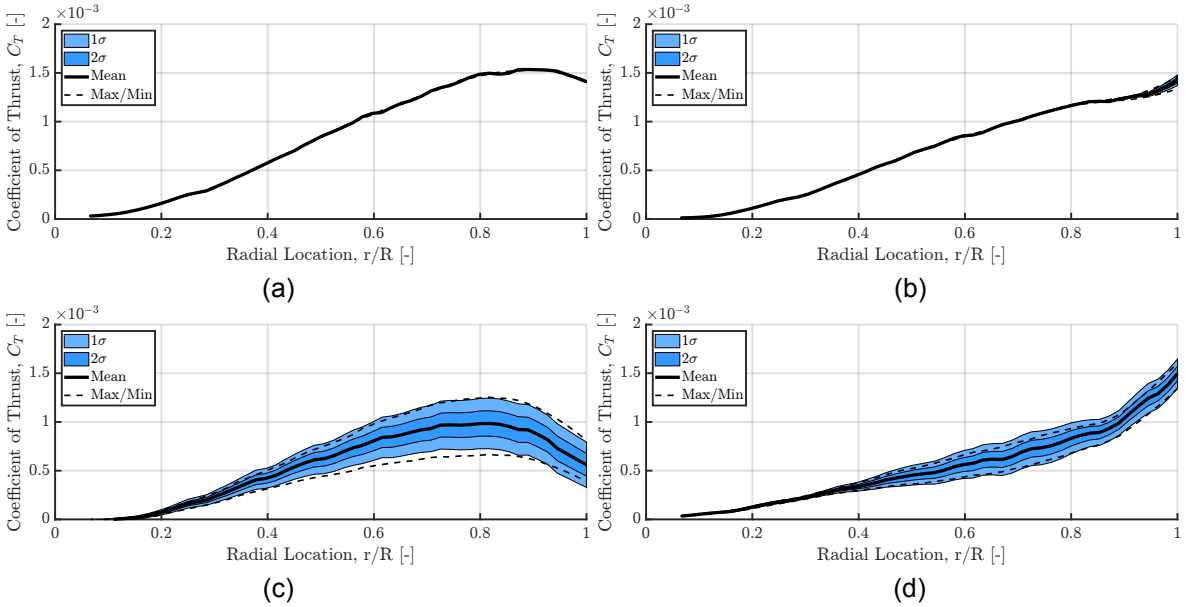

Figure 5.10: Radial thrust distribution along the (a) shrouded single propeller in the lead position, (b) shrouded single propeller in the rear position, (c) lead propeller from the S-CRP configuration, and (d) rear propeller from the S-CRP configuration.

An additional difference is the increased thrust fluctuations observed at the tip of the lead propeller. In the absence of the shroud, thrust fluctuations at the tip were reduced to approximately 10%, but with the shroud, they increased to nearly 45%. This may increase the unsteady loading noise generated from the propeller.

The rear propeller exhibits a somewhat similar pattern for the fluctuations. For regions where $r/R < 0.75$, the actual values of the thrust fluctuations are reduced compared to the case without a shroud. However, as a percentage of the sectional thrust, they are slightly higher, ranging between 15% and 25% of the sectional thrust fluctuations.

In the section where $r/R > 0.75$, the results diverge from what was observed in the open case. Instead of a sharp increase in mean thrust, there is now a steady increase, and the fluctuation magnitudes follow a similar trend. Thus, in regions where the fluctuations, as a percentage of sectional thrust, increased all the way to 41% before returning to 12% at the tip without the shroud, the shrouded case led to a steady decrease, reaching 10%.

Additionally, although the absolute magnitude immediately at the tip is about 10% higher with the shroud than without, at $r/R = 0.85$, the shrouded case exhibits fluctuations that are 200% lower compared to the non-shrouded configuration due to the loss of the peaky region.

All these observations are crucial in understanding how both the presence of a shroud and the use of a contra-rotating propeller alter propeller thrust and acoustic emissions. However, none signify a shift in the mechanisms generating noise. The magnitudes of the fluctuations diminished, and their relative contribution to mean thrust grew for both propellers. Although the distribution of the rear propeller underwent changes, the interaction between the propellers altered only relative to the mean, suggesting that potential interaction remains the prevailing mechanism.

The only possible additional noise-generating mechanism is the unidentified fluctuations at the tip. Before delving into this anomaly, it is imperative to design a shroud without separated flow to determine whether this phenomenon results from flow separation or if it is an intrinsic noise-generating mechanism for S-CRPs.

In summary, separation predominantly results from the shroud design, and its extent does not significantly vary with the propeller's position. However, due to this, the impact of this separation on propeller performance does indeed alter depending on the location of the propeller. While the shroud wall does diminish recirculation at the tips, the separation introduces other undesirable effects. The external contour of the shroud exerts minimal influence on its performance in hover conditions. It remains undetermined whether the tip fluctuations occurring at higher harmonics are related to separation. Nonetheless, the potential interaction between the propellers continues to be the primary contributor to interaction noise.

5.3. Acoustic Emission Results

This section explores acoustic emissions stemming from the CRP and S-CRP systems. The examination separates the components involved. Initially, it explores how the implementation of the coaxial contra-rotating propeller influences acoustics through aerodynamic interactions and acoustic propagation interactions. This is followed by an investigation into the impact of incorporating the shroud. The shroud's effects are categorized into two components: aerodynamic installation effects and acoustic installation effects. The latter contains both body interactions and multi-source combination effects.

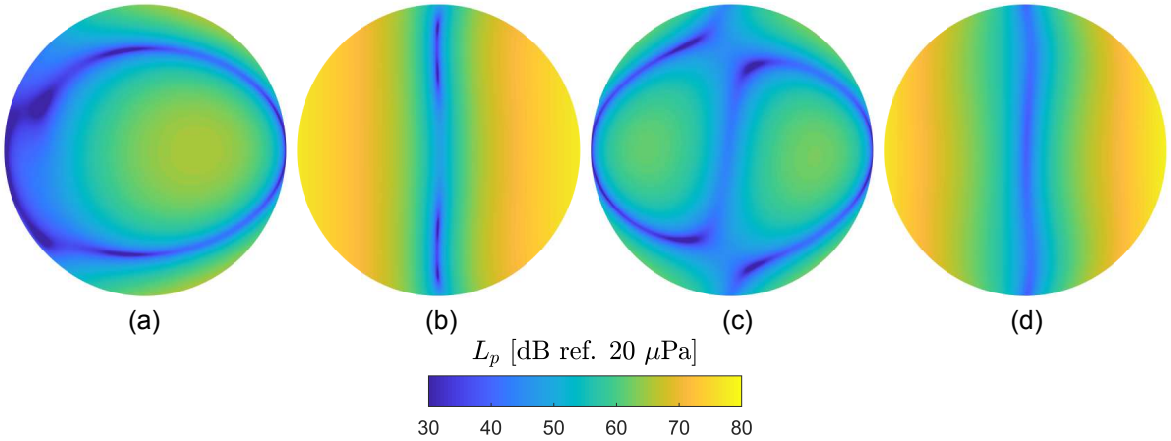

Figure 5.11: Sound pressure level below the CRP configuration, such that the circumference of the plots is the mid-plane listener directivity (thrust vector points to the left), for the (a) 1^{st} BPF, (b) 2^{nd} BPF, (c) 3^{rd} BPF, (d) 4^{th} BPF.

Noise is emitted in all directions, however, simulations and postprocessing are computationally intensive to fully capture the entire field. Additionally, it can be challenging to discern subtle differences between various solutions. Figure 5.11 illustrates sound pressure level over a hemispherical listener array, showcasing unique shapes. However, the most significant alterations can be observed in the mid- and rotor-plane cut lines. Thus, this section will include results at these directivities, which are the most important.

5.3.1. Contra-Rotating Installation Effects

The contra-rotating propeller introduces additional unsteady loading to the propellers and, due to this, introduces additional acoustic blade thrust harmonics which in turn generate additional noise in the far-field. This unsteady loading noise, in addition to the already present steady loading noise, influences all the harmonics of the BPF at the listener. Moreover, the classical quadri-lobal noise pattern documented in existing literature, characterizing the emissions from a CRP configuration, is due to both of these sources and how they interact during acoustic propagation. This section explores these interactions and details how the sound is generated and why it propagates to the far-field in the patterns it does.

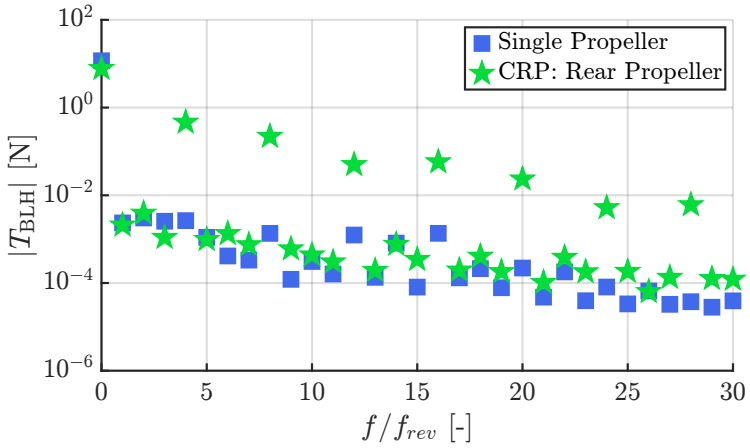

Figure 5.12: The Blade Loading Harmonics for one blade of a propeller in the thrust direction for the open rotor configurations.

Introducing a contra-rotating propeller to a single open propeller generates additional unsteady loading noise on both propellers. This amplifies the loading noise specifically at interaction tones that are multiples of the blade overlap frequency, where $\omega_{n,n} = \omega_{2n,0}$. As demonstrated in Section 5.2.2, this interaction is strongly attributed to potential field interaction. This is an additional noise-generating mechanism affecting tonal loading noise due to the CRP. This is evident in Figure 5.12, where only the frequencies corresponding to $4 \times f_{rev}$ (equivalent to $2 \times BPF$) experience an increase. Consequently, the only extra interaction arises from the blade overlap and its harmonics.

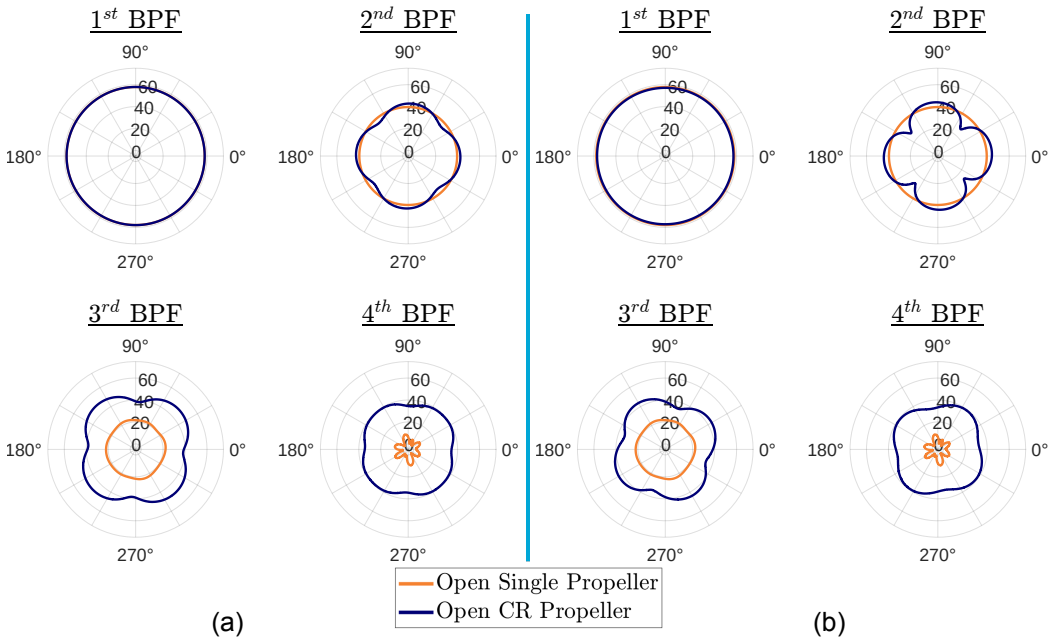

Figure 5.13: Directivities of the noise emissions (L_p [dB]) in the rotor-plane for the (a) lead propeller and the (b) rear propeller.

In the rotor plane, the change in the first BPF is dominated by the mean thrust change of the propeller. The decrease is modest, approximately 1 dB at all angles for the lead propeller and 3 dB for the rear propeller. This reduction is proportional to the mean thrust lost by each propeller, as highlighted in Table 5.3. This decline is illustrated in Figure 5.13 but, also, logically follows from Figure 5.12. Given that the nearest dominant BLH peak to the 1^{st} BPF in the CRP configuration is the mean value ($f/f_{rev} = 0$), the slight decrease in this value will have the most effect on tones at the first BPF at the listeners.

Because the source of the interaction noise only occurs at even BPFs, the first listener harmonic to be affected by the interaction is the 2^{nd} BPF. At this frequency, both propellers display a clover-like pattern. However, this pattern is skewed from the overlap axis aligning the lobes exactly with the azimuthal location of maximum thrust, as depicted in Figure 5.6. Therefore, $3.63°$ counter-clockwise from the axis of overlap for the lead propeller and $3.64°$ clockwise for the rear propeller.

This symmetry effect also persists for the higher harmonics, as the centerlines of the lobes are consistently skewed evenly on both sides of the centerline of the lobe of the full configuration (Figure 5.14).

Several implications arise from this observation. Firstly, it suggests that the lobes will correspond to the location of the largest thrust, implying that lower spatial variance in thrust could result in more uniform and possibly lower noise. Secondly, it indicates that the two skewed lobes combine to form a lobe precisely on the overlap axis, implying they are perfectly symmetric about this axis. This indicates the influence of potential flow effects, which affects both propellers.

An additional indication is made in Figure 5.14 for the total noise of the first BPF. The full system directivity shows traditional quadri-lobal shape found in literature, such as Refs. [12] and [14], however, the individual propellers do not. Thus, when this shape results from steady loading it is not due to the aerodynamic interaction of the propellers rather, it is due to the phase difference of the acoustic pressure propagation. Thus, it is the *acoustic installation effects* that dictate this shape. The same effect causes additional lobes for the second BPF.

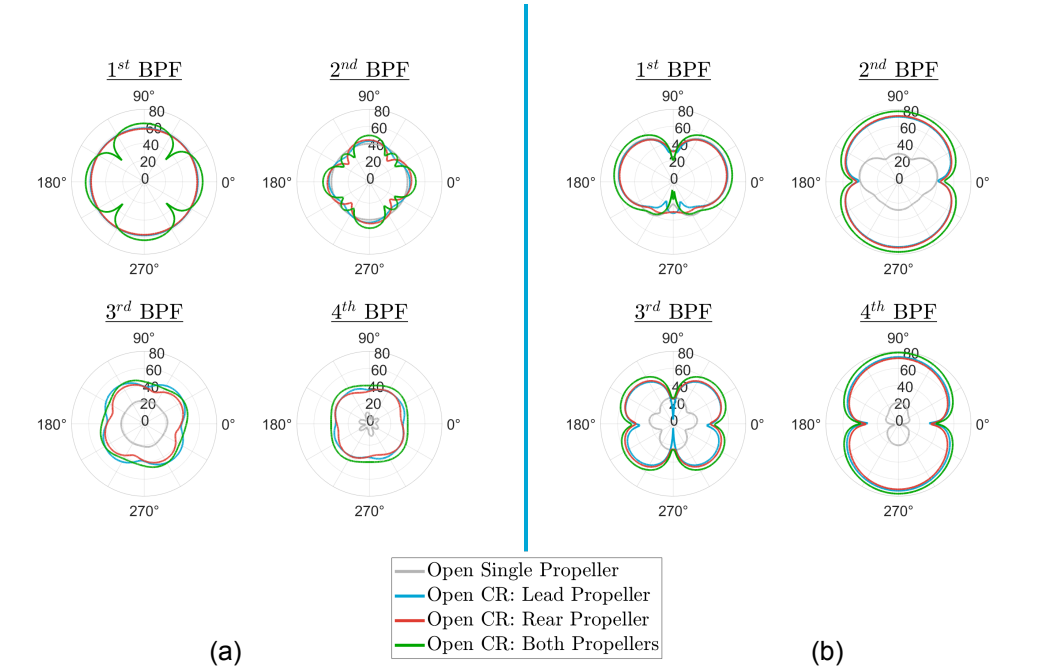

Figure 5.14: Directivities of the noise emissions (L_p [dB]) from the components of the CRP configuration in (a) rotor-plane and the (b) mid-plane.

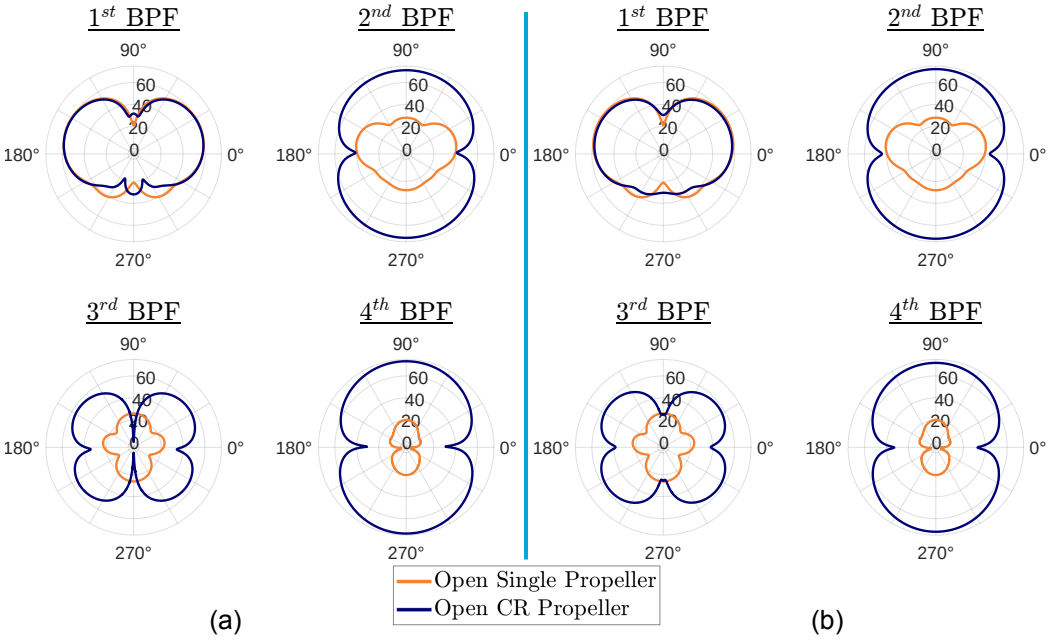

Figure 5.15: Directivities of the noise emissions (L_p [dB]) in the mid-plane for the (a) lead propeller and the (b) rear propeller.

The results in the mid-plane (Figure 5.15) provide a more consistent narrative across both propellers and their combined far-field impact. At the first harmonic, both the lead and rear propeller sources in the contra-rotating system produce noise levels similar to those of isolated propellers. This suggests that the small increase in noise observed in Figure 5.14(b) is due to constructive interference of the waves generated by the two separate sources. This pattern holds true for the higher harmonics as well, with the shape and magnitude of the noise at the listener locations being nearly identical for both propeller sources. Moreover, the combined noise from both sources is only slightly higher, indicating consistent constructive interference across all harmonics.

The bi-lobal shape observed at the even harmonics is typical of noise dominated by unsteady load-

ing in the thrust direction. This suggests that unsteady loading is more prominent than steady loading for both propellers and that unsteady loading in the thrust direction has a dominant influence, even though radial and azimuthal components also contribute.

In contrast, the odd harmonics not only exhibit reduced noise in the rotor plane but also in front of and behind the propeller. Considering Equation 2.19, the Bessel function, which dictates the modulation of loading harmonics into listener harmonics, has subscript as a function of $m - 2k$. If the harmonic is odd, by this function it can never be zero, and $J_0(x)$ is the most efficient connection between source and listener.

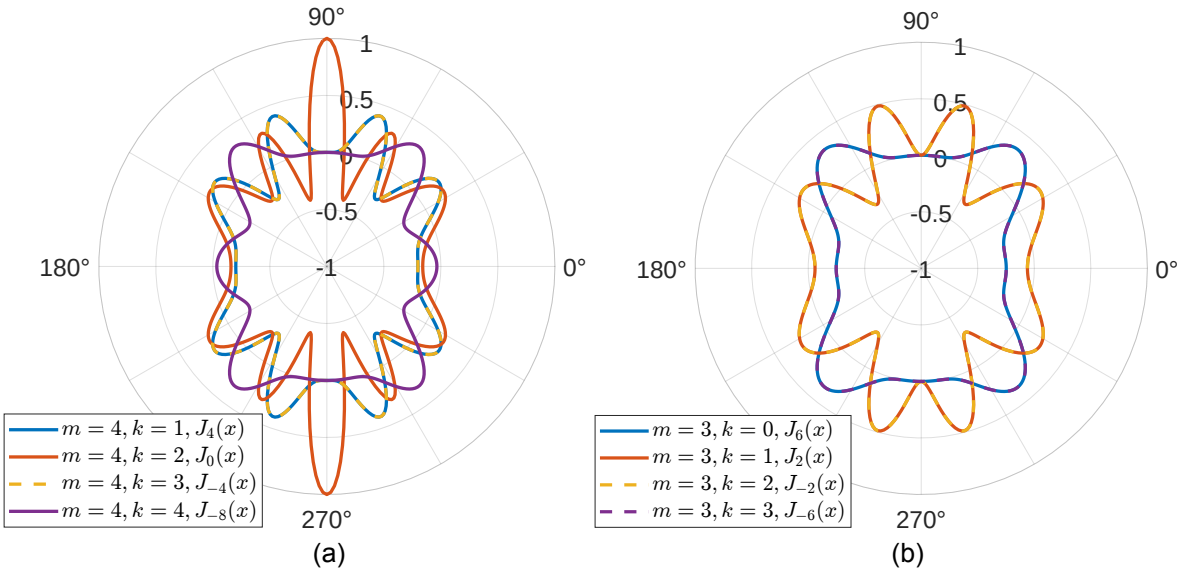

Figure 5.16: Directivity modulating factor on relevant BLHs, k, for (a) an even multiple, $m = 2$, and (b) an odd multiple, $m = 3$, of the listener BPF harmonic.

This is shown explicitly in Figure 5.16 which depicts the result of the Bessel function from Equation 2.19. This plot is represented on the listener directivities as they are defined in Figure 3.9 from the simulations, the solution to the Bessel function as it is defined in the equation is $90°$ rotated. Figure 5.16(a) the largest contributor in the axial direction at even multiples of the listener BPF ($\forall m | m \in 2\mathbb{Z}$) is the loading harmonic $k = m/2$. At the odd multiples of the BPF harmonics for the listener ($\forall m | m \in 2\mathbb{Z} + 1$) the source $k = m/2$ cannot exist and the closest values, $k = m/2 \pm 0.5$, only give a Bessel function subscript of ± 2. The solution to these functions at $\theta = 0$ and 180 (defined as $\theta = 90$ and 270 in the simulations) is zero.

From this, it can be concluded that all of the noise in the odd BPF harmonics is due to the modulation of noise from even BPF harmonics. The contribution of the noise at the same BPF harmonic has a small influence and the lack of $J_0(x)$ will not allow the noise to occur in the axial flow direction. This additionally explains why though only the interaction harmonics (even BPF multiples) are produced (Figure 5.12) there is still a high sound level at the odd BPF multiples.

A solution for the same geometry, employing a methodology closely resembling the formula in Equation 2.19, was generated at École Centrale de Lyon as part of the ENODISE project. Although no formal publication is available, the results can be found in Ref. [20].

In the mid-plane, these results (Figure 5.17) display a similar shape and amplitude to the uRANS-FEM results. However, they do not match in the rotor plane. This discrepancy can likely be attributed to the fact that the ECL solution used realistic but arbitrary values for lift and drag coefficients, treating the blade segments as flat plates. Additionally, it does not fully account for the effects of the tip region, and the only employed wake models which may not be the best representation for highly inclined wakes like those in this configuration, as it is an empirical model designed for turbomachinery. This also indicates that the wake interaction may create similar effects in the mid-plane as the combination of potential and wake effects shown in the present study.

This study has revealed insights into the noise emissions of CRPs. The introduction of a contra-rotating mechanism amplifies unsteady loading noise likely due to the interaction of the potential fields

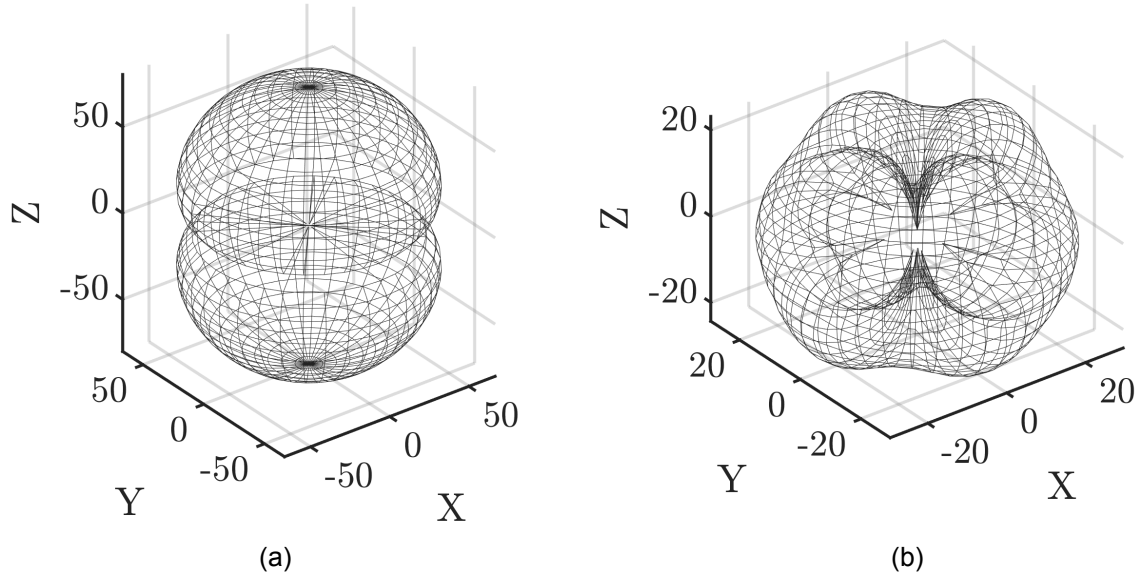

Figure 5.17: Results from analytical solution using approximated loads where the axis is the SPL level along the direction labeled for the (a) 2^{nd} BPF and (b) 3^{rd} BPF. [20]

of the propeller blades but, only at tones multiple of the blade overlap frequency and its harmonics. In the rotor plane, noise reduction occurs at the first BPF correlating to the reduction in mean thrust. Furthermore, the noise pattern at the 2^{nd} BPF displays a distinct clover-like shape, with the centerlines of the lobes consistently skewed, suggesting that noise emissions are intricately linked to the maximum thrust locations. The acoustics also indicate the influence of potential flow effects on both propellers.

The mid-plane results suggest that the noise levels from both the lead and rear propellers individually at the first BPF in the CRP configuration are still due to the mean thrust, however, their acoustic interaction gives the quadri-lobal shape from the literature. Odd BPF harmonics exhibit reduced noise compared to even harmonics which shows that noise at these frequencies results from the modulation of even BPF harmonics and the interaction noise only occurs at the interaction frequencies.

The current findings and those from the École Centrale de Lyon match well. The exception is in the rotor plane which is likely due to differences in the methodologies and assumptions, such as the use of arbitrary values for lift and drag coefficients or the wake model employed. The consistent noise patterns across different analyses, however, affirm the robustness of the study's findings and the complex interplay of factors influencing CRP noise emissions.

5.3.2. Shroud Aerodynamic Installation Effects

The goal of incorporating a shroud around propellers is to generate its own thrust and increase the propeller efficiency, some designs may inadvertently alter their aerodynamic and acoustic characteristics in additional ways. Noise directivity analyses indicate that the aerodynamic effects of the shroud in this study mildly reduce noise at lower BPFs but, only due to the decrease in mean thrust. This effect is less noticeable at higher BPFs, where contra-rotating interaction noises generate a majority of the sound. Similarly, mid-plane studies show modest noise reduction at lower BPFs, however, the rear propeller experiences an additional noise increase at higher BPFs, due to complex flow near the propeller tip.

The shroud's presence marginally affects the noise within the rotor plane produced by a single propeller, primarily by reducing the propeller's mean thrust and consequently, the steady loading noise. This observation is evident when comparing the blue and black lines in Figure 5.18, which display minor reductions at each BPF. Specifically, the lead propeller shows an average noise reduction of 0.61 dB and 0.76 dB for the 1^{st} and 2^{nd} BPFs, respectively. Likewise, the rear propeller exhibits only a slightly larger noise decrease, averaging 1.12 dB for the 1^{st} BPF and 1.19 dB for the 2^{nd} BPF. This small alteration, coupled with the consistent pattern, suggests that the shroud introduces only minimal changes to the propeller's aerodynamic noise sources, as the shroud is designed to do.

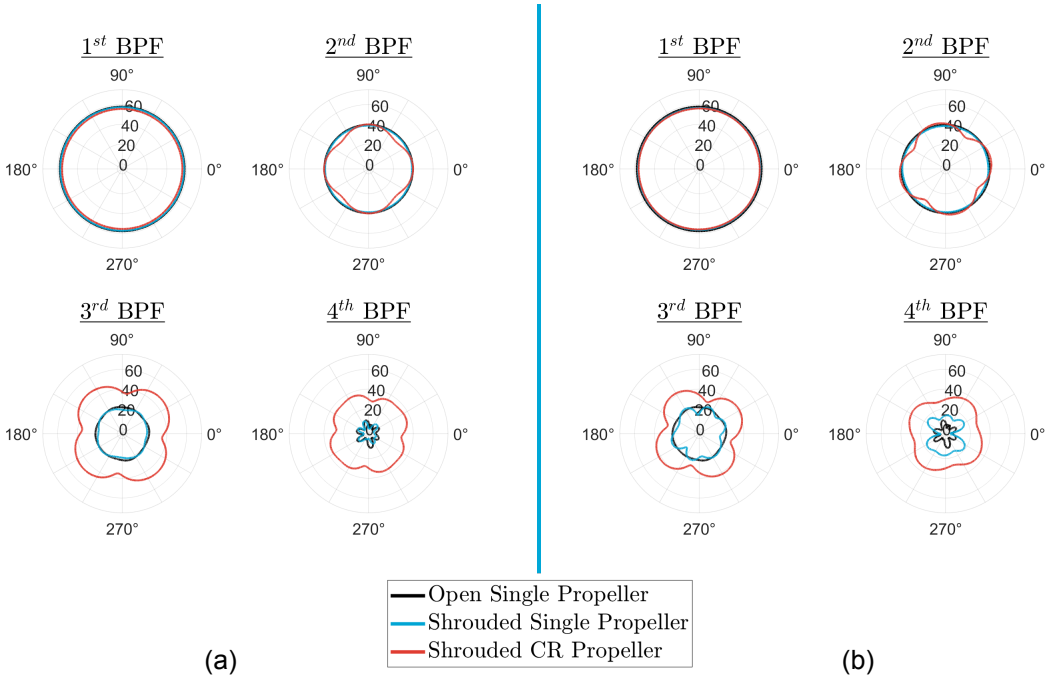

Figure 5.18: Directivities of the noise emissions (L_p [dB]) in the rotor-plane only considering propeller sources (no scattering) for the (a) lead propeller and the (b) rear propeller.

In a shrouded contra-rotating setup, the primary aerodynamic modification when compared to a single open rotor involves the potential flow variation resulting from the proximity of the adjacent propeller. This factor becomes increasingly prominent as the dominant contributor to tonal loading noise, particularly at higher harmonics (3^{rd} BPF harmonic and beyond) where the steady loading has decreased. This is depicted by the red line in Figure 5.18. The 1^{st} BPF continues to be predominantly influenced by steady loading, with additional reductions in propeller thrust within the full S-CRP configuration due to both the shroud and coaxial propeller contributing to a further decrease in mean thrust. The ensuing acoustic directivities maintain the same trend identified in Section 5.3.1 due to contra-rotating propellers.

In the mid-plane, the lead propeller's behavior exhibits a trend similar to that observed in the rotor plane, with the aerodynamic effects of the shroud primarily contributing to a decrease in sound pressure level, especially noticeable at the first BPF. This noise is further reduced by the combined effect of the shroud and the contra-rotating propeller, leading to a more pronounced decrease in noise at the first BPF, attributed to a reduction in thrust.

However, beyond the first BPF in the S-CRP configuration, the noise in the mid-plane is dominated by interaction noise, particularly at the even BPF harmonics. Simultaneously, the increase in noise at odd BPF harmonics follows the same trend and noise-generation mechanism described in Section 5.3.1, indicating that the shroud's aerodynamic influence is comparatively minor relative to the effects of contra-rotating interactions.

The behavior of the rear propeller slightly deviates from the trends observed due to the shroud in the mid-plane. While the influence on steady loading remains consistent, there's an introduction of additional unsteady loading at higher BPF harmonics not present in the open rotor. This phenomenon is particularly evident in the dipolar pattern observed at the 3^{rd} and 4^{th} BPFs in Figure 5.19(b), likely resulting from unsteady fluctuations near the propeller tips, as described in Section 5.2.2. The exact origin of these fluctuations is unclear — they may be due to wake re-ingestion or vortex formation along the wall — but they appear to be related to separation, as they are only present in the region impacted by shroud separation and are absent for the lead propeller.

For the S-CRP configuration, this additional unsteady loading is nearly negligible. The noise levels continue to be primarily governed by the unsteady loading resulting from the interaction of the propellers, confirming it as the dominant noise-generating mechanism. Noteworthy, though, are the slight noise increases on the thrust axis from this phenomenon, which changes the noise from inaudible (such

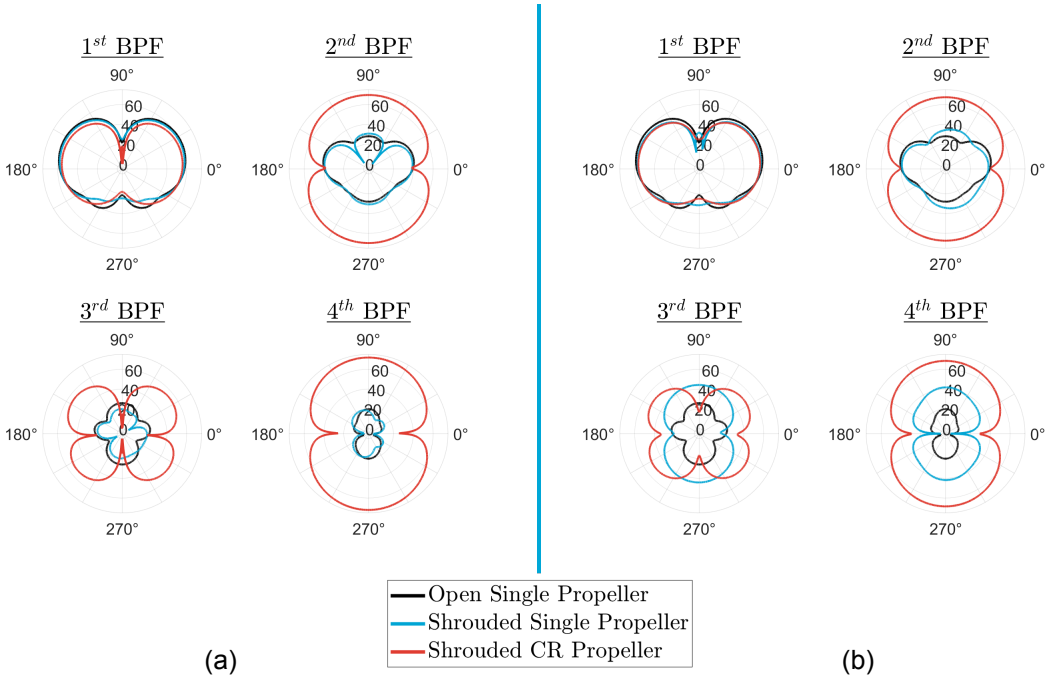

Figure 5.19: Directivities of the noise emissions (L_p [dB]) in the mid-plane only considering propeller sources (no scattering) for the (a) lead propeller and the (b) rear propeller.

as at the 3^{rd} BPF for the lead propeller in Figure 5.19(a)) to slightly increased for the rear propeller (Figure 5.19(b)). At even harmonics, the increase is dominated by the CRP interaction noise so this effect is not visible.

Overall, the shroud subtly modifies the acoustic profile, primarily diminishing noise through reduced steady loading. This effect is consistent across single and contra-rotating configurations, albeit more pronounced with the latter due to compounded aerodynamic interactions which reduce thrust. However, the shroud's influence wanes at higher BPF harmonics, where interaction noise dominates. Interestingly, the shroud instigates additional unsteady loading noise in the rear propeller due to aerodynamic phenomena. Ultimately, while the shroud contributes to noise reduction, its influence is secondary to the dominant noise mechanisms inherent in contra-rotating propellers.

5.3.3. Shroud Acoustic Installation Effects

In this section, the acoustic installation effects of the shroud are analyzed. This compares the same propeller sources with and without the shroud present in the acoustic FEM mesh during the simulation, thus the results discussed are in addition to the aerodynamic installing effects discussed in the previous section. The shroud affects the acoustic propagation of the noise in two ways. Firstly, the shroud creates either amplification or attenuation of acoustic source power depending on the location. Secondly, the shroud redirects the noise emitted in different locations by both blocking and warping the acoustic pressure as it propagates in the near-field. This second factor is the dominant effect in changing the noise directivity and is dependent on the propeller location within the shroud.

	Lead Propeller		Rear Propeller	
Source	$1^{st}BPF$	$2^{nd}BPF$	$1^{st}BPF$	$2^{nd}BPF$
Free Propagation	67.32	78.54	68.00	76.23
Acoustic Installation	71.42	80.53	65.72	77.55

Table 5.4: Sound Power Level (SWL) of the S-CRP configuration for the whole domain when only the propeller sources are considered (free propagation) and when the propeller sources and the acoustic propagation effects are considered (acoustic installation).

The closer to the center of the shroud a propeller is positioned, the more it is prone to experiencing attenuation, or at the very least, a diminished amplification compared to a propeller situated closer to

the leading edge. This phenomenon is evident from the SWL (Equation 2.8) in Table 5.4, which shows that the lead propeller's sound level rises by several decibels for the first and second BPF harmonics, a result of incorporating propagation effects. Conversely, the rear propeller sees a similar amount reduced from its sound level for the first BPF and a lesser increase at the second BPF.

While the literature, as discussed in Section 2.4.1, anticipates a reduction in SWL due to shielding effects, the topic of near-field amplification remains underexplored, with no substantial studies or official publications dedicated to it.

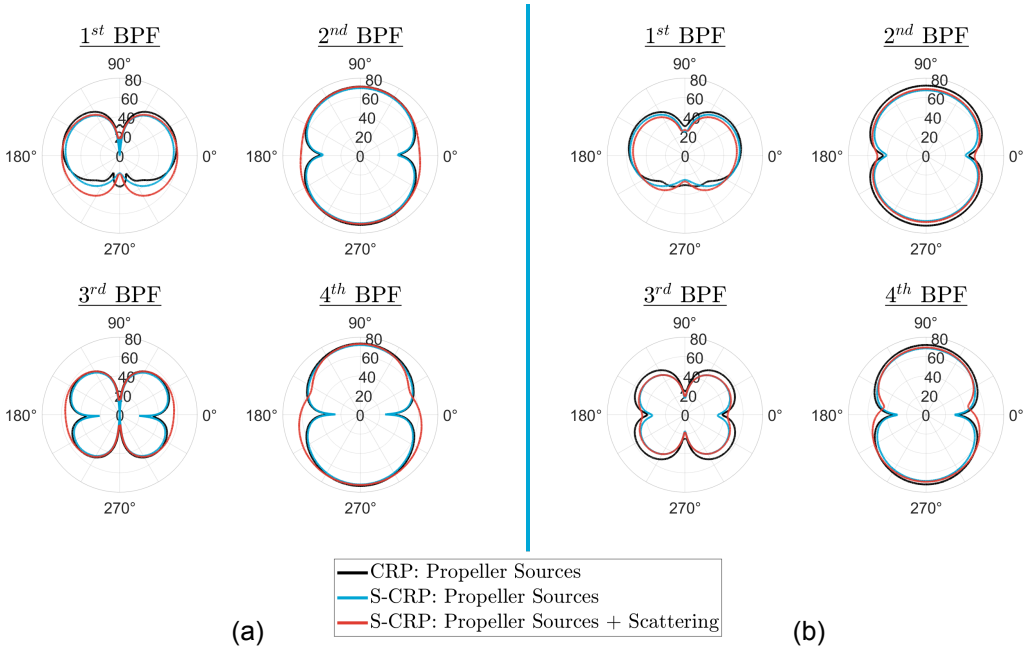

Figure 5.20: Directivities of the noise emissions (L_p [dB]) in the mid-plane for the (a) lead propeller and the (b) rear propeller.

These alterations in the configuration's sound power level also manifest in the far-field acoustics. As indicated by the red line in Figure 5.20, there are variations in the results for each S-CRP propeller when acoustic effects are accounted for relative to the free propagation baseline of the S-CRP propeller (blue line). The change in the primary lobes mirrors the changes in SWL. Consequently, along the thrust axis, the noise emitted by the lead propeller experiences a slight increase, and the rear propeller exhibits a decrease at the first BPF, followed by a rise at the second BPF which is smaller than that of the lead propeller.

The observed changes are only a few decibels, this is because the variations in the SWL are small. Additionally, the change is lower than the most pronounced acoustic effect of the shroud, the redirection of noise. It is this redirection that results in significant sound level spikes in the rotor axis ($0° - 180°$). While Figure 5.20 illustrates this only for propeller sources in an S-CRP configuration, the phenomenon is inherent to the interaction between the propeller and its shroud. This is evident for single propellers encased in a shroud, as shown in Appendix A.

Individually, a 20 dB increase, which occurs in the rotor-plane of the lead propeller, can be considered significant considering that humans interpret a 10 dB shift as a doubling in loudness. However, this emerges in areas with minimal or absent noise in free-field propagation conditions and ultimately produces a more consistent noise profile in the mid-plane. This can be observed in the more rounded shape presented in Figure 5.20. Although this effect is most apparent in the lead propeller, the rear propeller exhibits a similar trend, particularly at higher harmonics but does show a decrease at the first harmonic.

In free-field propagation, a propeller emits noise that is almost symmetric around both its rotor and thrust axes. This is depicted in Figure 5.21(a) and 5.22(a). The 3^{rd} BPF is chosen to illustrate this effect because it displays the phenomenon distinctly. Nonetheless, this symmetry is present across all frequencies, as detailed in Appendix A.

The noise from the propeller generally takes on a quadri-lobal shape in the near-field. However, introducing a shroud in the acoustic domain disrupts this quadri-directional propagation. Moreover,

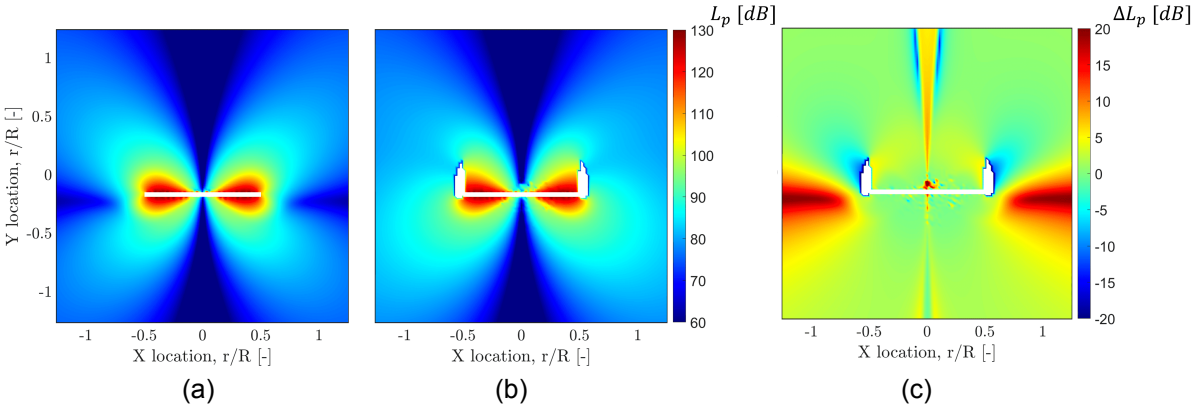

Figure 5.21: The sound pressure level of the lead propeller sources of the S-CRP configuration in the mid-plane at the 3^{rd} BPF with (a) free-field propagation, (b) including acoustic installation effects of the shroud, and (c) difference between the two.

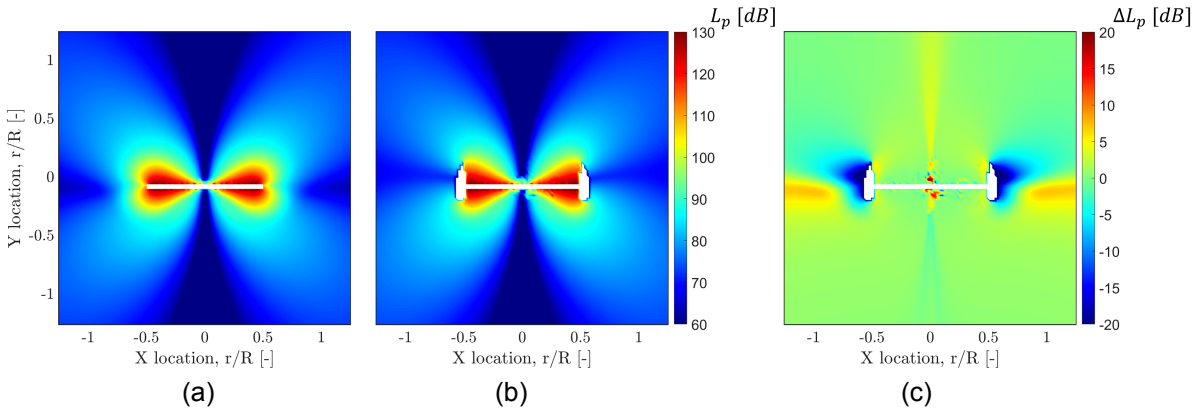

Figure 5.22: The sound pressure level of the rear propeller sources of the S-CRP configuration in the mid-plane at the 3^{rd} BPF with (a) free-field propagation, (b) including acoustic installation effects of the shroud, and (c) difference between the two.

when the propeller isn't perfectly centered within the shroud, it affects the lobes unevenly. This is evident when comparing Figure 5.21(b) to Figure 5.22(b).

Specifically, for the lead propeller, the downstream lobe undergoes attenuation. In contrast, the upstream lobe experiences an increased sound level, which is then warped around the circular leading edge. This same warping is observable at the trailing edge, though it's less pronounced there. This warping not only shifts the direction of noise propagation but also influences how noise behaves in the near field. It results in shadow zones of decreased noise close to the propeller and constructive interaction of noise propagating beyond this. The shadow zones fade rapidly in the near-field as the combination of the increased pressure areas fills in within the rotor plane.

This phenomenon occurs for both propellers however, the lead propeller has a larger warping of the sound due to its proximity to the leading edge. The rear propeller still sees a small increase in the rotor plane and has a slight asymmetry towards the leading edge. This is noted in Figure 5.20(b) with the lower but still increased noise in the rotor plane from the 2^{nd} BPF harmonic and up. At the 1^{st} BPF the steady loading noise already dominates in the rotor plane so this effect actually contributes more to evening the noise ahead and behind the rotor plane.

Both propeller positions exhibit this phenomenon. However, the lead propeller experiences a more pronounced warping of sound due to its closer location to the leading edge. In contrast, the rear propeller displays a smaller noise increase in the rotor plane but, still has a mild asymmetry oriented towards the leading edge. This is additionally captured in Figure 5.20(b), where there is a lower, but still increased, noise in the rotor plane starting from the 2^{nd} BPF harmonic and extending upwards. For the 1^{st} BPF, the consistent loading noise already predominates within the rotor plane. Thus, this effect mainly serves to balance out the noise in front of and behind the rotor plane.

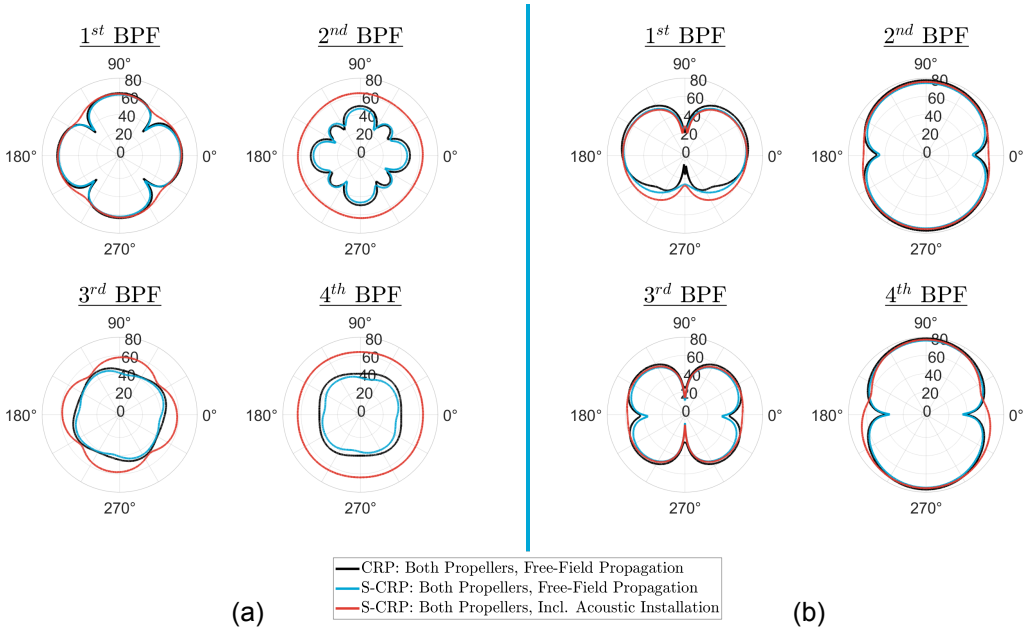

Figure 5.23: Directivities of the noise emissions (L_p [dB]) from the combination of the two propeller sources in (a) rotor-plane and the (b) mid-plane.

When the sources of both propellers are considered in the domain, the same acoustic interaction that was noted in Section 5.3.1 occurs. The interaction noise is in phase and amplifies in all directions due to constructive interference. The steady loading noise is perfectly out of phase because the propeller rotates in opposite directions at the same rate and this leads to constructive interference on the axes of overlap and destructive interference on the off axes. This generated the shapes shown in value in Figure 5.23.

In addition to this, the shrouded propellers emit, on average, less sound than the open CRP propellers. The influence of the separated flow reduces the influence of potential field distortion on the propeller tips for the rear propeller. This causes the lobes to be very slightly skewed compared to the open CRP lobes (Figure 5.23) due to the comparatively higher influence of the lead propeller. The peak noise of the combined propeller with the aerodynamic influence of the shroud of the first BPF still being $0.16°$ off the axis of overlap and the second BPF being $0.15°$ off.

Lastly, the scattering of the source of the shroud does not introduce any new phasing effects. Since both propellers respond uniformly to changes in SWL and exhibit increased noise in the rotor plane due to the acoustic spreading, these effects simply compound in every direction.

The position of a propeller within its shroud impacts its acoustic signature. While the shroud can serve to attenuate noise, as found in the literature, it often does not due to its design and the placement of the propeller playing pivotal roles in determining the final sound profile. As shown, a propeller nearer to the center of the shroud experiences low amplification or attenuation. This is due to both the reduction of total acoustic source strength and the lower likelihood of the noise being warped around the shroud and interacting constructively. Moreover, when both propellers are considered, interactions of the free-field propagation lead to specific amplification and cancellation effects in the noise patterns but, the scattering effects are simple constructive interference.

6

Conclusion

6.1. Conclusions

This study aimed to address the fundamental questions outlined in Chapter 1. This has been completed through a case-specific study detailed in this entire report, which also includes all the background information necessary to understand the analyses. First, the verification and validation of the methodology is concluded as using this in a novel application was also an objective of this study. Then, the answers to the questions are presented one at a time in the sections below.

Methodology

The uRANS-FEM methodology used in this study involved simulating the aerodynamics of various propeller system configurations. The surface pressure results from these simulations were then used to define acoustic loads, which were subsequently propagated in an acoustic FEM mesh. This approach allowed for the capture of near-field effects and the extension of results to a far-field listener location.

Each step of the methodology was validated against the available experimental data, first for aerodynamics and then for acoustics. Additionally, other methodologies were considered for comparison, but they lacked the critical advantages required for this study of the uRANS-FEM approach, particularly its ability to account for the impact of near-field bodies on acoustic propagation.

The results obtained from the aerodynamic methodology fall within an acceptable level of accuracy. Specifically, for the validated CRP configuration, the average thrust closely matches the experimental value, with discrepancies of less than 5% observed across all mesh sizes. Moreover, as the mesh cell density increases, the extrapolated thrust values continue to maintain a difference well below this 5% threshold. Additionally, the wake velocity observed at the rear of the propeller aligns well with the flow characteristics reported in experimental hotwire analyses, providing a realistic representation of the flow field.

The sound pressure levels obtained through the uRANS-FEM methodology at the identified tonal peaks exhibit reasonable agreement, with an average difference of 3.96 dB in the rotor plane (although one case with a maximum difference of 8.95 dB did occur) when compared to the experimental peaks. The differences are also shown to decrease with the microphone's distance from the source.

It is important to acknowledge that the methodology's primary limitation is that it solely captures tonal loading noise. Yet, it performs relatively well in resolving the tonal peaks indicating a large influence of tonal noise. This study suggests that the refinement used is sufficient for the aerodynamic simulation to accurately capture the pressure fluctuations that characterize the noise sources. Beyond this point, further refinement does not yield significant benefits to the solution as all relevant scales are captured.

The methodology is shown to be effective in predicting the pattern of the tonal noise and close in the magnitude where loading noise is dominant. This gives good predictions at the lower harmonics for all configurations and higher harmonics for configurations with periodic loading, such as the CRP. However, in cases where loading noise is not dominant, such as the higher harmonics in the single rotor experiment, the agreement with this methodology significantly deteriorates since it cannot provide information beyond the tonal component.

Furthermore, this study concludes that for higher multiples of the BPF in a CRP configuration, noise is significantly impacted, if not dominated, by loading noise. This explains why the results align well with this methodology, which effectively captures these noise characteristics.

The majority of the study's analysis was conducted at a listener radius of $20D$ from the sources. For the higher harmonics, the two acoustic propagation methods exhibited a very close agreement. However, at the 1^{st} BPF, there remained a noticeable difference between the results of the two methods. This discrepancy can be attributed to the fact that at this low frequency, the relatively few number of wavelengths present was insufficient for the near-field effects to dissipate. Therefore, the uRANS-FEM method yielded more accurate results as the other method lacks a near-field term. This is as confirmed by comparison with the experimental data.

The general shape of the directivities in this study aligns with those reported in the literature. For the CRP case, the quadri-lobal shape described in Ref. [14] is observed in the rotor plane for the first two BPF harmonics of the complete CRP system. A comparison with an analytical solution employing the same geometry, but approximate loads, yielded a favorable agreement. Given the limitations of the analytical method, the results in the mid-plane exhibit very good agreement, while the rotor plane displays a somewhat different shape. This discrepancy is anticipated to be reconciled when considering the full wake shape and loading distribution, which can now be implemented for the model under investigation.

Objective: To identify and distinguish the specific mechanisms responsible for performance and acoustic directivity in CRP configurations, and to investigate the applicability and modification of these mechanisms in S-CRP configurations.

What is the trade-off in terms of Figure of Merit, thrust per area, and acoustic emissions when a contra-rotating propeller configuration is used in place of a single propeller?

The contra-rotating propeller geometry offers a blend of enhancements and drawbacks compared to single-propeller systems. Notably, CRPs exhibit improved efficiency metrics, with a 2.98% increase in FOM and a 57.53% increase in thrust per area. These improvements underscore CRPs' advantages in terms of efficiency and compactness, particularly relevant for urban applications.

However, this configuration introduces higher noise levels, especially at higher harmonics, with increases ranging from 10 dB to 50 dB in various directions. This rise in noise is attributed to the close interaction of the CRP propellers, impacting both the sound directivity level and shape. While the noise change at the 1^{st} BPF is less pronounced in magnitude, the directivity shape shifts considerably. At higher harmonics, the acoustic pattern varies distinctly between odd and even multiples of the BPF due to the modulation effects of blade loading harmonics.

In terms of thrust distribution and unsteady loading, CRPs exhibit a reduction in thrust for both the lead (8.97% decrease) and rear (33.49% decrease) propellers. The rear propeller is more adversely affected due to the wake of the lead propeller, especially within its inner 75% radius. Additionally, unsteady loading is introduced, predominantly in the thrust direction, likely resulting from the potential interaction between the propellers. While this is certainly the case for the lead propeller it is particularly challenging to decouple this effect from the wake interaction for the rear propeller.

There is also an intriguing correlation between peak thrust and noise generation in CRPs. The highest thrust for both propellers occurs just before their axes overlap in the azimuthal plane, coinciding with the maximum noise directivity at the 2^{nd} BPF for each propeller. In the far field, these noise peaks symmetrically combine out when both propellers operate together, forming the typical CRP directivity shape with peaks along the axis of overlap. This shape is also formed at the 1^{st} BPF due to the phasing of the sound pressure interaction as this frequency is dominated by steady loading noise.

How much are the aerodynamic performance and the noise-generating mechanisms modified when employing a shroud designed for single propeller systems on a CRP one?

The shroud designed to produce its own thrust and improve the propeller efficiency for a single propeller, doesn't translate as effectively to a contra-rotating system. In such a system, the additional space inside the shroud causes airflow separation at the leading edge, disrupting the flow over the propeller tips. This results in different interactions between each propeller and the shroud, as they encounter varying degrees of separated flow. Consequently, there is a significant thrust reduction, with the lead propeller losing 54.42% and the rear propeller 54.29% of their thrust due to both the shroud effects and the propeller-propeller interaction.

Despite these drawbacks, the shroud still contributes to overall thrust as it was designed to do, generating over one-third of the system's total thrust. Moreover, compared to a single propeller, the shroud increases the thrust per area by 41.91% while maintaining a similar FOM. Although it's less effective than an open CRP system, it still marks an improvement.

From an acoustic standpoint, the aerodynamic installation effect of the shroud is relatively small, resulting in a minor reduction in noise primarily due to the loss of mean thrust. This reduction in noise is relatively consistent across different propeller positions within the shroud suggesting that the only position-based aerodynamic influence is due to the separating flow previously mentioned. However, there is an exception in the form of fluctuations that appear at the blade tip, which seem to generate unsteady noise in the rotor plane at higher harmonics. This suggests the presence of phenomena that modulate the thrust at a rate corresponding to 3 times the BPF and higher harmonics.

Can a shroud be used to mitigate noise radiation when used on a contra-rotating configuration?

In the literature the shrouds of single propeller systems were shown to only reduce noise in the rotor-plane forward flight but they were able to mitigate noise increases on the rotor plane in hover conditions. This is not a phenomenon recreated for contra-rotating propellers in this study and a different scenario is presented.

Contrary to established predictions, an increase in noise observed from the CRP system to the S-CRP system due to acoustic interference is primarily concentrated in the rotor plane. This increase occurs primarily in the rotor plane and ranges from about 5 to 25 dB depending on the frequency and azimuth angle.

Further analysis reveals that the shroud's acoustic installation effect is heavily dependent on the propeller's position within it. Particularly, the lead propeller's close proximity to the shroud's leading edge results in a substantial increase in noise, contradicting typical expectations of shrouds dampening sound. In free-field conditions, propellers emit noise symmetrically around both the rotor and rotational axes, but this symmetry is disrupted with the introduction of a shroud, especially when the propeller is not centrally located.

In the case of this study, this asymmetry is due to the lead propeller being near enough to the shroud's leading edge that it interferes with the noise behind the propeller, while sound in front propagates and is spread throughout the domain due to the shroud's warping effect. Consequently, while there is a slight amplification of SWL (4.1 dB at the $1^{st}BPF$) from the acoustic installation of the shroud for the lead propeller, the majority of the sound increase in the domain, particularly in the rotor plane, is attributed to this redistribution of sound.

This effect also only occurs significantly in the rotor plane. The dominating noise source is the unsteady loading noise due to the interaction noise of the propellers. The interaction mechanism is still dominant and the noise scattering is a function of the source strength of the propellers.

6.2. Recommendations

This research project inaugurates a series of studies on S-CRPs for UAM applications, producing key insights and raising supplementary questions for future exploration.

This study sets a foundation that needs further validation. While results have been acquired from the experimental campaign at VKI (chapter 4), additional experiments, particularly for the S-CRP, are pending and vital for validating the results.

The blade shape, especially the sweep, emerged as a significant parameter due preparing for this study. Due to its influencing both potential and viscous interactions between propellers in open CRP

configurations, future phases of study should meticulously analyze these interactions with the intention of extrapolating the findings to optimize S-CRPs.

The current state of the shroud is not recommendable due to its decreased performance and amplified noise. The separation along the shroud wall significantly hinders system performance, eliminating pressure recovery and decreasing propeller performance. Subsequent studies should explore the potential design of a shroud that mitigates these issues, possibly focusing initially on the hover conditions presented here.

The S-CRP configuration generates increased acoustic emissions largely due to the lead propeller's proximity to the leading edge. Investigating the exact cause of the noise increase, its association with acoustic installation effects, and identifying whether similar effects occur near the trailing edge is crucial. This prompts a broader question: Is there an optimal location within the duct for a two-propeller system, and how can the shroud be configured to generate thrust efficiently while managing acoustic emissions?

While the literature and present study affirm potential interaction effects and noise creation in the CRP configuration, the optimal propeller spacing for the S-CRP configuration remains undetermined. Further exploration is warranted to discern the ideal propeller spacing and its implications on performance and noise in the shrouded configuration.

The optimization of the system introduces a complex problem due to the interdependency of various parameters - propeller position in the shroud, propeller spacing, shroud shape, propeller shapes, and tip gap. These not only impact one another but also jointly influence performance and noise levels, creating an optimization challenge with a large number of variables. However, the identified noise-generating mechanisms in this study are applicable across different configurations, providing an initial direction for this optimization.

Diving deeper than geometry, it is imperative to examine these configurations in the context of specific applications to understand how these insights translate to operational scenarios and mission profiles. Especially, understanding how variation in inflow conditions, pertinent to UAMs and drones during non-hovering operations, impacts performance and noise emission will be pivotal.

In summary, this study has paved a path in understanding S-CRPs and their potential in UAM applications. The roadmap ahead entails intricate studies focusing on validation, optimization, acoustic research, and practical applications, which will collectively further the knowledge and practicality of S-CRPs in real-world scenarios.

Additional Acknowledgements

This project has received funding from the European Union's Horizon 2020 research and innovation programme under grant agreement No 860103. Results are uploaded to a database found at Ref. [2].

Bibliography

[1] Barker, J. E., Zarri, A., Christophe, J., and Schram, C. F., "Numerical Investigation of Tonal Noise Emissions from Propeller-Wing Aerodynamic and Acoustic Interactions," *AIAA AVIATION 2023 Forum*, 2023. https://doi.org/10.2514/6.2023-4056.

[2] Barker, J. E., Zarri, A., LeBras, S., Christophe, J., and Schram, C., "H2020 ENODISE: VKI and SISW Numerical Aeroacoustic Database of Configuration C," 2023. https://doi.org/https://doi.org/10.5281/zenodo.8305812.

[3] Barker, J. E., Zarri, A., LeBras, S., Christophe, J., and Schram, C., "H2020 ENODISE: VKI Numerical Aeroacoustic Database of Configuration B1," 2023. https://doi.org/https://zenodo.org/record/8306236.

[4] "EHang 216," *TransportUp webpage*, 2023. URL https://transportup.com/ehang-216/.

[5] Wauters, R., "Electric air taxi startup Volocopter raises €200 million in Series D funding," *Tech.Eu webpage*, 2021. URL https://tech.eu/brief/electric-air-taxi-startup-volocopter-raises-e200-million-in-series-d-funding/.

[6] "Moog Surefly," *EVTOL News: Vertical Flight Society*, 2023. URL https://evtol.news/workhorse/.

[7] Magliozzi, B., Hanson, D., and Amiet, R., "Propeller and propfan noise," *Aeroacoustics of flight vehicles: theory and practice*, Vol. 1, 1991, pp. 1–64.

[8] Schram, C., "How wrong can a flow model be, and yet provide a reasonable acoustic prediction?" *Internal Presentation: von Karman Institute for Fluid Dynamis and NASA Ames Research Center*, 2014.

[9] Sforza, P. M., *Theory of aerospace propulsion*, Butterworth-Heinemann, 2016.

[10] Wald, Q. R., "The aerodynamics of propellers," *Progress in Aerospace Sciences*, Vol. 42, No. 2, 2006, pp. 85–128. https://doi.org/https://doi.org/10.1016/j.paerosci.2006.04.001.

[11] Casalino, D., and Avallone, F., "Class Notes: Fundamentals of Aeroacoustics," *Technische Universiteit Delft*, 2023.

[12] Dittmar, J. H., "Some design philosophy for reducing the community noise of advanced counter-rotation propellers," Tech. rep., 1985.

[13] Chaitanya, P., Joseph, P., Prior, S., and Parry, A., "On the optimum separation distance for minimum noise of contra-rotating rotors," *Journal of Sound and Vibration*, 2022, p. 117032.

[14] Hanson, D. B., "Noise of counter-rotation propellers," *Journal of Aircraft*, Vol. 22, No. 7, 1985, pp. 609–617.

[15] Zhao, L., and Shkarayev, S., "Characterization of ducted contra-rotating propeller propulsions," *International Journal of Micro Air Vehicles*, Vol. 11, 2019, p. 1756829319837661. https://doi.org/10.1177/1756829319837661.

[16] Goudswaard, R., "Aerodynamic performance of a small-scale ducted rotor in hover: An experimental study on the effect of the tip gap," *Masters Thesis, Delft University of Technology*, 2021.

[17] Dyer, K., "Aerodynamic Study of a Small, Ducted VTOL Aerial Vehicle," *MIT Department of Aeronautics and Astronautics: Master Thesis*, 2000.

[18] Pereira, J. L., *Hover and wind-tunnel testing of shrouded rotors for improved micro air vehicle design*, University of Maryland, College Park, 2008.

[19] Malgoezar, A. M., Vieira, A., Snellen, M., Simons, D. G., and Veldhuis, L. L., "Experimental characterization of noise radiation from a ducted propeller of an unmanned aerial vehicle," *International Journal of Aeroacoustics*, Vol. 18, No. 4-5, 2019, pp. 372–391. https://doi.org/10.1177/1475472X19852952.

[20] Roger, M., Giraldo, D. A., and Jacob, M. C., "H2020 ENODISE Analytical Data Set configuration C ECL," 2023. https://doi.org/https://zenodo.org/record/8301188.

[21] Borer, N. K., Patterson, M. D., Viken, J. K., Moore, M. D., Bevirt, J., Stoll, A. M., and Gibson, A. R., *Design and Performance of the NASA SCEPTOR Distributed Electric Propulsion Flight Demonstrator*, 2016. https://doi.org/10.2514/6.2016-3920.

[22] Hermetz, J., Ridel, M., and Doll, C., "Distributed electric propulsion for small business aircraft a concept-plane for key-technologies investigations." *ICAS 2016*, 2016.

[23] "Airbus CityAirbus," *EVTOL News: Vertical Flight Society*, 2023. URL https://evtol.news/airbus-helicopters/.

[24] Anand, A., Kaur, H., Justin, C. Y., Zaidi, T., and Mavris, D. N., "A Scenario-Based Evaluation of Global Urban Air Mobility Demand," *AIAA Scitech 2021 Forum*, 2021, p. 1516.

[25] Grandl, G., Salib, J., and Kirsch, J., "The Economics of Vertical Mobility: A guide for investors, players, and lawmakers to succeed in urban air mobility," *Porsche Consulting*, 2021.

[26] Stokkermans, T. C. A., Usai, D., Sinnige, T., and Veldhuis, L. L. M., "Aerodynamic Interaction Effects Between Propellers in Typical eVTOL Vehicle Configurations," *Journal of Aircraft*, Vol. 58, No. 4, 2021, pp. 815–833. https://doi.org/10.2514/1.C035814.

[27] Johnson, W., Silva, C., and Solis, E., "Concept vehicles for VTOL air taxi operations," *AHS Technical Conference on Aeromechanics Design for Transformative Vertical Flight*, 2018.

[28] Christian, A. W., and Cabell, R., "Initial Investigation into the Psychoacoustic Properties of Small Unmanned Aerial System Noise," *23rd AIAA/CEAS Aeroacoustics Conference*, 2017. https://doi.org/https://doi.org/10.2514/6.2017-4051.

[29] Mulero-Pázmány, M., Jenni-Eiermann, S., Strebel, N., Sattler, T., Negro, J. J., and Tablado, Z., "Unmanned aircraft systems as a new source of disturbance for wildlife: A systematic review," *PLOS ONE*, Vol. 12, No. 6, 2017, pp. 1–14. https://doi.org/10.1371/journal.pone.0178448.

[30] McKay, R. S., Kingan, M. J., and Go, R., "Experimental investigation of contra-rotating multi-rotor UAV propeller noise," *Proceedings of ACOUSTICS*, Vol. 10, 2019.

[31] Filippone, A., "Historical development of the coaxial contra-rotating propeller," *The Aeronautical Journal*, 2022, p. 1–38. https://doi.org/10.1017/aer.2022.92.

[32] Biermann, D., and Gray, W. H., "Wind Tunnel Tests of Single and Dual-Rotating Pusher Propellers Having from 3 to 8 Blades," *NACA ARR (WR L-359)*, 1942.

[33] "Pop.Up Next," *ITALDESIGN*, 2023. URL https://www.italdesign.it/project/pop-up-next/.

[34] Huo, C., and Liu, Z., "Performance evaluations of a shrouded contra-rotating rotor based on a novel-designed platform with multiple testing possibilities," *Proceedings of the Institution of Mechanical Engineers, Part G: Journal of Aerospace Engineering*, Vol. 234, No. 14, 2020, pp. 2062–2075.

[35] Zhang, T., and Barakos, G. N., "High-fidelity numerical analysis and optimisation of ducted propeller aerodynamics and acoustics," *Aerospace Science and Technology*, Vol. 113, 2021, p. 106708. https://doi.org/https://doi.org/10.1016/j.ast.2021.106708.

[36] Jung, R., Kingan, M. J., Dhopade, P., and Sharma, R. N., "Investigation of the Interaction Tones Produced by a Contra-rotating Unmanned Aerial Vehicle Propeller," *28th AIAA/CEAS Aeroacoustics 2022 Conference*, 2022, p. 2832.

[37] König, R., Gerlach, A., Schmidt, H., and Stumpf, E., "Experimental investigation on acoustics and efficiency of rotor configurations for electric aerial vehicles," *INTER-NOISE and NOISE-CON Congress and Conference Proceedings*, Vol. 263, Institute of Noise Control Engineering, 2021, pp. 323–334. https://doi.org/10.3397/IN-2021-1435.

[38] Lanchester, F., "Investigation of the Efficiency of Reverse Rotating Propellers in Tandem," *British ARC R M No. 540*, 1918.

[39] Lanchester, F., "Contra-Props," *Flight Magazine*, 1941, p. 418–419.

[40] "NOISE STANDARDS: AIRCRAFT TYPE AND AIRWORTHINESS CERTIFICATION," *14 CFR §36*, 2018.

[41] Carlton, J., *Marine propellers and propulsion*, Butterworth-Heinemann, 2018.

[42] Gilbert, B. L., Oman, R. A., and Foreman, K. M., "Fluid dynamics of diffuser-augmented wind turbines," *Journal of Energy*, Vol. 2, No. 6, 1978, pp. 368–374. https://doi.org/10.2514/3.47988.

[43] Grunwald, K. J., *Division of Aerodynamic Loads on a Semispan Tilting-ducted-propeller Model in Hovering and Transition Flight: Kalman J. Grunwald and Kenneth W. Goodson*, National Aeronautics and Space Administration, 1962.

[44] Grunwald, K. J., and Goodson, K. W., *Aerodynamic Loads on an Isolated Shrouded-propeller Configuration of Angles of Attack from-10 Degrees to 110 Degrees*, National Aeronautics and Space Administration, 1962.

[45] AirbusHelicopters, "005766101-Fenestron," *EUIPO*, 2008.

[46] "Avata," *DJI webpage*, 2023. URL https://www.dji.com/nl/avata.

[47] Schram, C., Bériot, H., Roger, M., Reese, H., and Carolus, T., "On the importance of near-field terms in the assessment of acoustic installation effects for ducted low-Mach number fans," *15th AIAA/CEAS Aeroacoustics Conference (30th AIAA Aeroacoustics Conference)*, 2009, p. 3334.

[48] Smith, S. N., "Discrete frequency sound generation in axial flow turbomachines," *University Engineering Dept., Cambridge*, 1972.

[49] Kaji, S., and Okazaki, T., "Propagation of sound waves through a blade row: II. Analysis based on the acceleration potential method," *Journal of Sound and Vibration*, Vol. 11, No. 3, 1970, pp. 355–IN1.

[50] Pierce, A. D., *Acoustics: an introduction to its physical principles and applications*, Springer, 2019.

[51] Zarri, A., Dell'Erba, E., Munters, W., and Schram, C., "Aeroacoustic installation effects in multi-rotorcraft: Numerical investigations of a small-size drone model," *Aerospace Science and Technology*, Vol. 128, 2022, p. 107762. https://doi.org/https://doi.org/10.1016/j.ast.2022.107762.

[52] Simons, D., and Snellen, M., "Course AE4431 Aircraft Noise and Emissions," *Delft University of Technology: Course Reader*, 2022.

[53] Lighthill, M. J., "On sound generated aerodynamically I. General theory," *Proceedings of the Royal Society of London. Series A. Mathematical and Physical Sciences*, Vol. 211, No. 1107, 1952, pp. 564–587.

[54] Curle, N., "The influence of solid boundaries upon aerodynamic sound," *Proceedings of the Royal Society of London. Series A. Mathematical and Physical Sciences*, Vol. 231, No. 1187, 1955, pp. 505–514.

[55] Ffowcs-Williams, J. E., and Hawkings, D. L., "Sound generation by turbulence and surfaces in arbitrary motion," *Philosophical Transactions of the Royal Society of London. Series A, Mathematical and Physical Sciences*, Vol. 264, No. 1151, 1969, pp. 321–342.

[56] Farassat, F., and Succi, G. P., "A review of propeller discrete frequency noise prediction technology with emphasis on two current methods for time domain calculations," *Journal of Sound and Vibration*, Vol. 71, No. 3, 1980, pp. 399–419.

[57] Tam, C. K., "Computational aeroacoustics: an overview of computational challenges and applications," *International Journal of Computational Fluid Dynamics*, Vol. 18, No. 6, 2004, pp. 547–567.

[58] Anderson, J. D., "Fundamentals of Aerodynamics," *McGraw-Hill, Inc.*, 1991.

[59] Marte, J. E., and Kurtz, D. W., "A Review of Aerodynamic Noise From Propellers, Rotors and Lift Fans," *National Aeronautics and Space Administration*, 1970.

[60] Torija, A. J., and Clark, C., "A Psychoacoustic Approach to Building Knowledge about Human Response to Noise of Unmanned Aerial Vehicles," *International Journal of Environmental Research and Public Health*, Vol. 18, No. 2, 2021. https://doi.org/10.3390/ijerph18020682.

[61] Brooks, T. F., Pope, D. S., and Marcolini, M. A., "Airfoil self-noise and prediction," Tech. rep., 1989.

[62] Zarri, A., Christophe, J., Moreau, S., and Schram, C., "Influence of Swept Blades on Low-Order Acoustic Prediction for Axial Fans," *Acoustics*, Vol. 2, No. 4, 2020, pp. 812–832. https://doi.org/10.3390/acoustics2040046.

[63] Casalino, D., Grande, E., Romani, G., Ragni, D., and Avallone, F., "Definition of a benchmark for low Reynolds number propeller aeroacoustics," *Aerospace Science and Technology*, Vol. 113, 2021, p. 106707. https://doi.org/https://doi.org/10.1016/j.ast.2021.106707.

[64] Goldstein, M. E., “Aeroacoustics,” *McGraw-Hill International Book Company*, 1976.

[65] Roger, M., and Kucukcoskun, K., “Near-and-far field modeling of advanced tail-rotor noise using source-mode expansions,” *Journal of Sound and Vibration*, Vol. 453, 2019, pp. 328–354. https://doi.org/https://doi.org/10.1016/j.jsv.2019.02.007.

[66] Yilmaz, S., Erdem, D., and Kavsaoglu, M., “Performance of a ducted propeller designed for UAV applications at zero angle of attack flight: An experimental study,” *Aerospace Science and Technology*, Vol. 45, 2015, pp. 376–386. https://doi.org/https://doi.org/10.1016/j.ast.2015.06.005.

[67] Black, D. M., Wainauski, H. S., and Rohrbach, C., “Shrouded propellers - A comprehensive performance study,” *5th Annual Meeting and Technical Display*, 2012. https://doi.org/10.2514/6.1968-994.

[68] Hubbard, H. H., “Sound measurements for five shrouded propellers at static conditions,” , No. 2024, 1950.

[69] Martin, P., and Tung, C., “Performance and Flowfield Measurements on a 10-inch Ducted Rotor VTOL UAV,” Tech. rep., Army Research Development and Engineering Command Moffett Field CA Aviation, 2004.

[70] Akturk, A., and Camci, C., “Experimental and computational assessment of a ducted-fan rotor flow model,” *Journal of Aircraft*, Vol. 49, No. 3, 2012, pp. 885–897.

[71] Gallo, E., de Decker, J., Haezebrouck, P., Zarri, A., and Schram, C., “H2020 ENODISE: Experimental dataset of configuration C VKI,” 2023. https://doi.org/https://zenodo.org/record/7966211.

[72] “Mejzlik Propeller Calculators,” *Mejzlik webpage*, 2023. URL https://www.mejzlik.eu/technical-data/propeller_calculator.

[73] Jones, W., and Launder, B., “The prediction of laminarization with a two-equation model of turbulence,” *International Journal of Heat and Mass Transfer*, Vol. 15, No. 2, 1972, pp. 301–314. https://doi.org/https://doi.org/10.1016/0017-9310(72)90076-2.

[74] Wilcox, D. C., “Reassessment of the scale-determining equation for advanced turbulence models,” *AIAA journal*, Vol. 26, No. 11, 1988, pp. 1299–1310.

[75] Versteeg, H. K., and Malalasekera, W., “An Introduction to Computational Fluid Dynamics: The Finite Volume Method,” *Pearson Education*, 2007.

[76] Menter, F., “Two-equation eddy-viscosity turbulence models for engineering applications,” *AIAA Journal*, Vol. 32, No. 8, 1994, pp. 1598–1605. https://doi.org/10.2514/3.12149.

[77] “Simcenter STAR-CCM+ 2302 User Guide,” 2023.

[78] *Simcenter Nastran Acoustics User’s Guide (version 2022.1)*, Siemens, 2022.

[79] Menter, F. R., Langtry, R. B., Likki, S. R., Suzen, Y. B., Huang, P. G., and Volker, S., “A Correlation-Based Transition Model Using Local Variables Part 1 — Model Formulation,” *ASME Turbo Expo*, 2004.

[80] Menter, F. R., Smirnov, P. E., Liu, T., , and Avancha, R., “A One-Equation Local Correlation-Based Transition Model,” *Flow, Turbulence and Combustion, Springer*, 2015. https://doi.org/10.1007/s10494-015-9622-4.

[81] Roger, M., “Near-field fan noise modeling and installation effects due to scattering surfaces,” *Fan Noise 2007*, Vol. 3, 2007, pp. 13–21.

[82] Roger, M., and Kucukcoskun, K., “Near-and-far field modeling of advanced tail-rotor noise using source-mode expansions,” *Journal of Sound and Vibration*, Vol. 453, 2019, pp. 328–354. https://doi.org/https://doi.org/10.1016/j.jsv.2019.02.007.

[83] Beriot, H., and Modave, A., “An automatic perfectly matched layer for acoustic finite element simulations in convex domains of general shape,” *International Journal for Numerical Methods in Engineering*, Vol. 122, 2021, pp. 1239–1261. https://doi.org/10.1002/nme.6560.

Appendix A

Additional Acoustic Plots

Directivity Plots

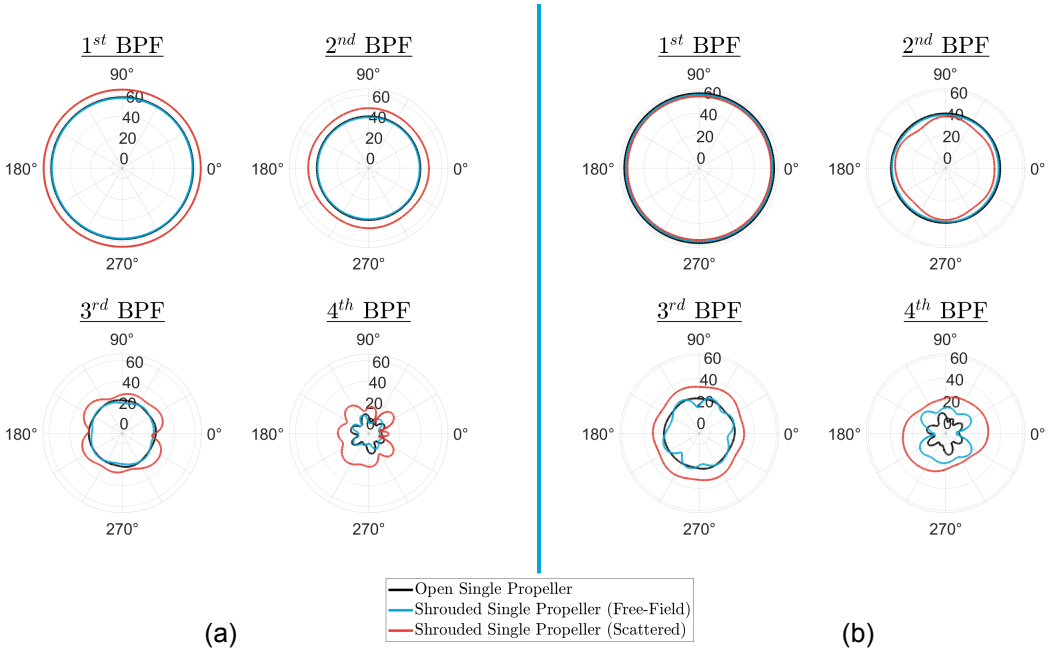

Figure A.1: Directivities of noise emissions in the rotor-plane for the (a) lead propeller and the (b) rear propeller.

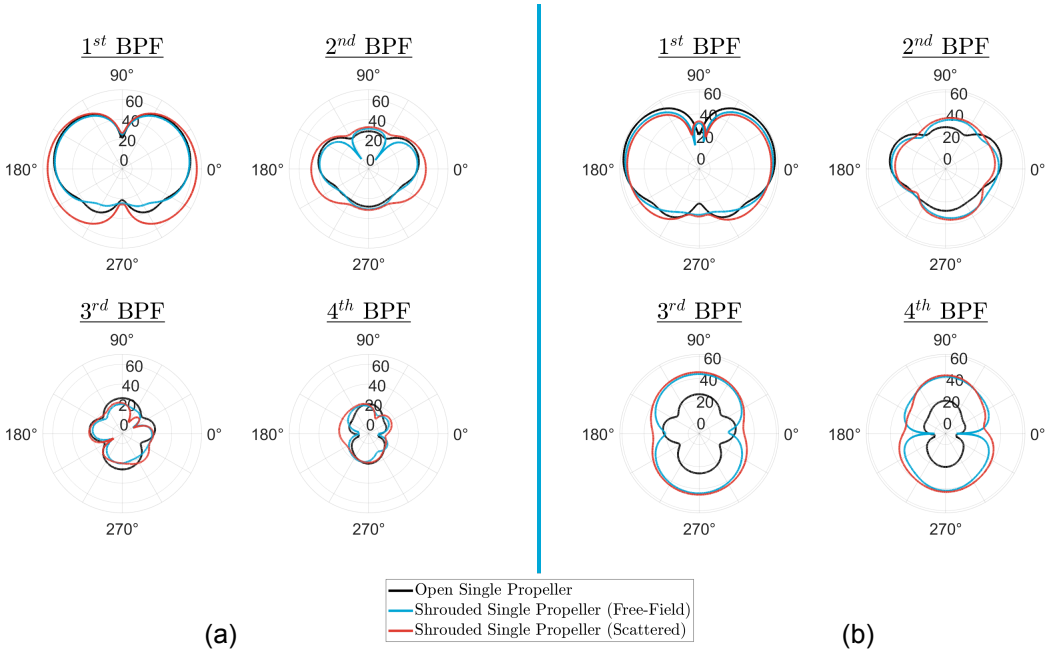

Figure A.2: Directivities of noise emissions in the mid-plane for the (a) lead propeller and the (b) rear propeller.

Midplane Sound Levels

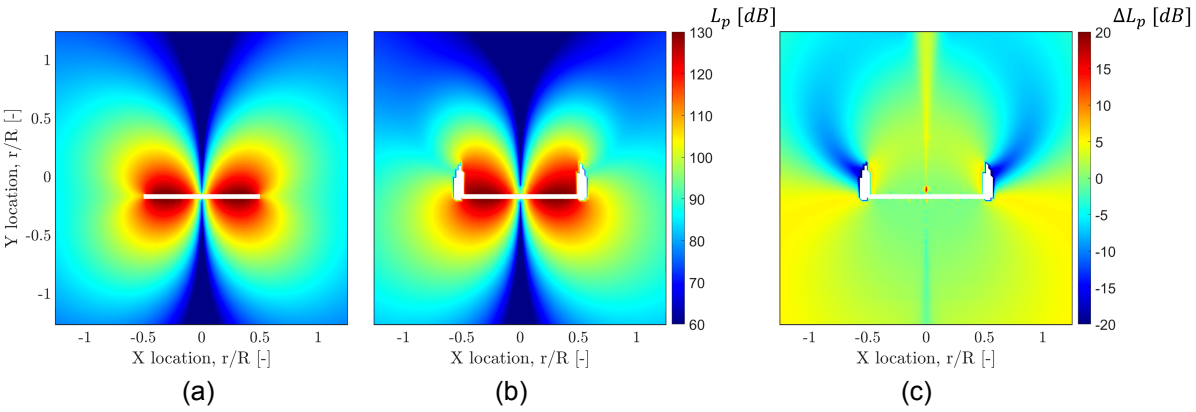

Figure A.3: The sound pressure level of the lead propeller sources of the S-CRP configuration in the mid-plane at the 1^{st} BPF with (a) free-field propagation, (b) including acoustic installation effects of the shroud, and (c) difference between the two.

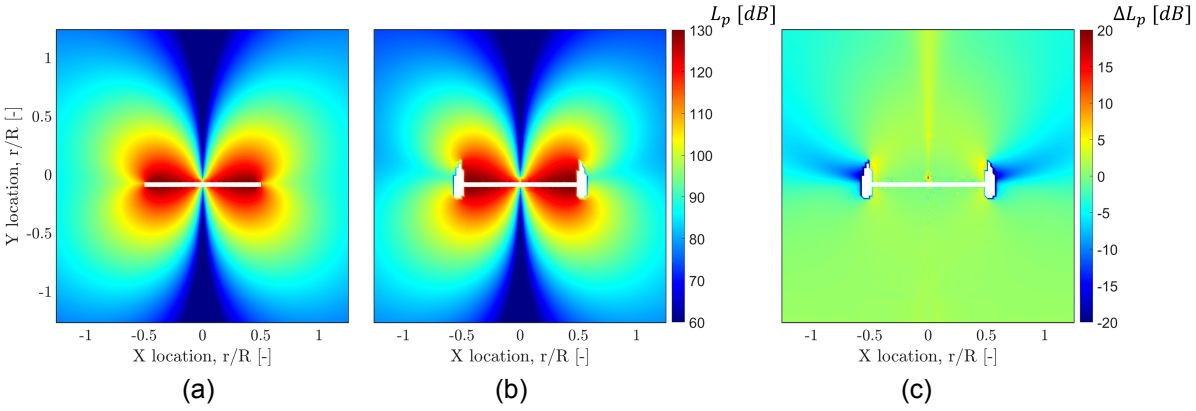

Figure A.4: The sound pressure level of the rear propeller sources of the S-CRP configuration in the mid-plane at the 1^{st} BPF with (a) free-field propagation, (b) including acoustic installation effects of the shroud, and (c) difference between the two.

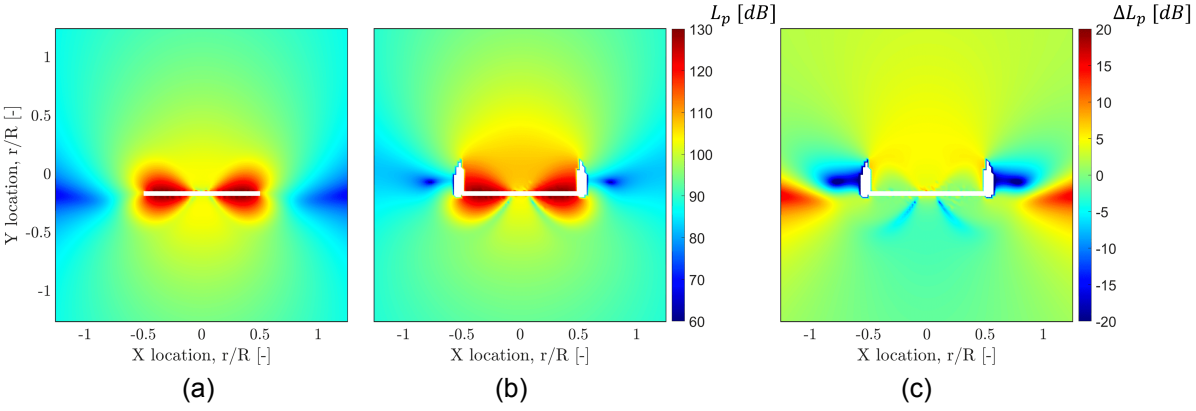

Figure A.5: The sound pressure level of the lead propeller sources of the S-CRP configuration in the mid-plane at the 2^{nd} BPF with (a) free-field propagation, (b) including acoustic installation effects of the shroud, and (c) difference between the two.

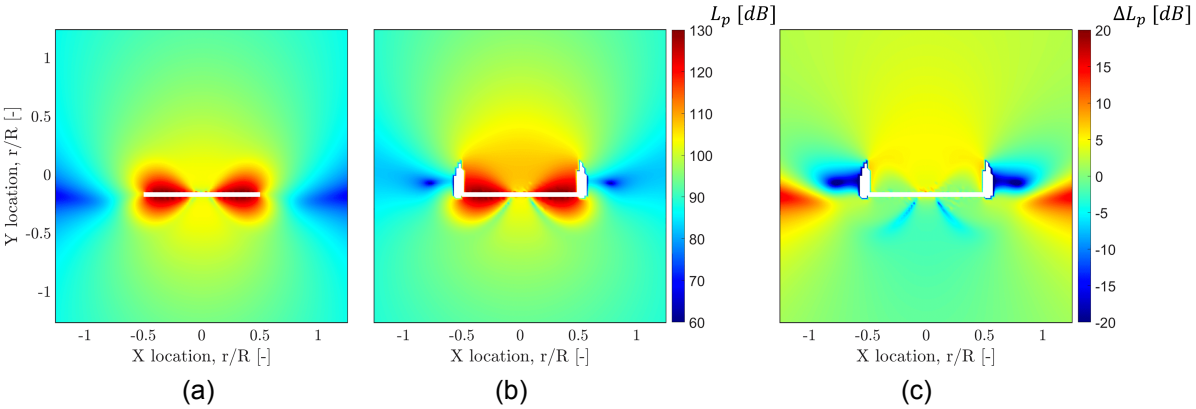

Figure A.6: The sound pressure level of the rear propeller sources of the S-CRP configuration in the mid-plane at the 2^{nd} BPF with (a) free-field propagation, (b) including acoustic installation effects of the shroud, and (c) difference between the two.

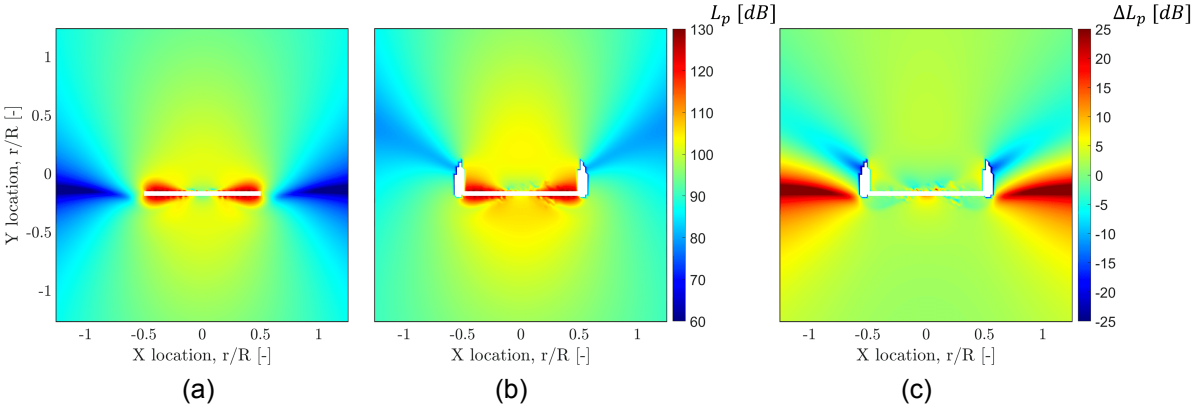

Figure A.7: The sound pressure level of the lead propeller sources of the S-CRP configuration in the mid-plane at the 4^{th} BPF with (a) free-field propagation, (b) including acoustic installation effects of the shroud, and (c) difference between the two.

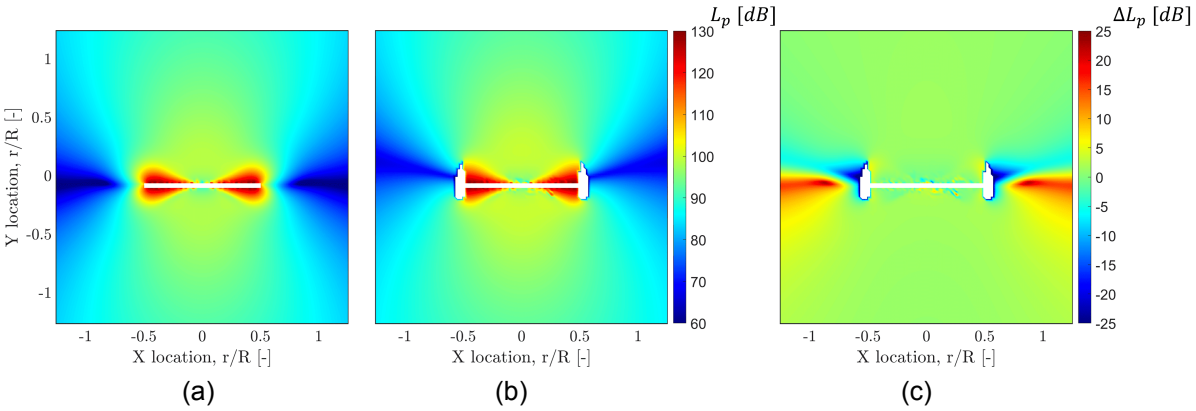

Figure A.8: The sound pressure level of the rear propeller sources of the S-CRP configuration in the mid-plane at the 4^{th} BPF with (a) free-field propagation, (b) including acoustic installation effects of the shroud, and (c) difference between the two.